

**THREE-DIMENSIONAL  
RAY-TRACING SIMULATIONS OF  
CONVECTIVE GRAVITY WAVES**

**Dissertation**

zur Erlangung des Grades  
Doktor der Naturwissenschaften (Dr. rer. nat.)

vorgelegt der

**Bergischen Universität Wuppertal**  
Fachbereich C - Mathematik und Naturwissenschaften

von

**Silvio Kalisch**

Wuppertal 2014

Die Dissertation kann wie folgt zitiert werden:

urn:nbn:de:hbz:468-20150512-113322-1

[<http://nbn-resolving.de/urn/resolver.pl?urn=urn%3Anbn%3Ade%3Ahbz%3A468-20150512-113322-1>]

## **Abstract**

Due to their importance for large-scale circulations and their contribution to the energy and momentum budget of the middle atmosphere, gravity waves have been subject of investigation for many in-situ and satellite measurements. These observations show that the horizontal wavelength of a gravity wave can be as short as a few kilometers, hence, they cannot be directly resolved by General Circulation Models (GCM)s. For this reason, their propagation and interaction with the background atmosphere have to be parametrized. These gravity wave parametrizations play an important role in state-of-the-art GCMs as they contribute to the energy and momentum budget of the middle atmosphere and directly influence the model dynamics. For technical reasons, most gravity wave parametrizations restrict the propagation of gravity waves to the vertical direction. Consequently, modeled distributions of momentum flux and gravity wave drag show remarkable deviations from the three-dimensional propagation as shown in this thesis. The most obvious differences found in the three-dimensional case are the poleward directed meridional drag and the shift of the zonal drag maximum towards higher latitudes in the winter hemisphere. Another simplification of gravity wave parametrizations is the homogeneous and isotropic non-orographic launch distribution, which is unable to resolve single gravity wave sources. In particular, dynamic sources

---

like convection remain unresolved and their time-dependent excitation process cannot be represented using a static launch distribution. Thus, the second aim of this thesis is to investigate the excitation and propagation of gravity waves forced by deep convection in the troposphere and estimate their influence on the middle atmosphere. For that purpose, the well-proven gravity wave ray-tracer GROGRAT has been coupled to the Yonsei convective gravity wave source model. Remaining free model parameters have been constrained to measurements and lead to a coupled convective gravity wave model representing convective excitations from small cells of deep convection up to large-scale convective clusters. Additionally, limitations of satellite instruments were taken into account to compare the simulation results from this thesis with global distributions of gravity wave momentum flux and drag. The *observational filter* of a satellite instrument restricts measurements of gravity waves to waves with horizontal wavelengths longer than 100km. Convective gravity waves, however, show non-negligible contributions to the overall momentum flux spectrum also for wavelengths shorter than 100km. Therefore, the last part of this thesis addresses this discrepancy between simulated and observable gravity wave spectrum. The direct comparison between simulations with *observational filter* and satellite observations shows a remarkable good agreement in the momentum flux distribution.

## **Zusammenfassung**

Aufgrund ihrer Bedeutung für großskalige Zirkulationen und das Energie- und Impulsbudget der mittleren Atmosphäre, sind Schwerewellen, unter Verwendung von in-situ- und Satellitenmessungen, bereits seit längerer Zeit Objekt intensiver Forschung. Diese Messungen zeigen unter anderem, dass die horizontale Wellenlänge einer typischen Schwerewelle auch im Bereich von nur einigen Kilometern liegen kann, weshalb sie von Atmosphärenmodellen (GCM)s nicht direkt aufgelöst werden können. Aus diesem Grunde werden ihre Ausbreitung und Interaktion mit dem atmosphärischen Hintergrund parameterisiert. Diese Schwerewellenparameterisierungen spielen für heutige GCMs eine so große Rolle, da sie nicht nur das Gesamtenergie- und Impulsbudget der mittleren Atmosphäre beeinflussen, sondern sich darüber hinaus direkt auf die Dynamik des Modells auswirken. Aus verschiedenen technischen Gründen wird die Ausbreitung von Schwerewellen dabei in den meisten Parameterisierungen auf eine rein vertikale Ausbreitung beschränkt. Im Vergleich zu einer korrekt modellierten dreidimensionalen Ausbreitung ergeben sich daraus signifikante Abweichungen in den Impulsfluss- und Schwerewellendragverteilungen. Diese Abweichungen wurden im Rahmen der vorliegenden Dissertation erstmals untersucht. So wurde für den Fall dreidimensionaler Ausbreitung von Schwerewellen eine stets polwärts gerichtete Meridionalbeschleunigung gefunden. Weiterhin lässt sich eine polwärts Verschiebung des Maximums der

---

Zonalbeschleunigung in der Winterhemisphäre feststellen. Eine weitere Vereinfachung heutiger Schwerewellenparameterisierungen findet sich in der Annahme einer homogenen und isotropen nichtorographischen Startverteilung, welche nicht in der Lage ist spezifische Schwerewellenquellen aufzulösen. Im Besonderen betrifft dies dynamische Quellen wie Konvektion, deren zeitabhängige Anregungsprozesse nicht durch eine statische Startverteilung wider gegeben werden können. Daher beschäftigt sich der zweite Teil dieser Dissertation mit der Untersuchung dieses Anregungsprozesses in der Troposphäre und der sich daran anschließenden Ausbreitung der konvektiv angeregten Schwerewellen, sowie der Bestimmung ihres Einflusses auf die mittlere Atmosphäre. Zu diesem Zweck wurde das Schwerewellen ray-tracing Modell GROGRAT mit dem Yonsei Modell für konvektive Anregung von Schwerewellen gekoppelt. Verbleibende freie Parameter wurden hierbei entsprechend vorhandener Beobachtungen eingestellt. Diese technische Entwicklungsarbeit führte zu einem gekoppelten Modell, welches die Anregung von Schwerewellen durch einzelne Konvektionszellen bis hin zu großskaligen Konvektionsclustern beschreibt. Außerdem wurden vorhandene Beschränkungen von Satelliteninstrumenten berücksichtigt, so dass ein direkter Vergleich der Simulationsergebnisse mit Messungen möglich wurde. Der sogenannte *observational filter* eines Satelliteninstruments schränkt hierbei die Beobachtung von Schwerewellen auf solche mit einer horizontalen Wellenlänge größer als ca. 100km ein. Allerdings zeigen die Verteilungen von horizontalen Wellenlängen konvektiver Schwerewellen nicht zu vernachlässigende

---

Beiträge im Bereich von Horizontalwellenlängen kürzer als 100km. Der letzte Teil dieser Dissertation ist deshalb dieser Diskrepanz zwischen simuliertem und beobachtbarem Schwerewellenspektrum gewidmet. Der direkte Vergleich zwischen Simulation mit *observational filter* und Satellitenmessungen zeigt dabei eine bemerkenswerte Übereinstimmung in den Impulsflussverteilungen.

# Contents

<b>1. Introduction</b>	<b>1</b>
<b>2. Gravity wave physics and observations</b>	<b>15</b>
2.1. Theoretical basics . . . . .	15
2.2. Limb-sounding measurements . . . . .	22
<b>3. Gravity wave ray-tracing</b>	<b>27</b>
3.1. Introduction . . . . .	27
3.2. Mathematical background . . . . .	28
3.3. The GROGRAT gravity wave ray-tracer . . . . .	31
3.4. The non-orographic launch distribution . . . . .	34
3.5. Comparison with satellite measurements . . . . .	37
<b>4. Oblique vs. vertical propagation of gravity waves</b>	<b>43</b>
4.1. Introduction . . . . .	43
4.2. Model setup . . . . .	46
4.3. Results . . . . .	49
4.4. Differences between oblique and vertical propagation	54
4.5. Meridional drag . . . . .	57
4.6. Poleward propagation . . . . .	60

## Contents

---

4.7. Influence of wind filtering and the Coriolis effect . . .	64
4.8. Further potential mechanisms: local Coriolis and remote recoil effect . . . . .	72
4.9. Summary and Discussion . . . . .	74
<b>5. Ray-tracing simulations of convective gravity waves</b>	<b>81</b>
5.1. The Yonsei convective gravity wave source model . .	81
5.1.1. Overview . . . . .	81
5.1.2. Mathematical description . . . . .	84
5.1.3. Implementation and coupling with GROGRAT	89
5.1.4. Application using the Merra dataset . . . . .	93
5.1.5. Source level momentum flux . . . . .	98
5.2. Ray-tracing of convective gravity waves . . . . .	100
5.3. Simulated convective gravity waves in comparison to satellite measurements . . . . .	119
5.3.1. Limitations due to the observational filter . .	119
5.3.2. Results . . . . .	122
5.3.3. Comparison of global ray-tracing and satellite data . . . . .	129
5.4. Summary and Outlook . . . . .	136
<b>6. Summary and Outlook</b>	<b>139</b>
<b>A. Appendices</b>	<b>149</b>
A.1. Wind filtering of gravity waves . . . . .	149
A.2. Timeseries of convective gravity waves . . . . .	151

A.3. Gravity wave ray-tracing as a parametrization for atmospheric circulation models . . . . .	157
A.3.1. Overview of the HAMMONIA GCM . . . . .	157
A.3.2. Technical implementation . . . . .	158
<b>Bibliography</b>	<b>162</b>

# 1. Introduction

Atmospheric gravity waves can exist and propagate within any stratified fluid (e.g. atmosphere, ocean) with gravity acting as the restoring force. It is therefore assumed that they can be found in the Earth's atmosphere as well as in the atmosphere of other planets [Collins *et al.*, 1997, Joshi *et al.*, 2000, Baker, 2000]. Vertical wavelengths of gravity waves in the Earth's atmosphere are typically as long as a few hundred meters up to a few ten kilometers. Their horizontal wavelengths are of the order of one kilometer to several thousand kilometers. Gravity waves propagating through the atmosphere occasionally produce clouds with a band-like structure, which can be observed from ground and from space. Figure 1.1 shows an example of such band-like clouds observed from space. This image was taken by the NASA MODIS (Moderate-resolution Imaging Spectroradiometer) imager during the passage of the southern Indian Ocean showing the Island of Amsterdam.

This picture is an example for one of the most important sources of gravity waves - orography. A vertically displaced wind flow over a topographic obstacle results in an oscillation of air parcels. After passing the obstacle (the Island of Amsterdam indicated by the red

arrow and in magnification in the upper left corner of Figure 1.1) the air flow starts to oscillate around its altitude of rest. The constant interaction of gravity and buoyancy force counter-acting on the air flow is responsible for the oscillation of the air flow behind the obstacle. Hereby, buoyancy, as the opposing force of gravity, displaces the air flow to higher altitudes again. Due to (quasi-)adiabatic decompression the air flow is cooled at every wave crest. Water vapor within the air flow condenses at the cold wave crests and evaporates again in the warm troughs which results in the typical wave pattern shown in Figure 1.1.

Besides orography, several other gravity wave sources are known. For instance convective storms and fronts or the gravity wave generation by imbalances of strong wind jets. The most relevant of these sources are located in the troposphere and tropopause region. From these primarily tropospheric sources, gravity waves propagate upward and thereby transport momentum and energy to higher altitudes. Finally, wave-breaking, dissipation, and the release of momentum dominate the momentum budget in the mesosphere. During the upward propagation gravity waves can also travel large horizontal distances. This is an effect often neglected in models.

Wave-breaking plays also an important role at the lower altitudes of the tropopause. There it acts as a prominent source of clear air turbulence (CAT) and affects aviation, which may cause severe hazards for airplanes [Eckermann, 2000]. Both examples demonstrate that gravity waves can transport large amounts of momentum and energy from source regions over far distances. [Booker and Brether-

---

ton, 1967, Bretherton, 1969]. The interaction of gravity waves with the mean-flow is of particular interest. Thus, one of the most im-

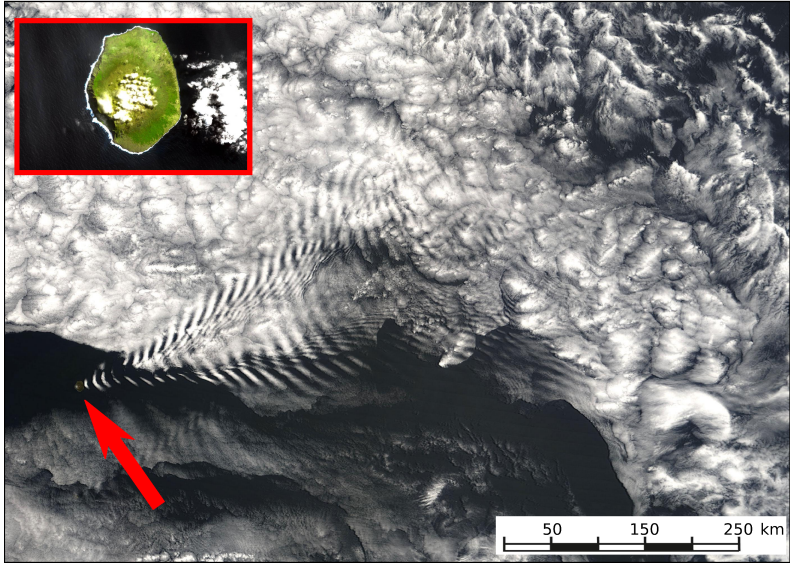


Figure 1.1.: An orographic gravity wave forced by the wind blocking topography of the Island of Amsterdam (red arrow and magnification in the upper left corner) in the southern Indian Ocean. Original picture taken by NASA (MODIS imager on board of the Terra satellite).

portant examples of the effect of gravity waves in the middle atmosphere is the interaction with the quasi-biennial-oscillation (QBO) [Reed *et al.*, 1961]. Gravity waves are wind-filtered during their upward propagation with respect to the QBO phase. On the other

hand, *Lindzen and Holton* [1968] showed that the observation of the QBO can be explained by a combined model of Kelvin- and gravity waves, which generate the QBO as verified in lab experiments [*Plumb and McEwan*, 1978]. However, the quantitative contribution of planetary waves and gravity waves in driving the QBO is still an open question [*Dunkerton*, 1997, *Ern et al.*, 2014].

A first simplified model of gravity waves propagating through the atmosphere and interacting with the background flow was proposed by *Lindzen* [1981]. This model was a break-through despite its simplifications. For the first time, the effect of unresolved gravity waves could be represented in atmospheric models. Henceforth, mesospheric wind-structures became understandable [*Holton*, 1982]. These first Lindzen parametrizations were developed towards more realistic multi-wave models taking into account wave saturation due to non-linear effects [*Hines*, 1997, *Warner and McIntyre*, 1999]. Consequently, *McLandress* [1998] and *Holton and Alexander* [1999] addressed the contribution of gravity wave momentum flux deposition to the dynamics of the middle and upper atmosphere. These studies suggest that the residual meridional circulation (Brewer-Dobson circulation), as shown in Figure 1.2, is not primarily driven by the upwelling of warm tropical air and the down-welling of cold air above the poles. Instead, atmospheric wave-breaking (gravity waves and planetary waves) in the middle atmosphere accelerates the zonal wind and, by interaction with the Coriolis force, becomes a major driver of the meridional circulation. Due to mass conservation this also induces a vertical motion. This effect is also referred to

---

as *Gyroscopic Pumping* [Holton *et al.*, 1995, McIntyre, 1998, 1999]. This momentum transfer due to gravity waves is prominent in the mesosphere, but also not negligible in the stratosphere (even though the major contribution of the momentum budget in the stratosphere originates from planetary waves). Indeed, *Alexander and Rosenlof* [2003] showed the importance of gravity wave mean-flow interaction for the lower stratospheric branch of the Brewer-Dobson circulation (lower grey arrows in Figure 1.2). Further, *McLandress and Shepherd* [2009] and *Butchart et al.* [2010] estimated the influence of gravity wave breaking to a predicted trend of the stratospheric summertime branch to be larger than 50 percent.

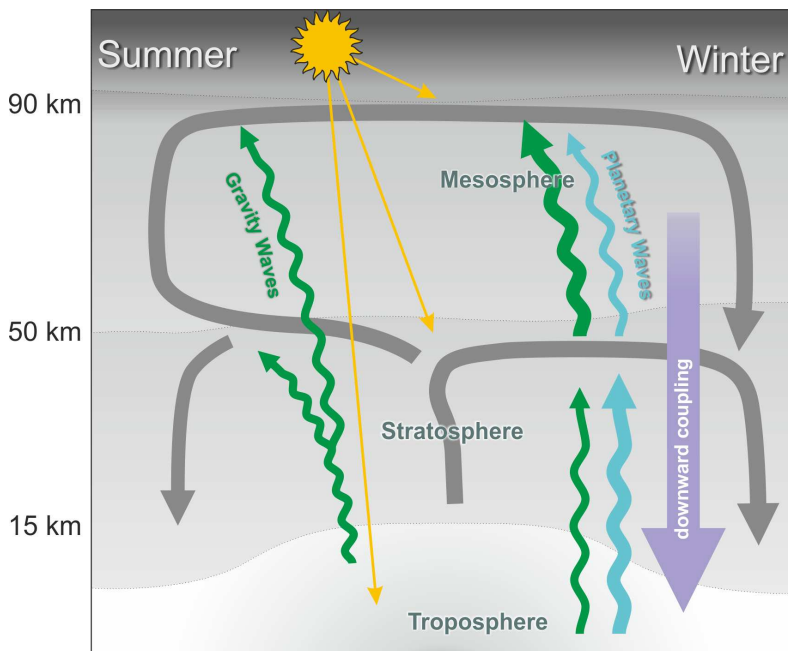


Figure 1.2.: Impact of gravity waves on the atmospheric mean circulation (Brewer-Dobson circulation). Gravity waves (green) propagate from their sources in the troposphere through the middle atmosphere and finally break in the mesosphere, where they contribute to the upper branch of the Brewer-Dobson circulation. Planetary waves (blue) are forced in the winter hemisphere, interact with gravity waves, and contribute to the lower branch of the circulation. As a result the net mass flux is downward directed from the mesosphere to the lower stratosphere - an effect referred to as “gyroscopic pumping” [Holton *et al.*, 1995, McIntyre, 1998, 1999]. “Downward coupling” describes the impact on the tropospheric circulation. (Figure with courtesy of Karlheinz Nogai.)

---

Momentum transfer from gravity waves also occurs at lower altitudes, e.g. at the source of their excitation. It follows from Newton's law of actio vs. re-actio [Newton, 1687] that there is a momentum transfer at the source level acting on the source itself. In case of orographic gravity waves this is the Earth's surface [Egger, 2000]. For convective gravity waves this interaction occurs at the top of the convection [Chun *et al.*, 2001] and can influence the angular momentum budget in tropical cyclones, typhoons, and hurricanes [Chimonas and Hauser, 1997].

Another example for the impact and importance of gravity waves can be found in atmospheric chemistry. Ozone depletion [Molina and Rowland, 1974] in the winter polar vortex strongly depends on low temperatures and the formation of polar stratospheric clouds (PSCs). PSCs are responsible for chlorine activation and therefore ozone depletion in the stratosphere which in case of Antarctica forms the remarkable and well known ozone hole [Farman *et al.*, 1985]. Model simulations indicate that ozone depletion starts already at higher average temperatures in the presence of gravity waves [McDonald *et al.*, 2009]. Considering a gravity wave in temperature, the temperature minimum can be low enough to locally produce PSCs even though the average temperature of the local atmosphere might be too high [Carslaw *et al.*, 1999]. These examples show that even though gravity waves are a small-scale phenomenon their contribution to the atmosphere's dynamic and chemistry is of global scale.

To address such a problem of multiple scales within a model of the Earth's atmosphere, gravity wave generation and propagation

have to be explicitly described in terms of parametrizations. For different gravity wave sources like orography, fronts, and convection parametrizations are included into global circulation models (GCMs). Most GCMs implement an orographic parametrization for gravity waves generated by wind-flow over mountain ridges [*Lott and Miller, 1997*]. Other sources of gravity waves are typically represented by a non-orographic parametrization with homogeneous and isotropic launch parameters [e.g. *Hines, 1997*]. The general importance of gravity wave launch spectra (e.g. in terms of horizontal wavelengths, phase speeds, and launch amplitudes) have already been investigated [*Manzini and McFarlane, 1998, Charron et al., 2002, Richter et al., 2010*]. Still, the parametrization of sources remain challenging and unsatisfactory [*Kim et al., 2003, Geller et al., 2013*]. It is therefore crucial to determine appropriate launch parameters (tuning) of the gravity wave spectrum in terms of phase speed, amplitude, and horizontal wavelength at launch altitude [*Medvedev and Klaassen, 2001, Preusse et al., 2008, 2009*]. Even with thoroughly tuned launch distributions, climate feedbacks on the launch spectrum of gravity waves cannot be represented by a static launch spectrum.

For this reason, measurements of gravity wave momentum flux distributions and phase-speed spectra associated with various sources are important. Different measurement techniques exist. In-situ measurements can resolve small-scale gravity waves with short horizontal wavelengths, but are restricted in their location. Satellite instruments on the other hand measure on a global scale, but have

---

limited sensitivity in detecting small-scale gravity waves. In particular, gravity waves with horizontal wavelengths shorter than 100km are a challenge for the detection by limb-sounding instruments. A major part of the horizontal wavelength spectrum with wavelengths longer than 100km can be observed [Preusse *et al.*, 2008, Alexander *et al.*, 2010a]. Accelerations of the mean-flow due to gravity waves (gravity wave drag) derived from those visible parts of the horizontal wavelength spectrum already contribute considerably to the entire zonal momentum budget [Ern *et al.*, 2011, 2013, 2014]. Climatologies are available for time spans covering more than 10 years [Ern *et al.*, 2014]. However, in-situ measurements show that short horizontal wavelengths of gravity waves that are not visible to limb-sounders are in particular important in regions of deep convection [Dewan *et al.*, 1998, Choi *et al.*, 2009, 2012, Ern and Preusse, 2012, Joutoukoff *et al.*, 2013]. The disadvantage of in-situ measurements are their spatial and temporal limitations. For instance, radiosondes cover altitude ranges up to 30km only and are lacking a global coverage. For this reason, the relative contributions of different horizontal scales of gravity waves still remain uncertain. Therefore, we rely on models of convective gravity waves for a detailed investigation. Part of this thesis is to address this problem of horizontal scales using a convective gravity wave model.

In order to parametrize gravity waves within GCMs, some simplifying assumptions have to be introduced to reduce the computational effort. The impact of these assumptions has to be verified and tested against observational data to improve the quality of grav-

ity wave parametrizations. One of these common assumptions of non-orographic gravity wave parametrizations is the homogeneous and isotropic launch distribution of waves. In contrast to common parametrizations, the horizontal propagation of gravity waves is considered in this thesis by using the method of gravity wave ray-tracing. This implies the following question:

**Can gravity wave ray-tracing with a homogeneous and isotropic source resemble major features in the gravity wave momentum flux distribution as observed by satellite instruments?**

To answer this question, the GROGRAT gravity wave ray-tracing model was used with a non-orographic background parametrization after *Preusse et al.* [2009]. The results of these calculations are compared to SABER (Sounding of the Atmosphere using Broadband Emission Radiometry; [*Mlynczak*, 1997, *Russell et al.*, 1999, *Yee et al.*, 2003, *Remsberg et al.*, 2008]) satellite limb-measurements.

Gravity wave parametrizations used in GCMs commonly assume a vertical-only propagation of gravity waves for the advantage of lower computational effort. This assumption simplifies the propagation to some extent, a major question *Lindzen* [1981] already asked:

**How does the vertical-only assumption of gravity wave propagation affect the patterns of gravity wave accelerations in the middle atmosphere?**

---

Chapter 4 addresses this question and shows how the vertical-only assumption of gravity wave propagation affects the distribution of the gravity wave drag and therefore the acceleration of the atmospheric background. In order to allow for effective parallelization of GCMs, all parametrizations described above<sup>1</sup> consider the propagation of gravity waves only inside individual vertical columns of the GCM grid. In practice, this implies that gravity waves are not allowed to propagate obliquely. This is in contradiction to gravity wave theory [e.g. *Lighthill*, 1967, *Andrews et al.*, 1987] and observations. Oblique propagation has been observed for an individual wave event [*Sato et al.*, 2003]. Also, other observations indicate propagation away from the source [e.g. *Taylor and Hapgood*, 1988, *Preusse et al.*, 2002, *Wu and Eckermann*, 2008]. On a statistical basis, observations indicate that, for instance, gravity waves from convective sources in the subtropics propagate poleward [*Jiang et al.*, 2004, *Ern et al.*, 2011, 2013] for almost 20° in latitude and thereby evade the wind reversal between tropospheric westerlies and stratospheric easterlies in the summer hemisphere [*Preusse et al.*, 2009]. This has consequences, for instance, for the representation of the Brewer-Dobson circulation, which is essentially driven by gravity waves in summer [*Alexander and Rosenlof*, 2003].

Two ray-tracing simulations have been set up to estimate the effect of the vertical-only assumption. One with vertical-only propagation of gravity waves and the second one with a free three-dimensional propagation of gravity waves. The resulting accelerations of the

---

<sup>1</sup>Besides single technical proof-of-concepts, e.g. *Song et al.* [2007]

background flow show some remarkable differences.

In addition, the assumption of a time independent homogeneous launch distribution for gravity waves remains as a rather unphysical representation of highly dynamic gravity wave sources like convection. This leads us to the following question:

**How does a convective gravity wave source model alter the global distributions of gravity wave momentum flux compared to a uniform gravity wave source?**

To answer this question, the Yonsei convective gravity wave source model [Song and Chun, 2005] is used. Chapter 5 introduces this model which, as a part of this work, has been coupled to the GRO-GRAT gravity wave ray-tracer. The results include some tuning of free parameters. Therefore, results from the coupled model simulations are compared to satellite observations of convective regions (e.g. tropics). However, it is an open question, whether the majority of convective gravity waves have wavelengths too short for a detection by limb-sounding instruments [Choi *et al.*, 2009, 2012]. Limb-sounding instruments like SABER are not able to detect waves of very short wavelength due to the so-called “observational filter” effect [Alexander, 1998]. This motivates the following question:

**How does the observational filter of infrared limb-sounding satellite instruments affect global momentum flux distributions and which part of the convective gravity wave spec-**

---

## trum is visible to satellite instruments?

This question will be answered in chapter 5. It is especially important for the evaluation of the quality of gravity wave modelling since it directly addresses constraints of satellite instruments in general. Satellites are the only way to access gravity wave distributions on a global scale for a long period of time. Their technical limitations in terms of sensitivity to gravity waves have been considered, for instance by *Preusse et al.* [2008]. Therefore, the aim of this thesis is to connect modelling and observations to achieve a more comprehensive picture of gravity waves and their excitation, propagation, and dissipation.

A brief overview of gravity wave theory and observations from limb-sounding instruments is given in chapter 2. The common method of ray-tracing to calculate gravity wave trajectories and momentum flux deposition is presented in chapter 3 together with a first comparison between ray-tracing results and satellite observations. Chapter 4 addresses the vertical-only assumption of state-of-the-art gravity wave parametrizations for a homogeneous launch distribution. Chapter 5 introduces the Yonsei convective gravity wave source model. Results from the source model coupled to the gravity wave ray-tracer GROGRAT are presented and compared to satellite observations. For this, observational constraints of limb-sounding remote sensing instruments are taken into account. Finally, a summary and outlook is given in chapter 6.



## 2. Gravity wave physics and observations

### 2.1. Theoretical basics

An overview on the basic properties of gravity waves is presented in this section. A more detailed presentation of the topic can be found in *Fritts and Alexander* [2003]<sup>1</sup>. An idealized air parcel in a stable atmosphere will start to oscillate when it is displaced<sup>2</sup> to a higher altitude without any exchange of heat with the surrounding air masses (adiabatic process). The temperature of this air parcel decreases and its density increases ( $T_2$  and  $\rho_2$  in Figure 2.1). With a higher density compared to the surrounding air, gravity force becomes stronger than the buoyancy force and the resulting force vector points downwards. The air parcel will therefore move downwards until buoyancy force is strong enough to overcome gravity and all of the remaining

---

<sup>1</sup>First theoretical work on gravity waves was done by *Wegener* [1906], *Lamb* [1910], and *Trey* [1919]. *Queney* [1948] performed first investigations on gravity waves excited by orography already in 1948.

<sup>2</sup>This displacement might for instance be introduced by a mountain disturbing the straight air flow and therefore forcing an upward propagation of air parcels.

## CHAPTER 2. GRAVITY WAVE PHYSICS AND OBSERVATIONS

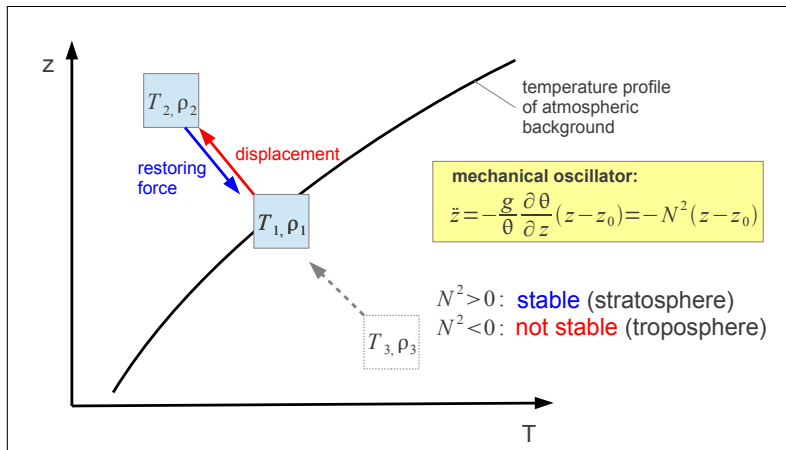


Figure 2.1.: Illustration of an air parcel oscillating around its equilibrium position. A displacement of the air parcel to a higher altitude implies a decrease in temperature and an increase in density (adiabatic process). Gravity then becomes the major force at the upper turning point resulting in a downward propagation of the air parcel until buoyancy becomes the governing force at the lower turning position. The whole behavior can be described (in a first order approximation) as a harmonic oscillator. Stable (oscillating) results are typically found in the stratosphere and unstable (non-oscillating) results may be found in the troposphere.

momentum is lost. The lower turning point is attained and due to the lower density compared to the surrounding air the resulting force vector now points upwards with the initial acceleration in the same direction. Neglecting frictional forces, this simple behavior can be

described by a harmonic oscillator model.

$$\ddot{z} = -N^2 \cdot (z - z_0) \quad (2.1)$$

here  $z$  denotes the actual vertical coordinate of the air parcel and  $z_0$  its vertical rest location. The squared buoyancy frequency  $N^2$  is the eigen-frequency of this oscillating system and is defined as

$$N^2 = \frac{g}{T} (\partial_z T - \Gamma) \quad (2.2)$$

In this definition  $\Gamma = -10\text{K/km}$  (the dry adiabatic lapse rate) accounts for the negative slope in temperature due to the negative density gradient with altitude. Equation 2.2 can be re-written in terms of potential temperature

$$\Theta = T (p/p_s)^\kappa \quad (2.3)$$

With  $\kappa = R/c_p \approx 2/7$  and  $p_s$  as the surface pressure. The potential temperature is the temperature that an air parcel at pressure  $p$  would acquire if adiabatically brought to standard pressure  $p_s$ . Using this definition yields the buoyancy frequency to be

$$N^2 = g \frac{T}{T_s} (\partial_z \ln \Theta) \quad (2.4)$$

Typical values of the periods ( $\hat{T} = 2\pi N^{-1}$ ) are 10-15 minutes within the troposphere and 5 minutes in the stratosphere. The largest change between both periods occurs within the tropopause

## CHAPTER 2. GRAVITY WAVE PHYSICS AND OBSERVATIONS

---

region and rapidly alters the propagation conditions of the wave. Thus, this region acts as a strong filter for gravity waves. As mentioned before, the oscillation of the air parcel also results in a periodical change in temperature. This is illustrated in Figure 2.2 with warm phases (red lines) and cold phases (blue lines). The air parcel

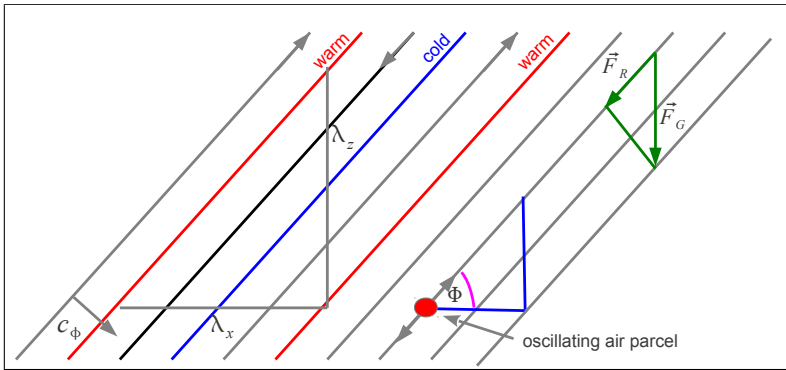


Figure 2.2.: Phase diagram of a gravity wave with vertical wavelength  $\lambda_z$  and horizontal wavelength  $\lambda_x$ . Blue lines indicate cold phases and red lines warm phases.

oscillates parallel to the phase fronts due to its resulting buoyancy force. To describe the physics of gravity waves in a simple algebraic way, the following dispersion relation is useful<sup>3</sup>.

$$\hat{\omega}^2 = \frac{N^2(k^2 + l^2) + f^2(m^2 + \frac{1}{4H^2})}{k^2 + l^2 + m^2 + \frac{1}{4H^2}} \quad (2.5)$$

<sup>3</sup>The general gravity wave dispersion relation presented here can be motivated by observation and by mathematical derivation. A detailed introduction on this topic can be found in *Fritts and Alexander* [2003].

In this equation  $\hat{\omega}$  is the intrinsic frequency,  $k, l$  are the horizontal wavenumbers,  $m$  is the vertical wavenumber, and  $N$  is the buoyancy frequency.  $H$  is the scale height, the altitude where the pressure is only  $1/e$  of the surface's pressure.  $f$  is the Coriolis factor given by  $f = 2\Omega \sin\phi$  with  $\phi$  as the latitude of the wave's position and  $\Omega$  as the Earth's angular velocity. It is known from observations [Fritts and Alexander, 2003] that for the vast majority of gravity waves the horizontal wavelength is much larger than the vertical wavelength. It is therefore straight forward to apply the mid-frequency approximation ( $k^2 + l^2 = k_h^2 \ll m^2$ ) to equation 2.5. Further, the Coriolis effect is often neglected ( $f \ll \hat{\omega}$ ), because typical values of the Coriolis factor for mid-latitudes are  $f \approx 10^{-4} \text{ s}^{-1}$ . As a result, equation 2.5 simplifies to:

$$\hat{\omega}^2 \approx \frac{N^2 k_h^2}{m^2 + 4H^2} \quad (2.6)$$

Equation 2.6 is in particular useful to understand the fundamental physics of gravity waves in terms of propagation. Thus, with the definition of the group velocity:

$$\hat{c}_g = \vec{\nabla}_{k,l,m} \hat{\omega} = \left( \frac{\partial \hat{\omega}}{\partial k}, \frac{\partial \hat{\omega}}{\partial l}, \frac{\partial \hat{\omega}}{\partial m} \right) = \left( \frac{\hat{\omega}}{k}, \frac{\hat{\omega}}{l}, -\frac{\hat{\omega}}{m} \right) \quad (2.7)$$

The phase velocity is defined by:

$$\hat{c}_\phi = \left( \frac{\hat{\omega}}{k}, \frac{\hat{\omega}}{l}, \frac{\hat{\omega}}{m} \right) \quad (2.8)$$

Phase and group velocity differ in sign. Conventionally, the intrinsic

## CHAPTER 2. GRAVITY WAVE PHYSICS AND OBSERVATIONS

---

frequency is defined positive and is accordingly chosen for an upward propagating wave (positive  $\hat{c}_{gz}$ ). The vertical wavenumber is negative resulting in a negative phase velocity  $\hat{c}_{\phi,z}$ . It is easy to show that  $\hat{c}_{\phi}$  is oriented perpendicular to the phase fronts and  $\hat{c}_g$  is oriented along the phase fronts as indicated in Figure 2.2. The example of Figure 2.2 shows upward propagating waves since many gravity wave sources are located in the troposphere and therefore in the middle atmosphere gravity waves are preferentially propagating upward. However, the generation of gravity waves at tropopause altitudes is indicated by upward propagation of gravity waves above the tropopause and downward propagation below the tropopause. In either way, the energy and momentum transported by gravity waves is connected to their temperature amplitude. The potential energy of a gravity wave is according to *Tsuda et al.* [2000] given by

$$E_{pot} = \frac{1}{2} \left( \frac{g}{N} \right)^2 \left( \frac{\hat{T}}{T} \right)^2 \quad (2.9)$$

with  $\hat{T}$  as the temperature amplitude of the wave and  $T$  as the background temperature. Assuming the ideal case of non-dissipative wave propagation without refraction ( $\vec{k} = 0$ ), the gravity wave (pseudo-)momentum flux<sup>4</sup> is conserved and the vertical flux of horizontal

---

<sup>4</sup>The term *pseudo-* indicates an eigenvalue of -1 of a point inflection transformation. Thus, the quantity in question is a pseudo-vector quantity [Andrews and McIntyre, 1978].

pseudo-momentum [Fritts and Alexander, 2003] is given by:

$$\vec{F} = \bar{\rho} \hat{c}_{gz} \frac{E}{\hat{\omega}} \vec{k} = \bar{\rho} (1 - f^2 / \hat{\omega}^2) (\overline{w'u'}, \overline{w'v'}) \quad (2.10)$$

The right hand side of equation 2.10 relates Reynolds stress and vertical flux of horizontal momentum to the pseudo-momentum flux assuming non-dissipative conditions. Radiative damping [Fels, 1984, Zhu, 1994], interactions between gravity waves, and wave-mean flow interactions [Lindzen, 1973] are also well known dissipative processes [Marks and Eckermann, 1995].

Gravity waves are often measured by their temperature variances or temperature amplitudes. For this purpose *Ern et al.* [2004] formulated the gravity wave momentum flux in linear theory as a function of gravity wave squared temperature amplitudes.

$$\vec{F} = \rho \frac{\vec{k}_h}{m} E_{pot} = \frac{\rho}{2} \frac{\vec{k}_h}{m} \left( \frac{g}{N} \right)^2 \left( \frac{\hat{T}}{\bar{T}} \right)^2 \quad (2.11)$$

The divergence of the momentum flux is proportional to the force exerted on the mean flow. In order to determine the effect on the background flow the gravity wave drag (GWD) is calculated to measure their contribution to the wind tendencies in atmospheric circulation models.

$$(X, Y) = -\frac{\epsilon}{\rho} \frac{\partial \vec{F}}{\partial z} \quad (2.12)$$

Here,  $X$  and  $Y$  are the vector components of the acceleration due to gravity wave forcing in zonal and meridional direction. The factor  $\epsilon$

was introduced as an efficiency [Holton, 1982] or intermittency [Fritts and Alexander, 2003] factor. It can be thought of as a representation of the fractional coverage of the wave dissipation event within the larger-scale space- and/or time-averaging interval. It may also act as a tuning factor within GCMs. It should be mentioned that GWD measurement uncertainties are usually as high as a factor of 2-3. Thus,  $\epsilon$  can be used to account for differences obtained in the direct comparison of model results and measurements.

## 2.2. Limb-sounding measurements

Limb-sounding instruments are widely used to answer scientific questions regarding atmospheric chemistry and dynamics. The basic measurement geometry of a typical limb-sounder is shown in Figure 2.3. The instrument, for instance on a satellite, points towards the horizon and detects incoming radiation from air along the line-of-sight [e.g. Riese *et al.*, 1999]. The part of the line-of-sight which is closest to the Earth's surface contributes the most to the observed spectrum. The reason for this weighted contribution along the line-of-sight is the exponential decay of density with altitude. The highest air density is found at the point closest to the Earth's surface. This point in the line-of-sight is called the tangent point. By slightly altering the elevation angle, the tangent point can be directed to different altitudes (and also to different horizontal positions). In this way, a complete vertical scan through the atmosphere can be achieved. This so-called limb-scanning is a common method

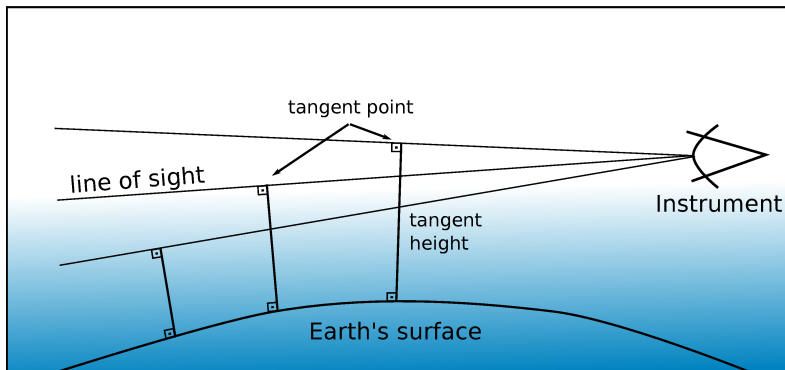


Figure 2.3.: Schematic overview of the limb-sounder geometry. The instrument optics aims through the atmosphere. Each "line-of-sight" is in parallel to one surface tangential. The measurement is (in a first-order approximation) Gaussian distributed along the line-of-sight with the tangent point as the region of major contribution. Therefore, small-scale horizontal structures are "smeared" or averaged along the line-of-sight which in particular affects the observation of gravity waves.

to derive vertical profiles of temperature and trace gases from measured infrared radiances from limb-sounding observations. The spatial resolution of remote sensing instruments is usually limited in the horizontal (represented by a weighting function) along the line-of-sight. This limitation has to be considered when measurements from limb-sounding instruments are compared to simulations. About 50% of the radiation originates from a 300km long segment along the line-of-sight *Riese* [e.g. 1994]. Assuming a sinusoidal wave along the line-of-sight the convolution of this wave with a Gaussian is given

by:

$$\frac{I}{I_0} = e^{-2\pi^2\sigma^2/\lambda_x^2} \quad (2.13)$$

With  $\sigma = 200\text{km}$  (50% radiation from a 300km line segment) and  $I/I_0 = 0.5$  the result is  $\lambda_x = 1000\text{km}$ . Thus, in this simple example waves are only detectable if their horizontal wavelength is longer than 1000km. Waves shorter than 500km encounter a reduced detection sensitivity. However, measurements by *Eckermann et al.* [2001], *Preusse et al.* [2003] suggest that these waves can be observed. The reason for this discrepancy is the wavelength shift introduced by the limb-sounding geometry as shown in *Preusse et al.* [2002]. The curvilinear line-of-sight is responsible for a longer observed wavelength compared to real wavelength of the gravity wave (Figure 2.4). It is therefore possible to measure gravity waves with shorter horizontal wavelengths than suggested by equation 2.13. Figure 2.4 shows a temperature wave field with the line-of-sight of a limb-sounder. At the tangent point, the horizontal wavelength is obtained to be close to the real wavelength. However, parts of the line-of-sight, which are more distant from the tangent point are only sensitive to a much longer wavelength. Since line-of-sight measurements are usually convolved with a weighting function (e.g. Gaussian). Then the average horizontal wavelength obtained is longer than the real horizontal wavelength of the wave. Therefore, gravity waves with wavelengths shorter than the detection limit derived from Eq.2.13 can still be measured. In other words, the sensitivity for shorter horizontal wavelengths measured by limb-sounding instruments is

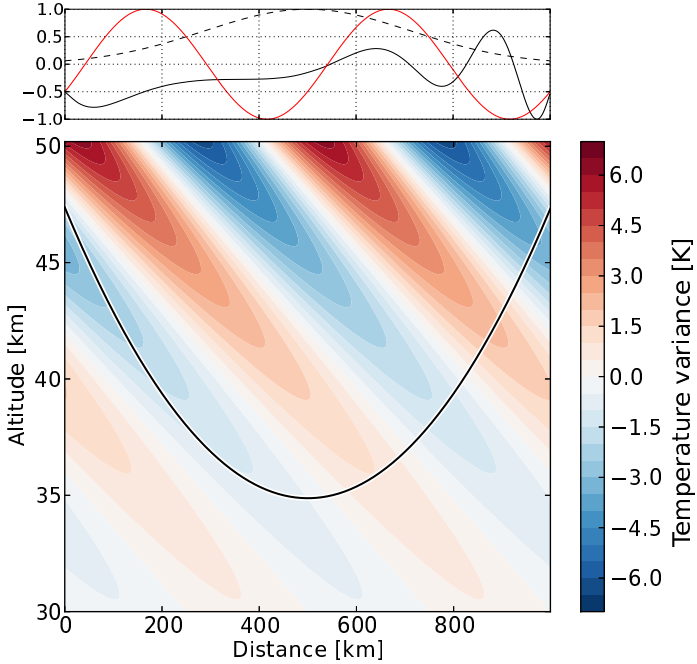


Figure 2.4.: Limb-sounding measurement geometry causes a shift in wavelength, thus, parts of the convective gravity wave spectrum become visible to the instrument. The black line indicates the line-of-sight in a wave-like temperature field. The smaller plot on top shows the measured (normalized) temperature along the line-of-sight (black solid line), the weighting function (black dashed line) and the altitude cross-section at 35 km altitude (red solid line).

increased<sup>5</sup>.

<sup>5</sup>Tomographic limb-sounding might solve this kind of gravity wave wavelength measurement problem [Ungermaun *et al.*, 2010].



## 3. Gravity wave ray-tracing

### 3.1. Introduction

Many problems in applied fluid dynamics and even more general, field theory, involve the task of solving partial differential equations (PDE) - equations of a function and its derivatives with respect to more than one variable. In contrast to the well developed theory of ordinary differential equations (ODE), yet no theorem of existence and uniqueness of a solution exists. Nevertheless, for some PDEs general solutions have been found. In many cases quasi-linear<sup>1</sup> PDEs can be solved using the method of characteristics. This method was first introduced by *Huygens* [1678] and identifies solutions of a wave-field with rays propagating orthogonal to the wave fronts. These rays can be referred to as the tracks of particles travelling at a certain velocity (termed group velocity) through the space. With this famous work of Huygens, the duality of waves and particles was founded and tracing tracks of rays became a valuable method of solving field-like PDEs. In this section the method of gravity wave

---

<sup>1</sup>A quasi-linear PDE is linear in the derivatives, but not necessarily in the related coefficients.

ray-tracing is briefly introduced as well as the computer programme GROGRAT (Gravity wave Regional Or Global RAY-tracer) [Marks and Eckermann, 1995] which is commonly used for basic studies and more importantly: the method of global gravity wave ray-tracing. This method of deriving (pseudo-)momentum flux, temperature amplitude, and drag (the momentum transfer of a gravity wave to the background) was introduced in *Preusse et al.* [2006, 2009]. For this purpose, 14 spectral components of gravity wave phase-speed, launch amplitude, and horizontal wavelength have been chosen in accordance to global satellite observations to resemble measured temperature amplitudes up to the lower thermosphere. The final comparison of the ray-tracing simulations showed already a remarkable good agreement with measured global momentum flux and temperature amplitude distributions [Preusse et al., 2009].

## 3.2. Mathematical background

The mathematical description of gravity waves within a background flow is a multi-scale problem with gravity waves acting on a smaller scale with comparably small amplitudes. A convenient ansatz is to reduce the complexity of the problem by separating between a large-scale background flow and small-scale perturbations. It is applicable to choose a linear perturbation ansatz for the background flow

$$\vec{U} = \vec{U}_0 + \vec{U}' \tag{3.1}$$

### 3.2. MATHEMATICAL BACKGROUND

---

with  $\vec{U}$  the zonal wind,  $\vec{U}_0$  the background and  $\vec{U}'$  the small-scale zonal wind perturbations. The latter can be further divided apart into periodical (wave-like) and non-periodical (e.g. turbulence) parts. Here, only the wave-like part is of interest.

$$\vec{U}' = \text{Re} \left\{ \hat{U}(\vec{x}, t) \exp[i\chi(\vec{x}, t)] \right\} \quad (3.2)$$

$\hat{U}$  represents the amplitude of the solution. Usually this wave amplitude is governed by a term growing exponentially with altitude. The reason is that gravity wave amplitudes grow proportional to  $\exp(z/2H)$  up to the saturation limit [Lindzen, 1981]. On the other hand, the periodical part of the solution can be represented by using a phase-function  $\chi$  with the following partial derivations:

$$k = \partial_x \chi \quad (3.3a)$$

$$l = \partial_y \chi \quad (3.3b)$$

$$m = \partial_z \chi \quad (3.3c)$$

$$\hat{\omega} = -\partial_t \chi \quad (3.3d)$$

The three wavenumbers  $k$ ,  $l$  and  $m$  form the wavevector  $\vec{k}$  and  $\hat{\omega}$  is given by the dispersion relation 2.5. To investigate the propagation of gravity waves as seen by an observer on the surface of the Earth, a transformation from the center of the wave packet moving with the background flow to the system of the observer at rest has to be applied. Therefore, the time derivative has to be replaced by an

operator accounting for the motion of the wave packet with respect to an observer at rest

$$\mathbf{d}_{g,t} = \partial_t + \vec{c}_g \circ \vec{\nabla} \quad (3.4)$$

with  $\vec{c}_g$  as the ground-based group velocity of the wave packet. The ground-based change of the wavevector  $\vec{k}$  can now be obtained by applying this operator  $\mathbf{d}_{g,t}$  to equations 3.3a

$$\mathbf{d}_{g,t}k = -\partial_x \hat{\omega} \quad (3.5a)$$

$$\mathbf{d}_{g,t}l = -\partial_y \hat{\omega} \quad (3.5b)$$

$$\mathbf{d}_{g,t}m = -\partial_m \hat{\omega} \quad (3.5c)$$

$$\mathbf{d}_{g,t}\hat{\omega} = \partial_x \hat{\omega} \quad (3.5d)$$

As a result, the trajectory calculation of a single gravity wave packet can now be written as the ground-based change of the position of the wave packet's position  $\vec{x}$

$$\mathbf{d}_{g,t}\vec{x} = \vec{c}_g \left[ \vec{k}(\vec{x}(t), t), \vec{x}(t), t \right] \quad (3.6)$$

Equations 3.5 and 3.6 are known as the gravity wave ray-tracing equations. They were first formulated by *Lighthill* [1967] in the context of gravity waves. It is possible to generalize from the underlying geometry. As a result the gravity wave trajectory calculation can be performed on an approximate Cartesian grid as well as in spherical

coordinates. A more modern and coordinate free representation of both equations can be found by substituting partial derivations  $\partial_i$  on single components of  $\vec{k}$  by  $\vec{\nabla}_{\vec{k}}$

$$\dot{\vec{x}} = \vec{U}_0 + \vec{\nabla}_{\vec{k}} \omega \quad (3.7a)$$

$$\dot{\vec{k}} = \vec{\nabla} \left( \vec{k} \cdot \vec{w} - \omega \right) \quad (3.7b)$$

### 3.3. The GROGRAT gravity wave ray-tracer

The GROGRAT ray-tracer was developed by *Marks and Eckermann* [1995] as a new tool to describe and calculate the propagation of non-hydrostatic gravity waves. Earlier approaches [*Dunkerton*, 1984] for hydrostatic waves were already able to reproduce the critical-level filtering effect [*Lindzen*, 1981] as a major contribution to the obtained filtering of waves with horizontal wavelengths between 50-200km. The GROGRAT model implemented for the first time the full gravity wave dispersion relation including both, the Coriolis force and higher frequency non-hydrostatic gravity waves, which may carry a large part of the (pseudo-)momentum flux. Calculations are performed in a full three-dimensional background atmosphere including, if provided, also temporal variations of the background. Further advances were the implementation of radiative and turbulent damping and amplitude saturation. The structure of GROGRAT is illustrated in Figure 3.1 and the individual processes are described in the following paragraphs.

The trajectory calculation (left light blue box of Figure 3.1) follows the mathematical description of *Lighthill* [1967] with a Runge-Kutta solver for the numerical integration. For conservative propagation of gravity waves, the wave action is a conserved quantity. However, there is continuous wave dissipation by turbulence and infrared radiation. In particular, waves strongly dissipate when saturation and wave-breaking occurs. This is implemented by a time constant  $\tau$  as a decay factor, thus the wave's amplitude is not exactly conserved. This decay factor accounts for two different kinds of amplitude damping. Radiative damping caused by the temperature difference in the warm and cold phase of the wave is parametrized according to *Zhu* [1994]. Amplitude damping due to interaction with turbulent layers of the atmosphere is calculated according to the scheme of *Pitteway and Hines* [1963]. Finally, amplitude saturation [*Fritts and Rastogi*, 1985] is also applied to restrict the amplitude growth above a certain saturation amplitude  $\hat{u}^*$ .

### 3.3. THE GROGRAT GRAVITY WAVE RAY-TRACER

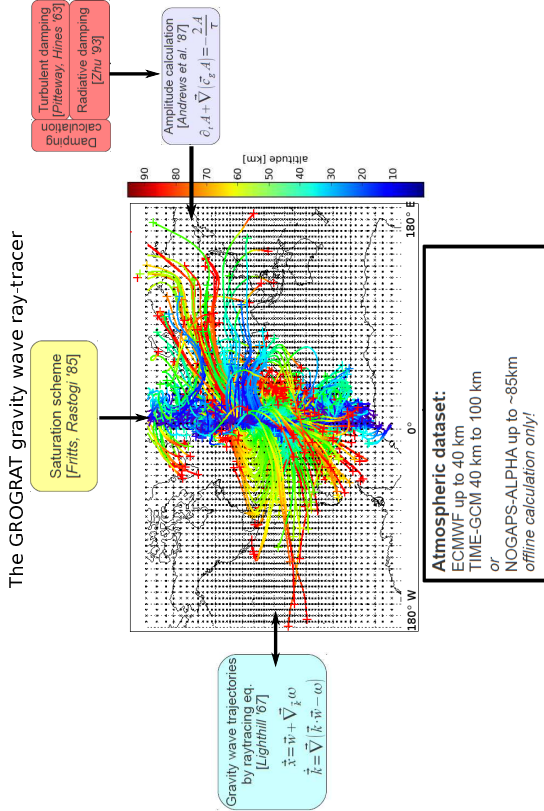


Figure 3.1.: Schematic overview of the GROGRAT gravity wave ray-tracer. Trajectories (center of this figure) are calculated using a Runge-Kutta integrator. Additionally various saturation and damping schemes can be used to parametrize wave action amplitudes. Further, propagation details like vertical only propagation or free oblique trajectory calculation can be configured. ECMWF, Merra and NOGAPS-ALPHA dataset have been used for the studies of this thesis.

Several different datasets with different gridpoint geometries may serve as a source for the atmospheric background data. For this thesis, various datasets have been used. Also, launch positions, directions, wavelengths, and intrinsic frequencies of the waves are important. These gravity wave launch conditions represent the sources of gravity waves. Various gravity wave sources like orography and convection have been studied so far<sup>2</sup>, but there is still a need for a gravity wave background parametrization. The latter implements launch conditions with the common equally distributed locations and launch directions of a well chosen gravity wave wavelength and frequency spectrum. For this particular work the gravity wave spectrum from *Preusse et al.* [2009] was used, because it was derived by tuning the spectrum against satellite observations. The advantage is the accuracy in physical modelling achieved by using as many observations as possible. But, as shown in section 5.3, this method includes only the observable parts of the gravity wave spectrum, thus, the modelling follows the instruments limitations<sup>3</sup>.

### 3.4. The non-orographic launch distribution

The ray-tracing method introduced in the last chapter is a well-known method of solving differential equations of wave type. In case of an inhomogeneous medium like the Earth's atmosphere the

---

<sup>2</sup>Even though the physical modelling of these sources has still to be improved.

<sup>3</sup>For instance, convective gravity waves have strong (pseudo-)momentum flux contributions within the <500km horizontal wavelength spectrum, which are hard to observe by limb-sounding instruments.

### 3.4. THE NON-OROGRAPHIC LAUNCH DISTRIBUTION

---

so called WKB approximation has to be applied first<sup>4</sup>. To solve the problem of gravity wave propagation some boundary conditions (in a mathematical sense) are needed. The physical interpretation of these boundary conditions is the location and direction of the gravity wave source as well as an initial amplitude and wavelength. The most obvious boundary condition is topography. As a result, orographic gravity waves have already been studied and most GCMs include an orographic gravity wave parametrization (e.g. *Lott and Miller [1997]*). The remaining sources of gravity waves are often parametrized by a so-called non-orographic parametrization (e.g. *Hines [1997]*<sup>5</sup>). Typically a non-orographic parametrization consists of equally distributed launch positions (a longitude-latitude grid at a given altitude) with several launch directions. Additionally, gravity wave amplitude, horizontal wavelength, and phase speed at launch location have to be defined. Ideally, these free parameters should be derived from measurements. This has been done in *Preusse et al. [2009]* for northern hemisphere summer conditions. The launch parameters needed are not directly accessible and had to be estimated indirectly from observed small-scale temperature fluctuations. The gravity wave temperature data needed were derived from SABER observations and have been compared to several setups of assumed non-

---

<sup>4</sup>The WKB approximation, named after Gregor Wentzel, Hendrik Anthony Kramers and Leon Brillouin [*Wentzel, 1926*], was originally introduced in quantum mechanics to solve the Schroedinger-equation in case of slowly varying potentials.

<sup>5</sup>The Hines parametrization uses a different non ray-tracing approach for solving the gravity wave propagation problem. Besides this differences, the boundary conditions are of non-orographic type.

horiz. wl	$\lambda_h$	phase speed	$c_{ph}$	amplitude	$\hat{u}$	IMF
	km		$\text{ms}^{-1}$		$\text{ms}^{-1}$	
	500		3		6.00	20
	500		10		20.00	5
	500		20		2.00	5
	500		30		1.00	5
	500		30		0.20	10
	500		40		0.10	20
	500		50		0.05	50
	500		90		0.05	60
	1500		30		1.00	20
	2000		15		2.00	30
	2000		60		0.20	20
	2000		60		0.05	60
	2000		30		1.00	20
	3000		30		6.00	5

Table 3.1.: Spectral parameters of the non-orographic parametrization according to *Preusse et al.* [2009]. Horizontal wavelength, phase speed, and launch amplitude are derived from SABER temperature measurements. Intermittency factors (IMF) represent the relative weight (representing the relative occurrence of each wave) of a single spectral component (SCE).

orographic boundary conditions by ray-tracing. By super-imposing several single spectral components (SCEs in *Preusse et al.* [2009]) and adjusting weighting factors of each component accordingly, a launch spectrum consisting of 14 single spectral components was derived. Table 3.1 summarizes those launch parameters. As a result, the estimated start parameters have a physical foundation and the launch spectrum can be regarded as realistic. This non-orographic

parametrization will be used (if not mentioned differently) in the following sections. In section 5 parts of this parametrization will be substituted by a more physical source model for convective gravity waves.

## 3.5. Comparison with satellite measurements

In *Preusse et al.* [2009] the gravity wave launch distribution was derived indirectly based on a fit on SABER observations. Single components of a phase speed and horizontal wavelength spectrum were superimposed using single wave intermittency and amplitudes suitable to reproduce the satellite measurements. In fact, the fitting was done for July 2004 TIME-GCM (Thermosphere Ionosphere Mesosphere Electrodynamics - General Circulation Model, *Roble and Ridley* [1994]) data. ECMWF<sup>6</sup> data were used for the necessary lower altitude forcing of the TIME-GCM, thus, the resulting atmospheric dataset consists of ECMWF data for altitudes up to 40km and of TIME-GCM data for altitudes from 40km to 120km with a smooth transition in between. Also, the derivation was done with temperature squared amplitudes since they are a direct result of the gravity wave retrieval from SABER temperature data. This raises the questions on how sensible this tuning of the gravity wave spectrum is if a different atmospheric dataset is used. It is also important

---

<sup>6</sup>European Centre for Medium-Range Weather Forecasts

to understand how the spectrum from *Preusse et al.* [2009] resembles the seasonal cycle and if it can reproduce momentum flux distributions of gravity waves from different sources. These sources might be localized (e.g. orography) and dynamic (e.g. convection, fronts). Hence, it is not obvious that a homogeneous isotropic and static launch distribution is able to represent all these different sources.

Figure 3.2 shows absolute momentum flux data derived from temperature amplitudes [*Ern et al.*, 2011] at 30km and 50km altitudes for January and July 2008. First of all, momentum flux decreases from 30km to 50km and the different colorbars of the logarithmic plot in Figure 3.2 address that. Secondly, the respective winter hemisphere shows the highest momentum flux values for both months and altitudes. Maximums due to orographic gravity waves above Europe and North America are prominent in January. The higher momentum flux values above the Atlantic Ocean indicate convective storms as one possible source. However, the generation process might be a combination of convection, geostrophic adjustment, and due to instabilities close to weather fronts. *Chun et al.* [2011] used WACCM<sup>7</sup> simulations to show that convective gravity waves are a major contributor to the overall forcing of the atmosphere. Convective forcing was also found to be prominent at extra-tropical latitudes.

The July data are dominated by high momentum fluxes around 50°S where the amplitude of gravity waves increases due to strong west wind regimes, which are in contrast to the northern hemisphere not disturbed by continents. Particularly high momentum

---

<sup>7</sup>Whole Atmosphere Community Climate Model

### 3.5. COMPARISON WITH SATELLITE MEASUREMENTS

#### SABER satellite measurements of absolute momentum flux

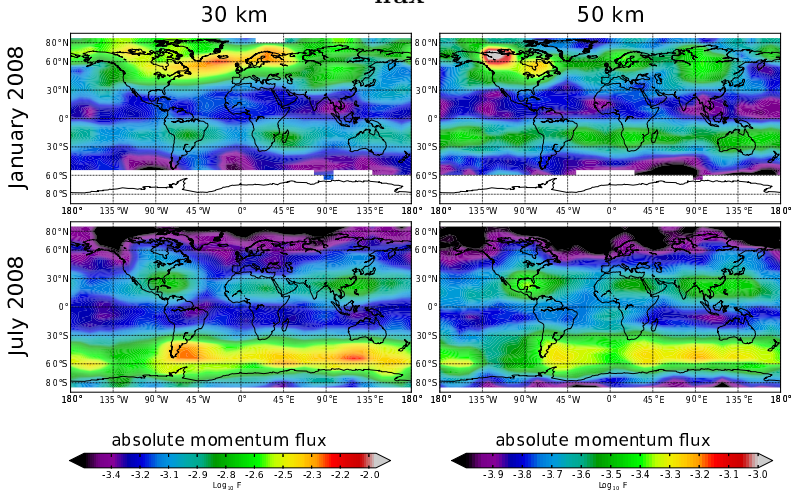


Figure 3.2.: Absolute momentum flux from SABER observations at 30km and 50km altitude for January and July 2008. Prominent features are the higher momentum flux values in the winter hemisphere and the higher momentum flux values above the continents in the tropics from convectively forced gravity waves. Also remarkable are the high momentum flux values in the lee of the Andes in July (30km). A different colorscale was used for the 50km altitude data due to lower momentum flux values as a result of wave dissipation.

flux values are observed in the region between South America and the Antarctic Peninsula. They are the result of gravity wave excitation by air flow over topography.

Figure 3.3 shows absolute momentum flux for January and July

2008 at 30km and 50km altitude as a result of gravity wave simulations performed by the GROGRAT ray-tracer. Maximums above Europe and North America are well represented for January conditions. The low latitude maximums at  $15^{\circ}\text{S}$  are westward shifted and not very localized above the continents. This is a direct result from the homogeneous launch distribution, which does not account for localized sources such as convection. These tropical maximums become more pronounced above 50km altitude as a result of wind filtering by planetary waves. In the July plots, the most prominent feature is the southern hemisphere momentum flux band around  $50^{\circ}\text{S}$  which is in general in good agreement with the observations from Figure 3.2. Again, single sources like the orography of the southern Andes and the Antarctic Peninsula are not well represented due to the homogeneous launch positions of each simulated wave. Also, the tropical momentum flux is less concentrated in the simulations above the continents compared to the measurements, but smeared out over all longitudes.

From the direct comparison of Figure 3.2 and Figure 3.3 it is possible to conclude that the homogeneous launch distribution for a gravity wave parametrization is able to reproduce the most prominent features seen in the observations. Still, single sources of gravity waves like orography and convection, which yield spatially localized maximums in momentum flux, are not well represented. Therefore, these sources have to be considered for a further improvement of gravity wave parametrizations. Also, the order of magnitude in momentum flux shows deviations somewhat larger than the uncertainty

### 3.5. COMPARISON WITH SATELLITE MEASUREMENTS

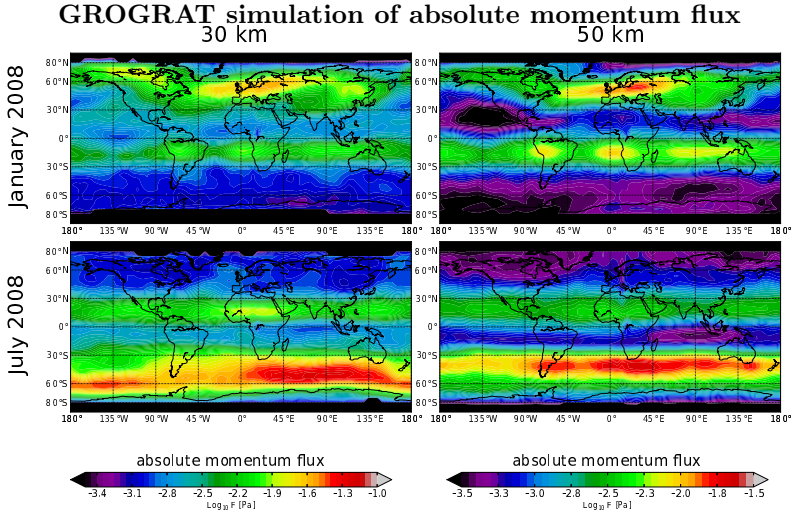


Figure 3.3.: Absolute momentum flux from GROGRAT simulations at 30km and 50km altitude for January and July 2008 (NOGAPS-ALPHA). Prominent features are the higher momentum flux values in the winter hemisphere. Gravity waves in the tropics are present, but not well localised above the continents (compared to Figure 3.2). A different colorscale was used for the 50km altitude data due to lower momentum flux values as a result of wind filtering.

margin of 0.3 and the decline in momentum flux in the simulation from 30km to 50km lower in the simulations (0.5 compared to 1 order of magnitude in SABER data). The reason for this discrepancy in momentum flux can be found in the tuning of non-orographic launch distribution in *Preusse et al.* [2009]. The difference in the momentum flux decline can be explained by the observational con-

strains of the SABER instrument. A problem which will be addressed in chapter 5.3 of this thesis. Today, the majority of general circulation models include a non-orographic gravity wave background parametrization and at least an additional parametrization of orographic gravity waves. Besides first results in the modelling of convective gravity waves, the inclusion into atmospheric models is still a matter of on-going research [*Trinh et al.*, 2014].

# 4. Oblique vs. vertical propagation of gravity waves

## 4.1. Introduction

In general circulation models (GCMs) the influence of gravity wave dissipation on the mean-flow has to be parametrized [e.g. *Kim et al.*, 2003], because most GCMs only resolve a small part of the gravity wave spectrum. A number of different approaches exist to account for gravity waves in global models. These differ in details of the assumed wave spectrum, the realization of gravity wave saturation, and the deposition of gravity wave momentum flux. For instance, some gravity wave parametrizations consider a superposition of individual, independent waves [e.g. *Lindzen*, 1973, 1981, *Alexander and Dunkerton*, 1999], while others explicitly assume a continuous spectrum [*Hines*, 1997, *Warner and McIntyre*, 1999], and some approaches try to compromise [*Medvedev and Klaassen*, 2000, *McLan-dress and Scinocca*, 2005]. These gravity wave parametrizations in-

## CHAPTER 4. OBLIQUE VS. VERTICAL PROPAGATION OF GRAVITY WAVES

---

clude a number of unknown parameters which are “tuned” in such a way that the mean background state of wind and temperatures generated by the GCM matches the observations [e.g. *Manzini and McFarlane*, 1998, *Kim et al.*, 2003, *Eckermann et al.*, 2009, *Orr et al.*, 2010]. Only in a few cases these free parameters have been chosen compliant to observations [*Ern et al.*, 2006, *Orr et al.*, 2010] and there is a large spread between gravity wave momentum fluxes in both different models and for different observations [*Geller et al.*, 2013]. These uncertainties, in conjunction with the fact that tuning can compensate for deficiencies of the parametrizations [*Fritts and Alexander*, 2003], may obfuscate problems, potentially causing major uncertainties in current climate simulations [*Alexander et al.*, 2010b].

The assumption of vertical-only propagation of gravity wave could be such a hidden problem: In order to allow for effective parallelization of GCMs, all parametrizations described above consider the propagation of gravity waves only inside the individual vertical columns of the GCM grid. In practice, this means that gravity waves are not allowed to propagate obliquely. This is in contradiction to gravity wave theory [e.g. *Lighthill*, 1967, *Andrews et al.*, 1987] as well as to observations. Oblique propagation has been observed for individual wave events [*Sato et al.*, 2003] and many observations indicate propagation away from the source [e.g. *Taylor and Hapgood*, 1988, *Preusse et al.*, 2002, *Wu and Eckermann*, 2008]. On a statistical basis, observations indicate that, for instance, gravity waves from convective sources in the subtropics propagate poleward

[*Jiang et al.*, 2004, *Ern et al.*, 2011, 2013] for almost  $20^\circ$  in latitude due to a substantial horizontal group velocity. They thereby evade the wind reversal between tropospheric westerlies and stratospheric easterlies in the summer hemisphere [*Preusse et al.*, 2009]. This has consequences for the representation of the Brewer-Dobson circulation, which in summer is mainly driven by gravity waves [*Alexander and Rosenlof*, 2003].

An additional higher order effect, which is similarly neglected by the only GCM-implemented ray-tracing parametrization [*Song et al.*, 2007], is the momentum transfer to the background flow caused when gravity waves are refracted horizontally. The influence of the horizontal refraction of gravity waves has first been postulated by *Buehler and McIntyre* [2003] and termed “remote recoil”. Its impact on orographic gravity waves has been investigated by *Hasha et al.* [2008]. Some first estimates of the impact for non-orographic gravity waves have been studied in *Preusse et al.* [2009].

In this study we investigate, whether the assumption of vertical-only propagation has larger impacts on the gravity wave drag distribution. In particular, are there changes which cannot easily be compensated for by tuning the source? And does the effect of “remote recoil” have a significant impact on a realistic global distribution?

In order to address these questions, gravity wave drag (GWD) is compared in two different simulations which differ only in the ability of gravity waves to propagate obliquely or not. Effects are considered on a global scale using realistic background winds and a gravity wave launch distribution which is guided by observations.

In section 4.2 we describe the model and its setup, and then present the results for the two model experiments performed in section 4.3. In particular, differences in zonal drag are described in section 4.4, differences in meridional drag are described in section 4.5. In order to explain these differences, we consider propagation of waves in the meridional direction (section 4.6) and how this is caused by wind filtering and Coriolis effects (section 4.7). Further potential effects of oblique gravity wave propagation on the drag are discussed in section 4.8. Finally, we summarize and discuss our findings.

### 4.2. Model setup

The GROGRAT model was used for trajectory and amplitude calculations. GROGRAT solves the ray-tracing equations [Lighthill, 1967] using a semi-implicit 4th order Runge-Kutta solver for trajectory and wave refraction calculations. Trajectories are calculated from the group velocity, which itself is derived from the non-hydrostatic rotational gravity wave dispersion relation (equation 2.5) Background wind, temperature and geopotential height fields are needed as an input for the simulation. These background fields were taken from the NOGAPS-ALPHA (Navy Operational Global Atmospheric Prediction System-Advanced Level Physics and High Altitude) [Eckermann *et al.*, 2009] dataset, with a 6-hourly data coverage from December 2007 to December 2008 on a  $1.5^\circ \times 1.5^\circ$  horizontal grid and an altitude coverage from  $10^3$  hPa (ground level) to  $10^{-4}$  hPa ( $\sim 100$ km) on 68 sigma hybrid levels. NOGAPS-ALPHA

is an extended high altitude dataset version with assimilated Microwave Limb Sounder (MLS) temperature data [Schwartz, 2008] up to 0.002 hPa (corresponding to a geometric altitude of approximately 90km). Thus, realistic background wind and temperature fields up to the mesosphere and lower thermosphere (MLT) region, where gravity wave breaking becomes especially important, can be used.

The launch distribution follows largely that of *Preusse et al.* [2009]. Gravity waves are launched at 5km altitude into 8 azimuth angles and on a regular global grid of  $3^\circ \times 3^\circ$  resolution in the horizontal direction. The launch spectrum is composed of 14 spectral components, each characterized by its initial phase-speed, amplitude, and horizontal wavelength at launch position. The vertical wavelength is calculated using the dispersion relation 2.5. The spectral distribution was obtained by tuning the relative contribution of each single spectral component (called “single spectral component experiment” - SCE - in *Preusse et al.* [2009]) such that zonal mean cross-sections of gravity wave variances match observations of the SABER (Sounding of the Atmosphere using Broadband Emission Radiometry) satellite instrument [Mlynczak, 1997, Russell et al., 1999, Yee et al., 2003, Remsberg et al., 2008]. This leads to 14 intermittency factors serving as weights for the 14 SCEs in averaged quantities like zonal means as described below in this section.

The GROGRAT model offers the opportunity to calculate both, obliquely propagating and purely vertically propagating waves leaving all other properties unchanged. In the absence of dissipation,

## CHAPTER 4. OBLIQUE VS. VERTICAL PROPAGATION OF GRAVITY WAVES

---

gravity wave amplitudes are calculated assuming wave action conservation along the limb ray. The gravity wave drag has been calculated for each individual wave with index  $j$  from the  $i$ -th SCE along its trajectory:

$$(X_{i,j}, Y_{i,j}) = -\frac{\epsilon_i}{\bar{\rho}} \partial_z (F_{px_{i,j}}, F_{py_{i,j}}) \quad (4.1)$$

Here  $X_{i,j}$  and  $Y_{i,j}$  are the zonal and meridional components of the gravity wave drag,  $\bar{\rho}$  is the density of the background atmosphere and  $F_{px_{i,j}}$  and  $F_{py_{i,j}}$  are the zonal and meridional components of the gravity wave momentum flux, respectively. The  $\epsilon_i$  account for the intermittency of the different spectral components. These drag values are evaluated in the same way as the modeled gravity wave temperature variances and gravity wave momentum flux (GWMF) values in *Preusse et al.* [2009]. Values along the trajectories are interpolated onto a 1km vertical grid and are averaged in  $5^\circ$  latitude bins according to

$$(X, Y) = \frac{1}{\sum_{i=1}^{n_{SCE}} n_{z,i}} \sum_{i=1}^{n_{SCE}} \epsilon_i \sum_{j=1}^{n_{z,i}} (X_{i,j}, Y_{i,j}) \quad (4.2)$$

where  $n_{z,i}$  denotes the number of rays of one SCE within the  $i$ -th spatial bin and  $n_{SCE}$  is the number of SCEs used in our simulation. According to *Preusse et al.* [2009] intermittency factors  $\epsilon_i$  for the individual spectral components are normalized to fulfill

$$\sum_{i=1}^{n_{SCE}} \epsilon_i = 1 \quad (4.3)$$

By using a consistent formulation for gravity wave drag, gravity wave temperature variances and GWMF, gravity wave drag values presented here are directly linked to the observations employed in *Preusse et al.* [2009] to determine the values for  $\epsilon_i$ . As discussed below, it is particularly important to distinguish between mid-frequency waves of moderate phase speed, fast waves and waves of very long horizontal wavelengths. *Preusse et al.* [2009] used several educated guesses as well as an automated least squares fit to determine the intermittency factors for the various SCEs by comparing the global distributions from ray-tracing modeling with SABER observations. Though there are variations in detail, they found the same partitioning between these three groups of waves - evidence that the partitioning is robust.

### 4.3. Results

In this section gravity wave drag (GWD) in zonal and meridional direction from two simulations is compared: In the reference run the full three-dimensional gravity wave trajectory calculation of GRO-GRAT was applied and gravity waves were allowed to propagate obliquely. We refer to this case as gravity wave oblique (GWO) and to the resulting drag as GWDO. This GWO case is compared to a simulation of restricted gravity wave vertical-only (GWV) propagation with its drag named accordingly (GWDV). Both simulations for GWO and GWV were performed for January 2008 and July 2008.

Figure 4.1 shows monthly averages of zonal mean GWD (color)

## CHAPTER 4. OBLIQUE VS. VERTICAL PROPAGATION OF GRAVITY WAVES

in the zonal direction for January (a,b) and July (d,e) conditions. Contour lines represent zonally averaged zonal winds. Solid lines indicate eastward winds and dashed lines indicate westward winds. The left column shows drag for the GWO case, the middle column shows drag for the GWV case. Relative differences between GWDV and GWDO are presented in panels c and f.

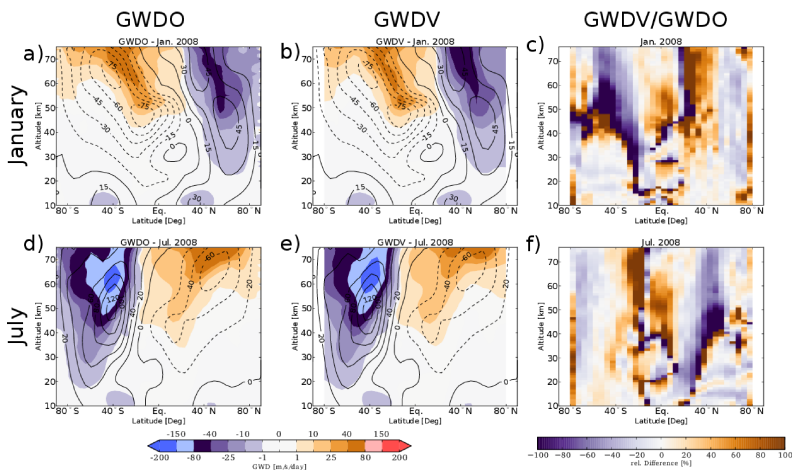


Figure 4.1.: Gravity wave zonal drag (color) and background zonal wind (contour lines) for January 2008 (upper row, panels a-c) and July 2008 (lower row, panels d-f). The left column (panels a,d) shows GWDO, the middle column (panels b,e) GWDV and the right column (panels c,f) relative differences (percentage) of GWDV with respect to GWDO. For discussion of the general features and the differences see text.

The salient patterns of all four acceleration cases are as expected

[Preusse *et al.*, 2006, 2009]. Since drag is shown in  $\text{ms}^{-1}\text{day}^{-1}$ , values generally increase with altitude as density decreases. Values are enhanced at strong vertical gradients of the background winds. For instance, in all cases the values are largest in the region of strongest vertical wind gradients on top of the mesospheric jets (summertime easterlies and wintertime westerlies). This can be explained as follows: gravity waves propagating against the predominant wind direction are Doppler-shifted to high intrinsic phase-speeds in the jets and attain lower intrinsic phase-speeds in the weaker wind velocities on top of the jet. Accordingly, the vertical wavelength is reduced and so is the saturation amplitude, resulting in enhanced wave breaking. In addition, waves which have experienced only westerly (or easterly) winds up to these altitudes may reach a critical layer where the background wind velocity equals the ground-based phase-speed.

For January (panels a,b), both GWDO and GWDV exhibit absolute values of up to  $80\text{ms}^{-1}\text{day}^{-1}$  close to the mesospheric jets. In the winter hemisphere GWD is higher than in the summer hemisphere. This situation is even more pronounced in July, where drag values in the winter hemisphere exceed  $150\text{ms}^{-1}\text{day}^{-1}$  but reach only  $\sim 80\text{ms}^{-1}\text{day}^{-1}$  in the summer hemisphere. Such lower drag values for the summer hemisphere are also indicated by satellite estimates of GWD based on absolute momentum flux values by *Ern et al.* [2011]. Due to favorable propagation conditions momentum flux values in the winter hemisphere are larger. This is a general feature independent of the individual launch spectrum or GWD parametrization, as indicated by the comparison of gravity wave mo-

## CHAPTER 4. OBLIQUE VS. VERTICAL PROPAGATION OF GRAVITY WAVES

---

mentum in five middle atmosphere general circulation models [Geller *et al.*, 2013]. When deposited in the MLT (mesosphere and lower thermosphere region), these larger gravity wave momentum fluxes result in the larger GWD values seen in figure 4.1.

The modeling results in Figure 4.1 show much higher maximum GWD values for southern hemisphere winter than for northern hemisphere winter conditions. This is not the case for the observed drag at these altitudes [Ern *et al.*, 2011], but observed stratospheric gravity wave momentum flux values show a similar hemispheric asymmetry with much higher values for southern winter [Ern *et al.*, 2011, Geller *et al.*, 2013]. Results from several GCMs also shown by Geller *et al.* [2013] indicate quite similar absolute stratospheric gravity wave momentum flux for the respective winter hemisphere. These GCM values contain both orographic and non-orographic GWs.

The launch distribution used in our study is tuned to match SABER gravity wave variances for July and CRISTA (Cryogenic Infrared Spectrometers and Telescopes for the Atmosphere) [Offermann *et al.*, 1999, Riese *et al.*, 1997, 1999] gravity wave momentum flux values for August. Because of the relatively sparse topography in the southern hemisphere, the contribution of mountain waves to the measured distributions in these months is relatively low. As discussed by Preusse *et al.* [2009], a launch distribution tuned for January conditions would contain a higher amount of slow phase-speed waves, i.e. presumably mountain waves. The use of the same globally homogeneous source distribution for January and July may hence explain why hemispheric asymmetries are stronger in our model re-

sults than in the measurements: weaker gravity wave momentum flux due to stronger wind filtering in a pronounced planetary wave structure in the northern hemisphere are largely compensated by more orographic sources.

Furthermore, absolute peak values of GWD in Figure 4.1 are larger than the corresponding values in the observations [*Ern et al.*, 2011]. One potential reason is that CRISTA gravity wave momentum flux of *Ern et al.* [2004], *Preusse et al.* [2009, 2002] is corrected for some visibility effects and therefore larger than SABER values which were not corrected. Another reason could be that drag is exerted at different altitudes and latitudes due to details of the wind fields.

Figure 4.2 shows altitude profiles of zonal GWD for January 2008 (a) and July 2008 (b). Given are the absolute values of latitude-averaged GWD on a logarithmic scale. Changes from positive to negative drag or vice-versa are therefore indicated by sharp peaks of very low absolute values. The solid lines represent GWDO, dashed lines represent GWDV, and color denotes the different latitude region used for averaging: northern hemisphere (20°N-70°N - red), southern hemisphere (20°S-70°S - blue) and the tropical region (20°N-20°S - black).

For the winter hemisphere (January: NH, red and July: SH, blue), drag is always in the same direction (westward) and agrees well in both simulations except for some small deviations above 60km altitude. Gravity wave drag values in SH winter are much larger than values in NH winter also for the hemispheric integral. In the tropical stratosphere several poles in the logarithm are found, i.e. zero cross-

ings in the drag, which are due to the QBO wind reversals. In the lower stratosphere GWDO and GWDV agree well, where at higher altitudes, in particular around the stratopause (50km), GWDV exceeds GWDO. In the summer hemisphere (January: SH, blue and July: NH, red) a sharp low-value peak indicates the reversal from low-altitude westward drag to high-altitude eastward drag. GWDV is larger below this reversal and smaller above this reversal than GWDO, i.e. GWDO is more eastward directed at all altitudes. This shifts the altitude of the zero crossing to lower altitudes (37km for GWDO instead of 41km for GWDV in January and 31km instead of 34km in July). Also note that the zero crossings in GWDV are sharp, indicating that the reversal of drag is at about the same altitude for all latitudes averaged, while the smoother peak of GWDO indicates a drag reversal at slightly different altitudes for different latitudes. This differences will be discussed in the next section.

#### **4.4. Differences between oblique and vertical propagation**

Relative differences between GWDO and GWDV are shown in Figures 4.1c and 4.1f. Largest differences are found in the upper stratosphere / lower mesosphere region of the summer hemisphere (southern hemisphere in January, northern hemisphere in July), where GWDO is larger at the lower side of the easterly jets slightly above the wind reversal. In the winter hemisphere there is a pattern of en-

#### 4.4. DIFFERENCES BETWEEN OBLIQUE AND VERTICAL PROPAGATION

hanced GWDV at low latitudes ( $20^\circ$  to  $40^\circ$ ) and enhanced GWDO at higher latitudes ( $40^\circ$  to  $70^\circ$ ). Still, the profiles averaged over the entire winter hemisphere ( $20^\circ$  to  $70^\circ$ ) in Figure 4.2 show good agreement between GWDV and GWDO. The red/blue pattern in the upper stratosphere and mesosphere in Figure 4.1c,f hence indicates a poleward shift of the drag maximum in the winter jet for the GWO case, which does, however, not alter the total drag in this region. In the equatorial region, GWDV is generally higher as seen also in Figure 4.2.

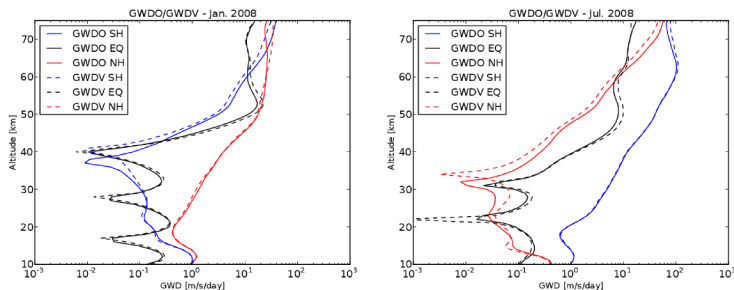


Figure 4.2.: Altitude profiles of GWD for different regions during January 2008 (a) and July 2008 (b). Solid lines indicate GWDO, dashed lines indicate GWDV. Profiles are averaged over  $70^\circ\text{S} - 20^\circ\text{S}$  (southern hemisphere - blue),  $20^\circ\text{S} - 20^\circ\text{N}$  (equatorial region - black) and  $20^\circ\text{N} - 70^\circ\text{N}$  (northern hemisphere - red).

There are also some local differences, which are less obvious, but could also be important, e.g. for chemistry climate simulations. In the regions of the subtropical jets, wind filtering in the UTLS regions of the summer hemisphere is particularly strong. This results

## CHAPTER 4. OBLIQUE VS. VERTICAL PROPAGATION OF GRAVITY WAVES

---

in local minima around  $50^\circ$  latitude at 70km altitude in GWDV. At the same places, GWDO smoothly follows the contours of the horizontal winds. This indicates that oblique propagation can redistribute GWMF across latitudes. For our study based on a homogeneous start distribution, this acts to smooth out patterns by wind filtering, but in general could also redistribute GWMF from specific sources.

Summarizing the most prominent patterns discussed above, three main differences between GWDO and GWDV are found: enhanced GWDO at the lower-altitude side of the summer jet, the poleward shift of drag for the winter jet and reduced equatorial drag in the GWO case. What causes this differences?

For this study a launch altitude of 5km has been chosen in accordance with previous studies of e.g. *Manzini and McFarlane* [1998] or *Ern et al.* [2006]: the main features of the middle atmosphere gravity wave momentum flux distribution are generated by wind filtering in the upper troposphere and lowermost stratosphere (UTLS). However, close to the source, it is expected that the filtering affects the GWO case and the GWV case in a very similar manner. This is confirmed by values close to zero in Figure 4.1c and 4.1f. Note that these small values rise to large relative differences: even though the absolute drag values remain low in the UTLS, relative differences would indicate, if the filtering was largely different. Since the distribution at UTLS heights is similar, only the different propagation above the UTLS can cause the larger differences observed around the stratopause and in the mesosphere.

Gravity waves find favorable propagation conditions if the wind direction is the same in the troposphere and middle atmosphere, but are mostly filtered if the wind direction reverses between troposphere and middle atmosphere. In particular, gravity waves with low ground-based phase-speeds will be strongly affected by such filtering. This explains, for instance, very low gravity wave momentum flux values in the lower stratosphere at summer mid-latitudes [Ern *et al.*, 2006, Preusse *et al.*, 2009]. In the summer subtropics, however, winds are easterly in both, the troposphere and the stratosphere. If some of these waves propagate poleward, they can reach mid-latitudes, dissipate and cause the enhanced GWDO at the low-altitude part of the summer jet. Horizontal propagation of gravity waves in the GWO case can also explain the poleward shift of the winter hemisphere maximum in GWD. These waves, which propagated poleward, are now missing in the equatorial region and GWDO is therefore smaller at low latitudes. Thus, poleward propagation of waves would account for all three major patterns in the differences between GWDO and GWDV.

## 4.5. Meridional drag

So far, only zonal GWD has been considered, but the effects for meridional GWD shown in Figure 4.3 are even more pronounced. First, meridional GWDO (panels a, c) is much higher than GWDV (panels b, d). Gravity wave drag values can be as high as  $150\text{ms}^{-1}\text{day}^{-1}$  compared to only  $10\text{ms}^{-1}\text{day}^{-1}$  for GWDV above the mesospheric

## CHAPTER 4. OBLIQUE VS. VERTICAL PROPAGATION OF GRAVITY WAVES

---

jet for July conditions. Second, the altitude-latitude structure is different: meridional GWDO is high in those regions where zonal GWD in Figure 4.1 is also high. Similarly to zonal drag, meridional GWDO closely follows the zonal winds indicated by the contour lines in the left column. In addition, SH winter values of meridional GWDO are much larger than NH winter values, again similar to zonal drag. In contrast, GWDV is found mainly at the highest altitudes and of similar values for January and July. Finally, GWDO is generally directed towards the pole of the respective hemisphere, thus showing a hemispheric split, both for January and July conditions. The prevailing meridional GWDV is directed northward (positive values) in July and southward (negative values) in January, i.e. opposed to the expected direction of the global scale circulation indicated by the meridional mean winds shown in the right column of Figure 4.3.

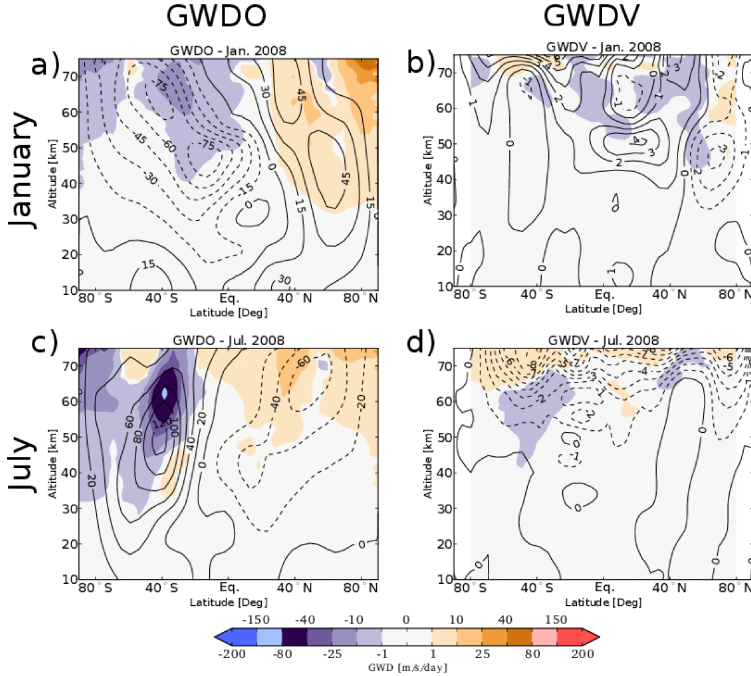


Figure 4.3.: Gravity wave meridional drag (color) for January 2008 (upper row) and July 2008 (lower row). For meridional GWDO (left column) contour lines show the zonal wind, for meridional GWDV (right column) contour lines show the meridional wind.

Further investigation showed that the hemispheric split in GWDO is present throughout the entire year and meridional drag is generally poleward directed, independently from the seasonal cycle. However, the precise latitude where meridional GWDO changes sign

from southward to northward shifts between the two seasons, from northern hemisphere latitudes in January to southern hemisphere latitudes in July (altitude 55km upwards). Like in *Preusse et al.* [2009], the high altitude GWD peaks close to the poles are assumed to be an artifact due to GROGRAT lacking the cross-pole propagation ability. Neglecting these peaks, the meridional GWD in the GWDO case is still much stronger and generally directed in poleward direction.

## 4.6. Poleward propagation

In section 4.4 it has been argued that a prevalence of poleward propagating gravity waves in the GWDO case could explain the differences between GWDO and GWDV for zonal drag. Likewise, a prevalence of poleward propagating gravity waves would explain the patterns of meridional drag in the GWDO case. In general, the zonal background wind is much stronger than the meridional wind. Waves which are launched at angles  $45^\circ$  from the cardinal directions, i.e. those which are launched with both a zonal and a meridional wave component, are therefore primarily modulated by the zonal wind in a similar way as waves launched in the zonal direction. In the GWDV case, waves propagating e.g. to the northwest and to the southwest are kept together at the same location in latitude and longitude while they are propagating upward. They are therefore modulated by the same zonal winds and the meridional net effect cancels. Only modulation induced by the much weaker meridional

## 4.6. POLEWARD PROPAGATION

---

winds causes a net drag. This net drag is expected to act opposite to the meridional prevailing winds as indicated for the GWDV case in section 4.5. If e.g. northwest and southwest components are allowed to separate spatially, they are modulated by different zonal winds at different locations. This causes an additional net meridional drag at similar locations like the zonal drag, to which these waves also contribute. This additional meridional drag is much stronger than the meridional drag induced by meridional winds only. In regions with prevalent poleward propagation (i.e. most of the higher latitudes), this drag pattern is therefore preferentially poleward directed.

This immediately leads us to the question: Is there any evidence for poleward propagation? In a ray-tracer, single waves can be monitored. That supports the means to answer this question. Figure 4.4 shows the number distribution of absolute end-latitude (y-axis) vs. launch-latitude (x-axis) of all gravity waves for two representative days of January and July 2008. Poleward propagating waves dissipate at higher latitudes compared to their launch latitude, thus they are found above the dashed black diagonal. Equatorward propagating waves fall below this diagonal.

The equatorial region seems to be generally dominant even at 20km altitude because a larger number of high- and mid-latitude waves have already been filtered out at this altitude. Also, waves originating from  $0^\circ$  to  $5^\circ$  have frequently already propagated  $30^\circ$  poleward at 20km altitude, as can be seen from Figure 4.4a. At 60km altitude (Figure 4.4b, the majority of waves is found above the diagonal. For waves originating in the tropics, the maximum of

## CHAPTER 4. OBLIQUE VS. VERTICAL PROPAGATION OF GRAVITY WAVES

---

the number distribution indicates  $\sim 25^\circ$  poleward propagation and even waves originating from  $60^\circ$  are found on average  $10^\circ$  further poleward. For July (Figure 4.4c-d) equatorward propagation (indicated by the secondary diagonal with lower end-latitudes than start-latitudes below the black line) can be also found, but the poleward direction still remains stronger.

## 4.6. POLEWARD PROPAGATION

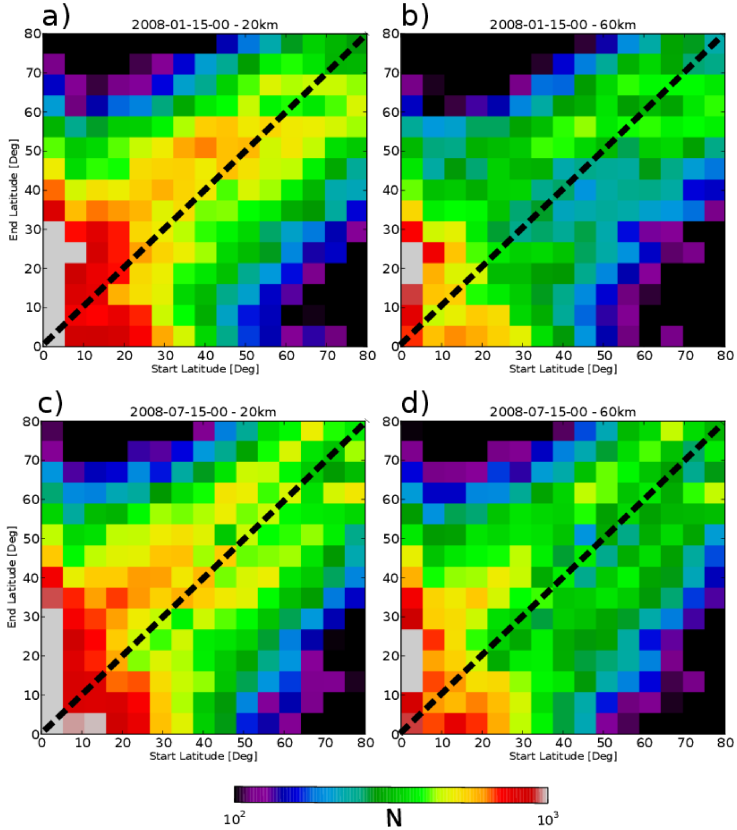


Figure 4.4.: Number distribution of absolute start vs. end latitude of each wave for a representative January (a-b) and July (c-d) snapshot at altitudes of 20km and 60km. Wave events above the diagonal indicate poleward propagation, events below the diagonal equatorward propagation. Color indicates the number of events in a respective bin on a logarithmic scale.

## 4.7. Influence of wind filtering and the Coriolis effect

Since there is evidence for poleward propagation, another question for the reason for the prevalence of poleward propagation can be addressed now: What causes this prevalence of poleward propagating gravity waves? There are two potential mechanisms, which are first introduced and then investigated by ray-tracing experiments.

According to the dispersion relation (equation 2.5) a propagating gravity wave can only exist if the intrinsic wave frequency  $\hat{\omega}$  is greater than the Coriolis parameter  $f$ . At moderate phase-speeds, in particular gravity waves with very long horizontal wavelengths (short vertical wavelengths) are therefore restricted to the equatorial region. This is the reason why climatologies for squared amplitudes or potential energy of long horizontal wavelength (and short vertical wavelength) gravity waves exhibit an equatorial maximum at low altitudes [*Alexander et al.*, 2002]. Note that this maximum is overestimated in these early publications, since Kelvin waves are often not removed or underestimated. However, even after removing Kelvin waves properly, gravity wave momentum flux remains slightly enhanced in the tropics compared to winter mid-latitudes, especially for the lower stratosphere and long horizontal wavelengths (short vertical wavelengths). Therefore, SCEs consisting of long horizontal wavelengths contribute to the global distribution at low altitudes only in the tropics. Gravity waves of long horizontal wavelengths are one reason why so many more waves at low latitudes are observed in

#### 4.7. INFLUENCE OF WIND FILTERING AND THE CORIOLIS EFFECT

---

Figure 4.4. They have low vertical group velocities and propagate very obliquely. Therefore, they have the potential to reach higher latitudes even at low altitudes, if they can exist at these higher latitudes. This is the case where they are propagating opposite to fast background winds: the intrinsic frequency is Doppler-shifted such that waves can escape the tropical confinement [Preusse *et al.*, 2009]. To be distinguished from a second effect discussed below, this will be called the global Coriolis mechanism.

The second potential reason to consider is wind filtering. As described above, many gravity waves are removed already in the UTLS region. In particular, the wind reversal at the summer tropopause is permeable only to gravity waves of high ground-based phase-speeds. Similar as for the global Coriolis mechanism, more waves exist in the lower stratosphere in the tropics than at higher latitudes, and in particular at higher summer latitudes. Finally, waves can be refracted by horizontal wind gradients. This may exert drag at the location of refraction, but it will also focus gravity waves into the wind jets and thus shift the location of gravity wave momentum flux deposition.

In order to investigate the relative importance of wind filtering and Coriolis filtering, further ray-tracing calculations using the COSPAR international reference atmosphere (CIRA) have been performed. Differences between GWDV and GWDO (not shown) exhibit the same main three features of enhanced eastward GWDO in the summer stratosphere, poleward shift of the maximum GWDO in the winter polar vortex and lower GWDO in tropical upper stratosphere

## CHAPTER 4. OBLIQUE VS. VERTICAL PROPAGATION OF GRAVITY WAVES

---

and mesosphere. Therefore, climatological data can be used to investigate the cause of these patterns with a smaller number of rays launched. In two experiments, effects of wind filtering and the global Coriolis mechanism were isolated, respectively.

In Figure 4.5 a standard GWO run (left column) is compared to a simulation where a constant Coriolis factor  $f = \Omega \sin 30^\circ$  was applied everywhere, independent of the position of the ray (middle column). Since the two simulations are otherwise exactly the same, the differences in the right column reveal the effect of the global-Coriolis mechanism alone. The “fixed- $f$  simulation” suppresses very long horizontal wavelengths at the equator and in particular removes the part of the tropical maximum in ray number which is due to the global-Coriolis mechanism. This is expressed in lower drag in the tropical UTLS and tropical lower stratosphere region. Larger differences are also found for the summer-stratopause. There the differences are of about the same size as the differences between GWDO and GWDV presented in Figure 4.1. Differences in the mesosphere of the winter hemisphere are, however, small and have the opposite sign to the GWDO-GWDV differences presented in Figure 4.1. This means that the global-Coriolis mechanism does contribute little to the poleward shift of the winter drag maximum in the mesosphere.

For the meridional drag the general patterns are very similar in the standard GWDO simulation and the simulation with constant Coriolis parameter. Considering the difference plots, however, the absolute values of the latter are only about 50% of the standard

#### 4.7. INFLUENCE OF WIND FILTERING AND THE CORIOLIS EFFECT

---

run. In summary, the global Coriolis effect is responsible for the enhanced zonal GWDO around the summer stratopause and for about half the meridional drag. The first sensitivity experiment investigates the impact of the Coriolis force as a shaping factor for the global distributions. Results for this experiment are shown in Figure 4.5. The second sensitivity experiment shown in Figure 4.6 neglects the latitudinal variation of the wind field. As a result, the Coriolis force and geometry remain as the only factor generating latitudinal differences. The left column of Figure 4.6 again shows a standard GWO run and the middle column shows results for a CIRA wind profile taken from  $40^{\circ}\text{S}$  with the standard calculation of the Coriolis factor along the waves. In this way, a summer mid-latitude (January) and a winter mid-latitude (July) wind profile was applied globally. In a vertical-only simulation, the results of this experiment would be different for every latitude but remain unchanged for  $40^{\circ}\text{S}$ . The latitude of  $40^{\circ}\text{S}$  is also chosen because it is the position of the subtropical jet. In January, the wind reversal globally removes a large part of the gravity wave spectrum already at UTLS altitudes.

## CHAPTER 4. OBLIQUE VS. VERTICAL PROPAGATION OF GRAVITY WAVES

---

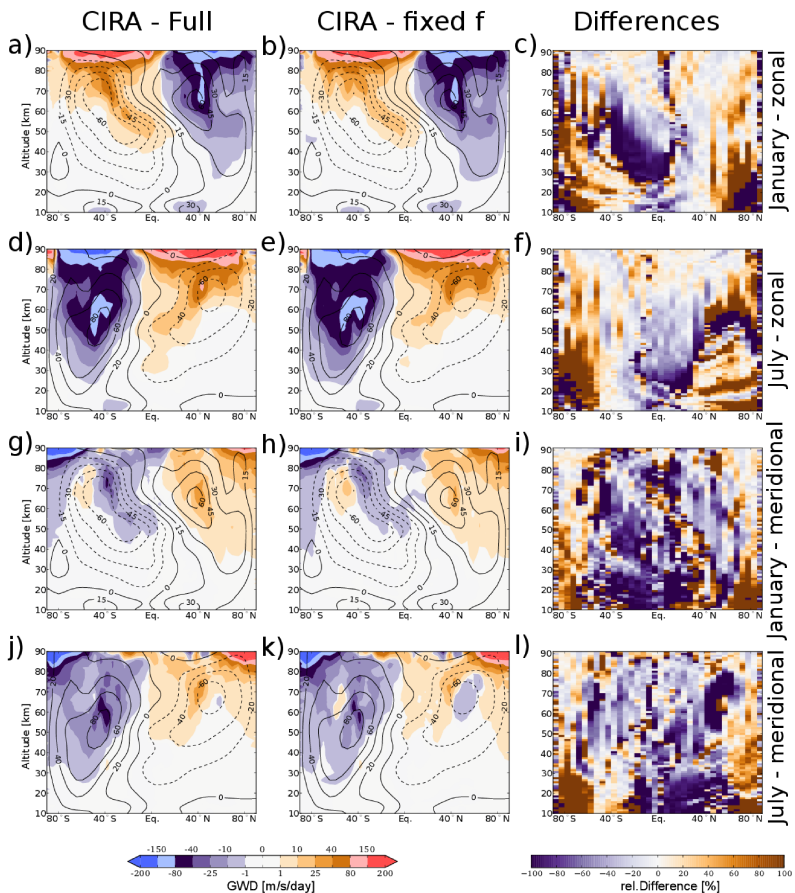


Figure 4.5.: Sensitivity run on the influence of the Coriolis parameter based on CIRA background winds. Gravity wave zonal drag (color) and background zonal wind (contour lines) for a standard GWO simulation (left column) and a simulation using a fixed Coriolis factor  $f$  for  $30^\circ$  latitude (middle column). Relative differences between both runs are depicted in the right column. The upper rows is for January (zonal, meridional) and the lower rows for July (zonal, meridional).

#### 4.7. INFLUENCE OF WIND FILTERING AND THE CORIOLIS EFFECT

---

Accordingly, there is about  $-1\text{ms}^{-1}\text{day}^{-1}$  drag around 15km for all latitudes. Though this drag value is small, quite a large fraction of gravity wave momentum flux is dissipated. Comparing this run to the standard GWDO run, the effects of wind filtering can be isolated. At low latitudes, drag is enhanced compared to the reference GWDO below 30km in panel c and below 25km in panel f, and much smaller above these altitudes. In panel c, the area of reduced drag spreads poleward from low latitudes and reaches  $40^\circ$  S at approx. 50km altitude. Only above 75km altitude, zonal GWD is approx. the same as in the standard run. Considering the summer hemisphere, i.e. the January values, two main findings can be obtained: Firstly, due to wind filtering, low latitudes are more permeable for low phase-speed waves than summer mid-latitudes. At summer mid-latitudes, the effect for the zonal drag is of about the same size as the Coriolis effect. Secondly, while the Coriolis effect mainly affects very long horizontal wavelengths, wind filtering acts on the phase-speed and also removes shorter horizontal wavelengths. The latter propagate less obliquely than the very long horizontal wavelengths and affect higher altitudes.

In July, there is no wind reversal and propagation conditions in the lower atmosphere are obviously very favorable for  $40^\circ$  S resulting in maximum mesospheric drag between  $35^\circ$  S and  $50^\circ$  S in the standard run (Figure 4.6d). If these favorable propagation conditions apply for the entire southern hemisphere, this results in enhanced drag in the mid-mesosphere also for  $40^\circ$  S (positive values in panel f for altitudes larger 60km). This is some indication for the reason of

## CHAPTER 4. OBLIQUE VS. VERTICAL PROPAGATION OF GRAVITY WAVES

---

the poleward shift of the winter maximum: at latitudes higher than  $40^\circ$  S, the permeability of the atmosphere for gravity waves is lower, so some waves from around  $40^\circ$  S will spread to these higher latitudes when propagating to higher altitudes and generate larger drag there. (Please do not consider values north of  $\sim 20^\circ$  S, they are too different for comparison and indicate only the relative sign of the two simulations, i.e. the drag reversal on the summer hemisphere discussed for Figures 4.1 and 4.2.)

## 4.7. INFLUENCE OF WIND FILTERING AND THE CORIOLIS EFFECT

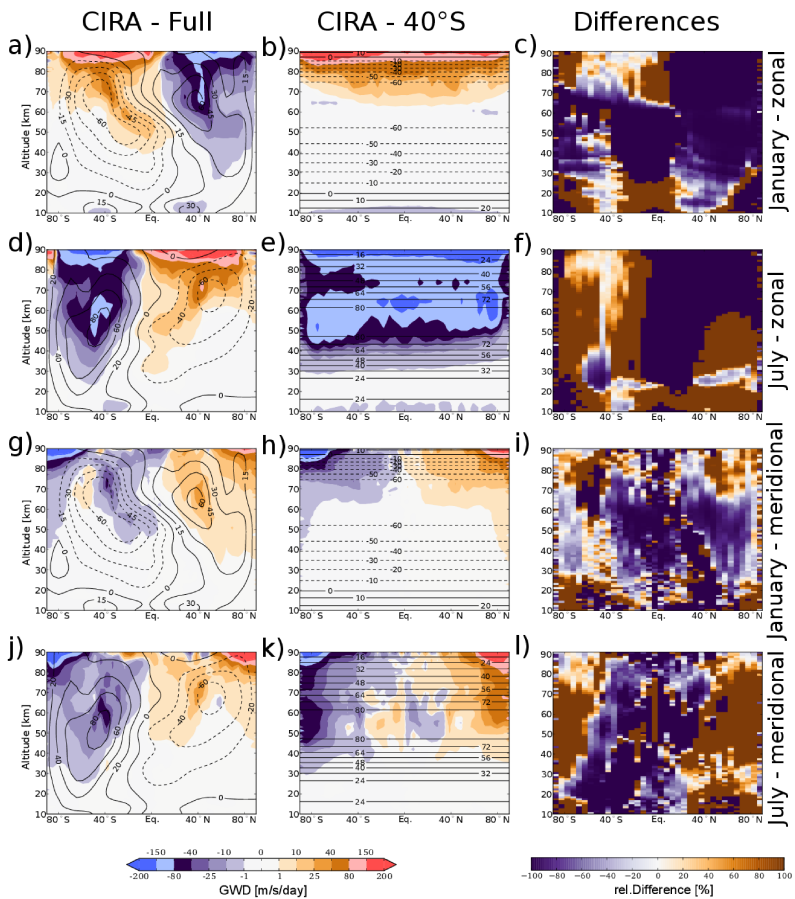


Figure 4.6.: Depiction according to Figure 4.5 but for a sensitivity run applying the CIRA wind profile for 40°S for all latitudes and non-constant Coriolis factor. Thus, latitudinal variations are only induced by Coriolis force and spherical geometry.

The pattern of reduced drag at high winter latitudes and enhanced drag at low winter latitudes observed in the GWDV/GWDO differences depicted in Figure 4.1 cannot be reproduced by using a single wind profile. Apparently, the wind filtering of gravity waves is more complex than the Coriolis effect.

In addition, focussing of waves into the jets contributes. The latitudinal patterns of meridional drag largely differ from those of the reference run. For instance, spurious meridional drag at the boundaries is much larger. Obviously, the wind gradients of the jets are required to induce meridional gravity wave drag at the same locations where zonal gravity wave drag would also be maximal in the standard runs. Still, there is a hemispheric split generated by the global-Coriolis mechanism. Considering the July case for  $40^\circ$  S, there is a maximum around 60km altitude at about the same location where the reference GWDO run also peaks. This maximum is, however, only half as large as in the reference run.

### **4.8. Further potential mechanisms: local Coriolis and remote recoil effect**

In section 4.7, two major effects have been considered which are both equally important for roughly 50% of the observed preference in poleward propagation and the resulting zonal and meridional drag patterns. These sensitivity studies suggest that the two major mechanisms have been identified here, but, considering the range of un-

#### 4.8. FURTHER POTENTIAL MECHANISMS: LOCAL CORIOLIS AND REMOTE RECOIL EFFECT

---

certainty, this does not rule out the contribution of other effects. It should therefore be investigated whether two further conceivable mechanisms may contribute.

An additional possible reason for the high poleward meridional GWD is the potentially higher dissipation of poleward propagating waves compared to equatorward propagating waves due to the Coriolis factor  $f$ . This can be deduced from the dispersion relation (equation 2.5) as follows: assuming horizontal wavelengths to be much larger than vertical wavelengths, it is obtained that  $k^2 + l^2 = k_h^2 \ll m^2$ . Now, (equation 2.5) can be represented in the simpler form:

$$\hat{\omega}^2 = \frac{N^2 k_h^2}{m^2} + f^2 \iff m^2 = \frac{N^2 k_h^2}{\hat{\omega}^2 - f^2} \quad (4.4)$$

Comparable to the situation close to a critical wind shear,  $m$  grows towards infinity for  $\hat{\omega}^2$  approaching  $f^2$ . Thus, the vertical wavelength of the waves gets shorter and wave dissipation increases. For waves launched close to the equator,  $f^2$  is almost zero and grows proportional to  $\sin^2 \phi$  (where  $\phi$  is the latitude) towards the poles and  $m^2$  finally diverges, i.e. the vertical wavelength approaches zero and the wave dissipates. Theoretically, the dissipation of gravity waves is increased on average for poleward traveling waves and this could generate an asymmetry in drag, even if there would be an equal amount of poleward and equatorward propagating waves. Since this asymmetry is introduced locally as the waves propagate further poleward/equatorward, this mechanism is termed the local-Coriolis mechanism in contrast to the global-Coriolis mechanism affecting

the whole global shape of the gravity wave momentum flux and drag pattern.

This hypothesis has been tested by using the launch value of the Coriolis parameter along the whole ray-path. This means that the global-Coriolis mechanism takes full effect, since long horizontal wavelength gravity waves can be launched only at low latitudes, but the local-Coriolis effect is eliminated, since  $f$  does not change along the ray-path and accordingly  $m$  is not modified due to changing values of  $f$ . This simulation (not shown) does not result in significant changes compared to the reference run.

“Remote recoil” was considered in *Preusse et al.* [2009]. It is not very important for the zonal drag, but alters the meridional drag pattern and shifts the altitude of the meridional drag maximum. This does not mean that horizontal refraction is unimportant, since this causes the focusing into the wind jets.

### 4.9. Summary and Discussion

Gravity wave parametrizations make the strong assumption of vertically propagating gravity waves which is, as already discussed by *Lindzen* [1981], a major simplification. The GROGRAT ray-tracer [*Marks and Eckermann*, 1995] was used in two different modes to quantify the influence of this simplification for realistic global gravity wave drag distributions based on the launch distribution inferred in *Preusse et al.* [2009] and background winds from NOGAPS-ALPHA. In the GWO cases three-dimensional propagation of gravity waves

was applied to calculate the gravity wave drag distributions. For the GWV simulations, the propagation of gravity waves was restricted to the vertical direction. The differences between these two simulations are due to the this assumption only and avoid additional effects such as different spectra or wave physics included in previous studies (e.g. *Watanabe* [2008]).

The restriction to vertical propagation alters the global distributions of both the zonal drag and the meridional drag. For zonal drag the following major patterns were found: GWDO is enhanced in the summer stratopause and mesosphere region, drag is reduced in the tropics above the mid stratosphere (30-40km), and in the GWO case the drag maximum at the top of the winter polar jet is shifted poleward. In addition, some local structures caused by local wind filtering in the UTLS are smoothed. The influence on meridional drag is much stronger and alters the distribution completely: in the GWV case, drag is opposed to the summer pole to winter pole circulation in the upper mesosphere and relatively weak. In the GWO case, drag is exerted at similar locations where zonal drag is also large, and the absolute values are much larger. The direction of the drag is from low-latitude to pole.

These differences are caused by several mechanisms further investigated in this thesis. Gravity waves are generated to a large extent in the troposphere. This is reflected here by using a launch altitude of 5km. Wind filtering in the UTLS region and the Coriolis effect shape the general structure of GWMF in the middle atmosphere [*Manzini and McFarlane*, 1998, *Ern et al.*, 2006]. On top of

## CHAPTER 4. OBLIQUE VS. VERTICAL PROPAGATION OF GRAVITY WAVES

---

the UTLS ( $\sim 25$ km), GWDV and GWDO are still similar, but from here on GWs can propagate along different paths in the GWO case. The main mechanisms are summarized in Figure 4.7.

Different scales of gravity waves are indicated in Figure 4.7 by different colors. Green indicates mid-frequency gravity waves of moderate horizontal wavelengths (500km in our simulations) and low to moderate ground-based phase-speeds. They dominate the GWD in the middle atmosphere. These waves are filtered at wind reversals, explaining the low GWMF in the summer stratosphere seen by many observations [Ern *et al.*, 2014, Sato *et al.*, 2003]. At low latitudes and in the winter hemisphere these waves find favorable propagation conditions and they are horizontally refracted into the jets (cf. also Preusse *et al.* [2009]). Because there is a preference of poleward propagation this causes the poleward shift of the drag maximum on top of the winter polar jet and enhanced GWDO in the summer mesosphere. Local filtering structures in GWDV are washed out in GWDO. Red indicates gravity waves of very long horizontal wavelengths. These waves can exist at low altitudes only at low latitudes, but can escape the confinement by the Coriolis parameter at higher altitudes when they are Doppler shifted to higher intrinsic phase-speeds. Because of their very long horizontal wavelengths they propagate very obliquely. They shift the drag reversal from westward to eastward drag in the summer hemisphere to lower altitudes and generally fill the gap of GWD in the summer stratopause region, i.e. at lower altitudes than the mid-frequency waves indicated in green.

At the highest altitudes very fast gravity waves become dominant (blue). This was also shown by *Preusse et al.* [2009], who found that only these fast waves can explain the observed reversal from winter to summer maximum at high latitudes around the mesopause. These waves are only weakly influenced by the wind filtering below and they propagate only low distances in the horizontal. This will reduce GWDV/GWDO differences in the MLT region as seen in CIRA and TIME-GCM runs (not shown) extending to higher altitudes than the NOGAPS data.

Since regions favorable for gravity wave propagation in the UTLS are found more frequently at low latitudes, and because of the influence of the Coriolis parameter, there is a general prevalence of gravity waves propagating from low to high latitudes (see Figure 4.4). Many of these waves have a zonal as well as a meridional component and are therefore modulated by the background zonal winds, which are (not only in the zonal average) much stronger than the meridional wind. Therefore, meridional drag patterns are found at the same location as zonal drag maxima and are poleward directed. This effect cannot be found in a GWV simulation because there, the modulation due to the zonal wind will always act the same way on the waves with northward or with southward component, leaving no net effect. In other words, the pattern is caused by the spatial separation of these waves.

General circulation models can explain main features of the middle atmosphere and the MLT region. It is therefore not surprising that the zonal drag differences between GWO and GWV are moderate,

## CHAPTER 4. OBLIQUE VS. VERTICAL PROPAGATION OF GRAVITY WAVES

---

since the vertical-only assumption for gravity wave propagation is commonly applied in GCMs. Some of these differences may be even further reduced by tuning of the assumed gravity wave spectrum. However, such apparently smaller differences could become important for a detailed understanding, e.g. downward coupling for which gravity wave drag is a major source of uncertainty [*Sigmond and Scinocca, 2010*]. Distributions of trace species may be affected as, for instance, gravity waves are the main driver of the summer-time Brewer-Dobson circulation [*Alexander and Rosenlof, 2003*]. In this region, GWDO is enhanced with respect to GWDV. Perhaps even more importantly than the mere value, the propagation path is different, which may lead to different feed-backs to climate change. In addition, the momentum deposited in the GWO simulation is better aligned with the mesospheric wind gradients - a feature in good qualitative agreement with observational studies *Ern et al. [2011]*. This could be important for the onset of jet instabilities and therefore influence the quasi-two-day waves *Ern et al. [2013]*.

The influence of the meridional acceleration on the general circulation can only be estimated by GCM simulations. This is beyond the scope of this thesis. However, as a first order effect, the meridional drag and zonal drag occur at the same position. Therefore, an easy-to-implement test to GCM modellers is proposed: the meridional drag can be kept proportional to the absolute zonal drag, scaled, and adjusted for hemisphere:

$$Y_N = Y + \alpha \cdot \Gamma \cdot |X| \tag{4.5}$$

with  $X$  representing the zonal drag component calculated by a common gravity wave parametrization,  $Y$  the meridional drag component,  $\alpha$  as a positive scaling factor and  $\Gamma$  as a hemispheric function ( $\Gamma = -1$  for SH;  $\Gamma = 1$  for NH). The latter ensures the poleward direction of the new adjusted meridional drag  $Y_N$ . The scaling factor  $\alpha$  should be zero at the tropopause, high (e.g. 50%) in the mid-stratosphere and mesosphere, and vanish again at the mesopause. This meridional acceleration may directly affect the residual circulation, but also changes the interaction of gravity waves and planetary waves. Thus, a first assessment of some of the effects of oblique wave propagation can be considered without actually including a ray-tracing parametrization into a GCM. However, the overall conservation of momentum and energy have to be carefully considered.

## CHAPTER 4. OBLIQUE VS. VERTICAL PROPAGATION OF GRAVITY WAVES

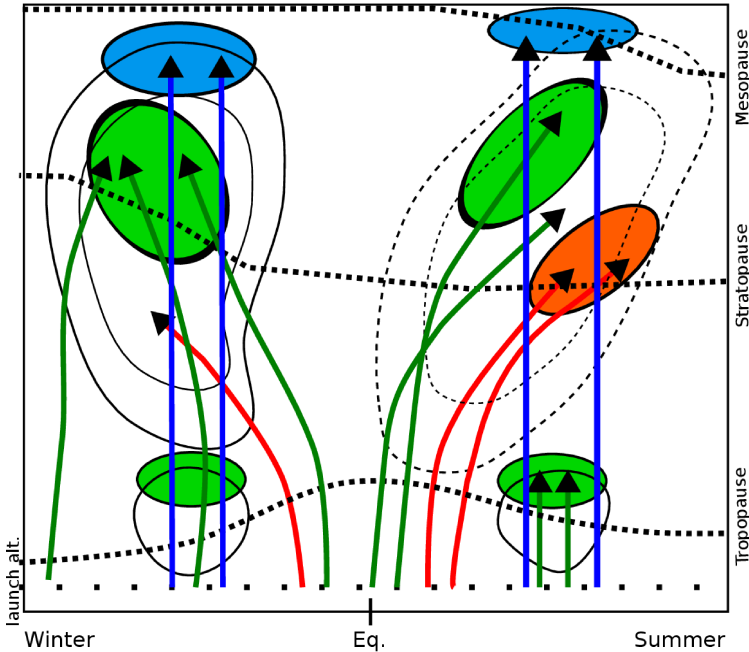


Figure 4.7.: Schematic view for different scales of gravity waves of their propagation and interaction with the background flow. A typical solstice wind field is indicated by thin black lines, the separation into the main compartments troposphere, stratosphere and mesosphere is indicated by bold dashed black lines. Gravity waves are indicated by colored arrows, the main regions where they exert drag are indicated by the color-shaded regions. Note that drag is exerted, in general, all along the propagation paths. Gravity waves of medium horizontal phase-speeds (slower approx. 30 m/s) and moderate horizontal wavelengths (500km in our simulation) are represented by green color, very fast gravity waves (horizontal phase-speeds larger than 50m/s) are represented by blue color and gravity waves with more than 1000km horizontal wavelength are represented by red color. Many of these waves propagate obliquely. This induces different propagation pathways for realistic propagation and the usually assumed vertical propagation and leads to differences between GWDV and GWDO. For details see text.

# 5. Ray-tracing simulations of convective gravity waves

## 5.1. The Yonsei convective gravity wave source model

### 5.1.1. Overview

In the last chapter a non-orographic gravity wave launch distribution was applied to simulate waves from a broad variety of sources (e.g. fronts, convection, geostrophic adjustment). This non-orographic launch distribution does not account for any individual gravity wave source. However, the launch distribution is optimized by comparison of simulated global distributions of measured momentum flux and temperature amplitude with results obtained from observations [Preusse *et al.*, 2009]. The boundary conditions (e.g. launch altitude, direction, phase speeds spectrum) are constant in space and time.

Propagation and dissipation of gravity waves can be deduced relatively straightforward from theory and are therefore accepted to

## CHAPTER 5. RAY-TRACING SIMULATIONS OF CONVECTIVE GRAVITY WAVES

---

a large degree [McLandress, 1998]. The results of the comparison shown in chapter 3 support the approach of many non-orographic parametrizations in GCMs. A well chosen spectral distribution of gravity waves launched below the tropopause captures already many features of the real gravity wave distribution. However, observations indicate a larger degree of zonal asymmetry, requiring the inclusion of localized sources. Also, the comparison in chapter 3 was performed on a logarithmic scale and even in this comparison larger differences due to missing sources are noticeable. In particular for those regions where previous studies indicated orographic or convective gravity wave excitation.

This is especially true for dynamic sources like deep convection. The general importance of convectively forced gravity waves led to an ongoing development of parametrizations for gravity wave drag from deep convection (GWC) [Chun and Baik, 1998, Beres et al., 2004, Chun et al., 2004]. Further studies [Chun et al., 2004, Beres et al., 2005, Song et al., 2007] have shown the importance of GWC parametrization to achieve a more realistic representation of gravity waves in the middle atmosphere and particularly in improving the QBO [Kim et al., 2013]. One major restriction of these models is the restriction of gravity wave propagation to one vertical model column, thus, a more realistic oblique propagation of gravity waves is not addressed. This simplification is useful to reduce computational effort, but it does not represent the underlying gravity wave dynamics very well as seen in chapter 4. The focus of this chapter is in particular on the influence of convectively excited gravity

## 5.1. THE YONSEI CONVECTIVE GRAVITY WAVE SOURCE MODEL

---

waves and their interaction with tropical and low latitude winds. For this reason, the Yonsei convective gravity wave source model [Song and Chun, 2005, Song et al., 2007] was applied to generate the launch distribution for ray-tracing calculations using the GRO-GRAT ray-tracer. A comparison with SABER (remote sounding instrument on the TIMED satellite - see section 5.3) gravity wave momentum flux and temperature squared amplitude data with respect to the physical restrictions of the instrument itself is also presented in this chapter. The SABER instrument is able to resolve gravity waves with horizontal wavelengths (approximately) as short as 100km [Preusse et al., 2002, Alexander et al., 2010a, Ern et al., 2011]. Wavelengths shorter than 100km are hardly visible to the instrument [Trinh et al., 2014]. Further, the visibility function of the instrument is responsible for an underestimation of short horizontal wavelengths and therefore introduces a low bias of the resulting respective momentum flux. In order to estimate the error from the influence of instrument limitations on gravity wave distributions, an observational filter has been introduced. The intention is to simulate the tropical gravity wave spectrum as seen from SABER in order to assess ray-tracing results with global gravity wave momentum flux measurements. This offers the opportunity to distinguish the part of the gravity wave spectrum which is in principle visible to the instrument from parts of the spectrum which have to be evaluated by other measurement techniques (e.g. super-pressure balloons).

Since the Yonsei convective gravity wave source model was designed to properly work with general circulation models (GCMs),

regardless of the spatial scale or the time integration constant used, some parameters remain free to adjustment. There are two parameters ( $\delta_x$ ,  $\delta_t$ ) accounting for the spatial scale and time scale of a convective event. Also, the wave filtering and resonance factor [Song and Chun, 2005] can be adjusted to directly fit the source model to the observational data. The subsequent trajectory and amplitude calculations away from the convective source at cloud top height were performed using the GROGRAT gravity wave ray-tracer. The combination of both, the source model and the ray-tracer, offers the opportunity to distinguish between the influence of (tropical) deep convection as the excitation process and wind filtering effects. As a result, comparisons between gravity wave momentum flux observations and their simulation can be presented for global distributions and at different altitude levels.

### 5.1.2. Mathematical description

Chun and Baik [1998] first formulated a parametrization of convectively forced gravity waves for a vertically uniform background wind in a stable (neglecting turbulent shear flow) atmosphere. This parametrization significantly contributed to the zonal background wind and temperature of the Yonsei atmospheric general circulation model (AGCM) [Chun *et al.*, 2001] and the NCAR<sup>1</sup> Climate Model 3 [Chun *et al.*, 2004]. These first attempts on convection as a source of gravity waves account only for gravity waves stationary with respect to a moving cloud and were therefore not able to

---

<sup>1</sup>National Center for Atmospheric Research, Boulder, Colorado (US)

## 5.1. THE YONSEI CONVECTIVE GRAVITY WAVE SOURCE MODEL

---

consider high-frequency gravity waves above cumulus clouds that have been observed and simulated [Fovell *et al.*, 1992, Pfister *et al.*, 1993, Preusse *et al.*, 2001, Beres *et al.*, 2002, Ern and Preusse, 2012, Ern *et al.*, 2013]. Depending on the observational technique and the model used, different scales are in the focus of the investigation. Horizontal wavelengths may range from a few kilometers [Jewtoukoff *et al.*, 2013] up to several thousand kilometers [Preusse, 2001]. The analytic formulation of diabatic gravity wave forcing [Song and Chun, 2005] overcomes the limitations of Chun and Baik [1998] and also accounts for deep convective forcing. Further applications of this model (see sections 5.2 and 5.3) show its performance in comparison with satellite observations. Observations do only partly cover the spectrum of gravity waves. The limitations for infrared limb-soundings and potential effects on the global distribution are discussed in chapter 5.3 But first, a short overview of the mathematical formulation of the convective gravity source model and its derivation is given in the next paragraph. This derivation goes back to Chun and Baik [1998] and Beres *et al.* [2002] and was later extended to include (non-)stationary gravity wave spectra generated by convection. Considering a two-dimensional, hydrostatic, non-rotating, inviscid, and Boussinesq atmosphere, small amplitude

CHAPTER 5. RAY-TRACING SIMULATIONS OF  
CONVECTIVE GRAVITY WAVES

---

perturbations can be expressed as

$$\frac{\partial u'}{\partial t} + \vec{U} \frac{\partial u'}{x} + \frac{d\vec{U}}{dz} w' + \frac{\partial \phi}{\partial x} = 0 \quad (5.1a)$$

$$\frac{\partial \phi}{\partial z} = b \quad (5.1b)$$

$$\frac{\partial b}{\partial t} + \vec{U} \frac{\partial b}{\partial x} + N^2 w = \frac{gQ}{c_p T_0} \quad (5.1c)$$

$$\frac{\partial u'}{\partial x} + \frac{\partial w'}{\partial z} = 0 \quad (5.1d)$$

with  $u'$  and  $w'$  as the horizontal and vertical perturbation wind velocities,  $\phi = p'/\rho_0$  the normalized ( $\rho_0 =$  basic state density) pressure perturbation,  $b = g\Theta'/\Theta_0$  as the buoyancy perturbation (where  $g$  is the gravitational acceleration,  $\Theta'$  the temperature perturbation, and  $\Theta$  the reference potential temperature). The vector  $\vec{U}$  is the basic state wind,  $N$  is the buoyancy frequency of the background atmosphere,  $c_p$  the specific heat of air at constant pressure, and  $Q$  the latent heat released from the cloud. Combining equations 5.1a-5.1d and applying a Fourier transform in time and one spatial direction afterwards leads to the Taylor-Goldstein equation [*Goldstein, 1931*] for convectively forced linear gravity waves<sup>2</sup>:

$$\frac{\partial^2 \hat{w}}{\partial z^2} + \left[ \frac{N^2}{(U-c)^2} - \frac{d^2 U/dz^2}{(U-c)} \right] \hat{w} = \frac{g\hat{q}\zeta_q}{c_p T_0 (U-c)^2} \quad (5.2)$$

Here  $\hat{w}$  and  $\hat{q}$  are the Fourier transformed of  $w$  and  $q$ ,  $\zeta_q$  is the vertical heating profile ( $Q = q(\vec{x}, t)\zeta_q(z)$ ).

---

<sup>2</sup>In a wave-vector aligned coordinate system

## 5.1. THE YONSEI CONVECTIVE GRAVITY WAVE SOURCE MODEL

---

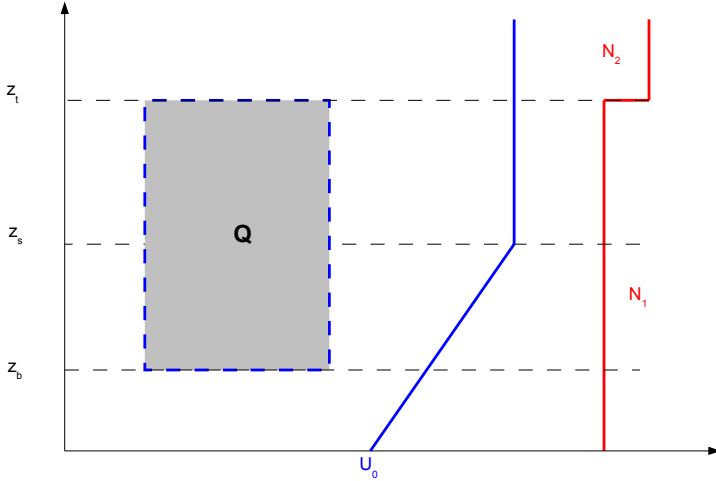


Figure 5.1.: Schematic overview of the basic-state wind and stability used in this study. The symbols  $z_b$ ,  $z_t$ , and  $z_s$  represent the bottom and top altitudes of the diabatic forcing region  $Q$  and the shear level altitude.  $U_0$  and  $U_t$  are background winds at the surface and the top level of the forcing.  $N_1$  and  $N_2$  are buoyancy frequencies with non-continuous transition at the top of the forcing region.

A three layer atmosphere is assumed to solve equation 5.2 in three vertical sections (see Figure 5.1). In the section below  $z_b$  (bottom altitude of the convective forcing) and above  $z_t$  (top altitude of the convective forcing) equation 5.2 becomes homogeneous. The section of the latent heat release is found between  $z_b$  and  $z_t$  with a non-zero right hand side in Equation 5.2. Further, a shear layer from the

## CHAPTER 5. RAY-TRACING SIMULATIONS OF CONVECTIVE GRAVITY WAVES

---

ground to some shear level  $z_s$  is assumed. Above this shear level the background wind profile is assumed to be constant with altitude and the buoyancy frequency has a non-continuous transition from  $N_1$  to  $N_2$  at the top of the forcing region. The momentum flux can then be calculated as:

$$\bar{F} = \rho_0 \overline{u'w'} = \frac{1}{L_x L_t} \int \int \rho_0 u' w' \mathbf{d}x \mathbf{d}t \quad (5.3)$$

The constants  $L_x$  and  $L_t$  represent appropriate spatial and temporal scales for averaging and have to be set according to the atmospheric background grid size<sup>3</sup>. The momentum flux calculated by this model represents only gravity waves propagating outside of the forcing region. Momentum flux inside the forcing region (e.g. storms) are mainly due to turbulence and therefore neglected. After integration of equation 5.3 the momentum flux is obtained as

$$\bar{M}(c) = -sgn(U_t - c) \rho \frac{2(2\pi)^2}{L_x L_t} \left( \frac{g}{c_p T_0 N_1^2} \right)^2 \frac{N_2}{|U_t - c|} |X|^2 \Theta(c) \quad (5.4)$$

The parameter  $|X|^2$  is called the wave-filtering and resonance factor and represents the interference of the Fourier transform at the borders of each of the three modelled layers. It is derived and discussed in detail in *Song and Chun* [2005]. The diabatic heating source function  $\Theta(c)$  assumes a forcing to be a Gaussian distribution in space

---

<sup>3</sup>Atmospheric circulation models solve the dynamic equations by spatial and temporal discretisation. Therefore, the averaging domain for the convective gravity source model is at least equal to this discretisation grid.

and time as derived in *Song and Chun* [2005]:

$$\Theta(c) = \frac{2q_0^2}{\delta_x} \left( \frac{\delta_x \delta_t}{16\pi} \right)^2 \frac{\sqrt{\pi/2}}{\sqrt{1 + (c - c_q)^2/c_0^2}} \quad (5.5)$$

with  $c_0 = \delta_x/\delta_t$  and  $\delta_x$ ,  $\delta_t$  as widths of the Gaussian. Equation 5.4 is the major outcome of the convective model and presents the momentum flux of convective gravity waves as a phase speed spectrum. Besides the tuning parameters  $L_x$ ,  $L_t$ , and  $\delta_x$ ,  $\delta_t$  the initial propagation direction of each wave has to be assumed. In order to achieve a well presented angular sampling of the wave field and to be consistent with the gravity wave background parametrization used eight equally distributed launch angles have been chosen.

### 5.1.3. Implementation and coupling with GROGRAT

As described in section 5.1.2, the parameters  $\delta_x$  and  $\delta_t$  represent the spatial and temporal scales of the convection and largely influence the horizontal wavelength and periods of the excited waves. Several sets of parameters were used. Two parameter sets (MF1 and MF2) for the convective source have already been introduced in *Choi et al.* [2012]. MF1 has a typical maximum in the momentum flux for waves of 10km horizontal wavelength which is not visible to limb-sounders. MF2 has been introduced for a better comparison with AIRS (Atmospheric InfraRed Sounder) observational data. The peak in the horizontal wavelength spectrum was found at 50km with a 15 times smaller intensity compared to MF1. To further improve the rep-

## CHAPTER 5. RAY-TRACING SIMULATIONS OF CONVECTIVE GRAVITY WAVES

---

resentation of measurable gravity waves, another set of spatial and temporal scaling parameters - MF3 - will be introduced later in this chapter.

It is noteworthy that the momentum flux at cloud top can be also scaled by an additional factor. This additional factor depends strongly on the dataset used and should also be considered for a better comparison with measurements. It expresses the efficiency of the wave-filtering and resonance effects within the convective forcing region [Song and Chun, 2005]. To calculate propagation and momentum flux of gravity waves from convection, the convective source model was used as the launch distribution for the GROGRAT ray-tracer. The convective gravity wave source model calculates a momentum flux spectrum as a function of phase speeds. Horizontal wavelengths are estimated according to Choi *et al.* [2012] using equation 5.6

$$k_h = \frac{2\pi}{\delta_x} \frac{1}{\sqrt{1 + (c - c_q)^2/c_0^2}} \quad (5.6)$$

Here  $\delta_x$  is the spatial constant with respect to the model's grid size in kilometer. The horizontal speed of the convection is given by  $c_q$ . The characteristic velocity  $c_0 = \delta_x/\delta_t$  is the ratio of spatial and temporal model constants. The diagram in Figure 5.2 illustrates the connection between source model and ray-tracer. The source model uses heating profiles at every grid cell to calculate the convective forcing of gravity waves. Top and bottom of the forcing as well as an average forcing  $Q_0$  are determined from these profiles (see Figure 5.3a-5.3c for a depiction of the profile fitting). Cloud top and bot-

## 5.1. THE YONSEI CONVECTIVE GRAVITY WAVE SOURCE MODEL

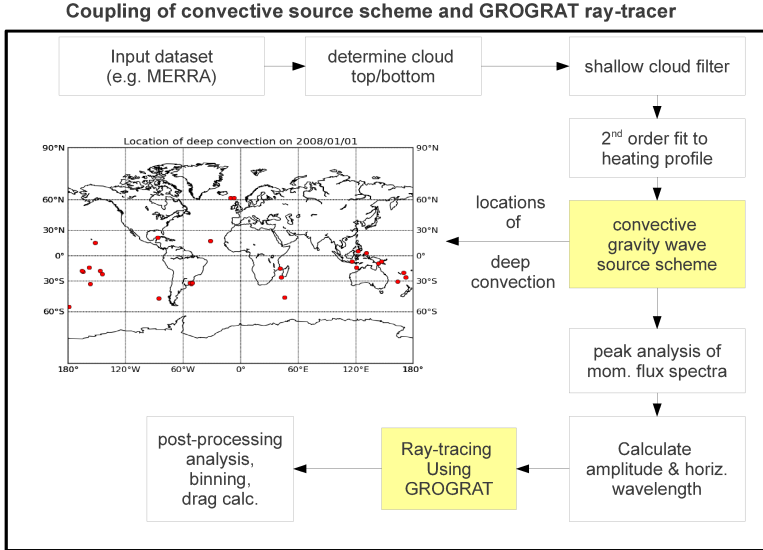


Figure 5.2.: Coupled convective gravity wave source model and GROGRAT ray-tracer. The input dataset (Merra data were used for this study) provides winds, temperature, geopotential, heating rates and cloud top height. Two preparative steps are performed to calculate the correct bottom and top of the heating source and to filter out shallow clouds. The resulting heating source characteristics are used as an input for the gravity source model. The GROGRAT ray-tracer uses the output data of the source as gravity wave characteristics together with the background atmosphere to calculate gravity wave trajectories. As a last step the usual statistical binning and analysis is applied to obtain derived quantities like gravity wave drag and squared temperature amplitudes.

## CHAPTER 5. RAY-TRACING SIMULATIONS OF CONVECTIVE GRAVITY WAVES

---

tom data from the MERRA dataset are used as a first guess to apply a second order fit to the heating profile. The analytical derivation of the source model [Song and Chun, 2005] assumes that the convection is of Gaussian shape. Therefore, the second order fit results are used to recalculate top and bottom of the forcing region. Altitude and forcing maximum are also needed as input variables for the source model. After a successful run of the source model, the output data have to be analyzed in terms of a peak analysis of the momentum flux spectrum. GROGRAT assumes single waves with discrete phase speed, horizontal wavelength and amplitude, thus, the maxima/minima of the momentum flux spectrum are used for the start spectrum. The phase speed determined by the peak analysis are further used for horizontal wavelength calculation. The amplitude of the wave can now be obtained by the following equation valid in mid-frequency approximation<sup>4</sup>:

$$\hat{u} = \sqrt{\frac{\lambda_x}{\lambda_z} \frac{2F_{px}}{\rho}} \quad (5.7)$$

With this input data GROGRAT runs can be performed for each individual wave found in the peak analysis of the convective source model output. The post-processing of the GROGRAT data is similar to the methods mentioned before and momentum flux, gravity wave drag and amplitude are calculated for a regular grid. These ray-tracing results consider only a convective source. The possible

---

<sup>4</sup>This equation is based on the polarization relations and have been derived analogously to 2.11 [Ern et al., 2004]

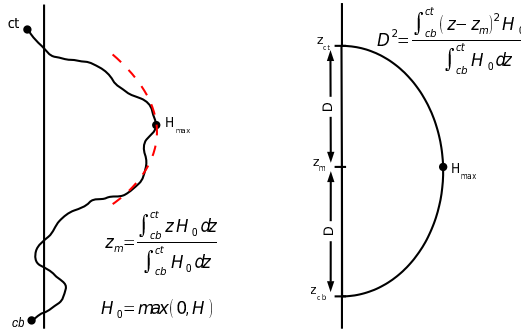
contribution to the momentum flux distribution from other sources than convection was also considered in order to compare the simulation results with observations. For this reason, a non-orographic launch distribution for gravity waves in particular at high latitudes was used as a background. This scheme mainly influences the momentum flux at high latitudes for the following reasons: The high amount of gravity waves from convective sources in low latitudes yields a much higher weight of convective waves compared to the background parametrization. At high latitudes, however, convective gravity waves are out-numbered by the non-orographic waves. Therefore, high latitude momentum flux is prominently induced by non-orographic waves. Another problem to consider when comparing simulations with observations is the spectral visibility of convective gravity waves to limb-sounding instruments. Gravity waves generated by the Yonsei convective source scheme may have, depending on the choice of  $\delta_x$  and  $\delta_t$ , very short horizontal wavelengths which are unlikely to be resolved by limb-sounding instruments like SABER and HIRDLS. The influence of the observational filter on the global distribution will be addressed in chapter 5.3

### 5.1.4. Application using the Merra dataset

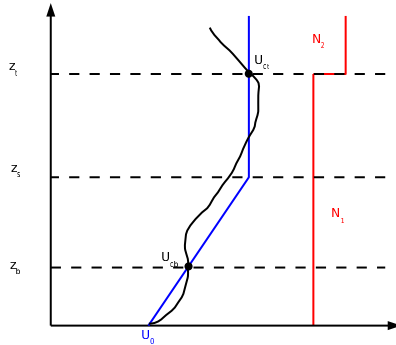
For the following investigations on convective gravity waves the Merra dataset [*Rienecker et al., 2011*] was used as source for altitude-resolved heating rates. For consistency, atmospheric background fields of wind, temperature, and geopotential were also taken from the same dataset. Merra data include several ground based, in-situ,

CHAPTER 5. RAY-TRACING SIMULATIONS OF  
CONVECTIVE GRAVITY WAVES

---



(a) Sketch of an exemplary heating profile.  
(b) Second order fit to the heating profile.



(c) Retrieving relevant data from the three layer atmospheric model.

Figure 5.3.: Profile fitting of diabatic heating rates to determine top/bottom altitude of the convection ( $z_{cb}, z_{cz}$ ), the maximum heating  $H_0$ , and atmospheric background conditions.

## 5.1. THE YONSEI CONVECTIVE GRAVITY WAVE SOURCE MODEL

---

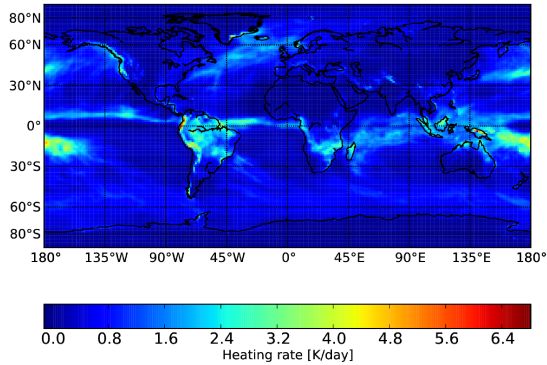
and satellite measurements through 3DVAR assimilation into the Goddard Earth Observing System (GEOS) [Suarez *et al.*, 2008]. It supports a horizontal resolution of  $1/2^\circ$  longitudinal and  $2/3^\circ$  latitudinal with 72 levels up to 70km with assimilated satellite data up to the middle mesosphere. Several studies showed the reliability of this record<sup>5</sup> [Bosilovich *et al.*, 2011] especially for precipitation and heating rates. The Yonsei convective scheme requires reliable heating rate profiles and their analysis in terms of bottom, top and maximum heating.

---

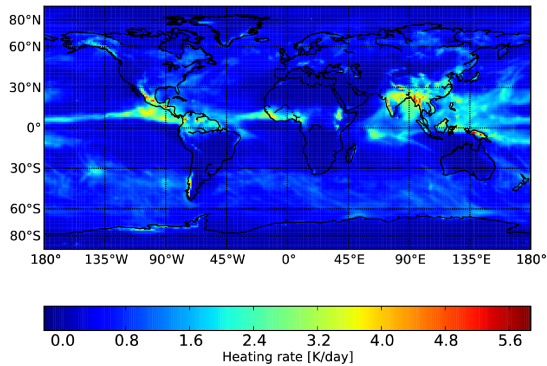
<sup>5</sup>First Merra data are available for 1979 and already implemented the very first satellite observations of the middle atmosphere. Further information can be obtained from:  
<http://disc.sci.gsfc.nasa.gov/daac-bin/DataHoldings.pl>

## CHAPTER 5. RAY-TRACING SIMULATIONS OF CONVECTIVE GRAVITY WAVES

---



(a) January 2008



(b) July 2008

Figure 5.4.: Heating rates from Merra dataset (average between 3-12km) for two representative seasons of 2008.

## 5.1. THE YONSEI CONVECTIVE GRAVITY WAVE SOURCE MODEL

---

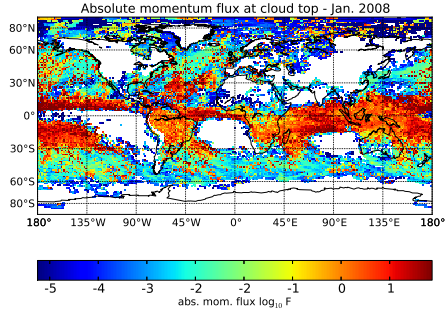
Figure 5.4a shows Merra average heating rate profiles for averaged January 2008. High values of about 4K/day are found over the pacific ocean. Also South America, the south part of Africa and Madagascar, and the West Pacific region show higher heating rates around 2-3.5K/day. These are the typical rain forest regions with high amounts of precipitation and evaporation. Another feature are higher values along the inter-tropical convergence zone (ITCZ) in the Pacific and Atlantic ocean close to the equator. Comparing these findings with the July 2008 heating rates shown in Figure 5.4b, obviously the maximum heating regions are shifted to the northern hemisphere. Highest values about 5K/day are found in India and Indochina, but also in middle America. The heating rates in Africa are lower (2.5K/day), but still a pronounced feature. It is expected to find regions of maximum momentum flux at cloud top level (source level) to be close to the regions of maximum heating rates. Figures 5.5a and 5.5b show momentum flux at cloud top height for average January 2008 and July 2008 conditions. They show that, in first order, momentum flux at cloud top height is correlated to average heating rates from Figures 5.4a and 5.4b. The depth of the heating is another major factor influencing the momentum flux distributions at cloud top height. Thus, not only the pacific and continental regions show remarkable momentum flux forcing. For instance, the Indian Ocean region is another strong source of convective gravity waves. Further, the large regions of shallow clouds (flagged white due to the shallow cloud filter in Figures 5.5a and 5.5b) do not contribute as gravity wave source regions.

### 5.1.5. Source level momentum flux

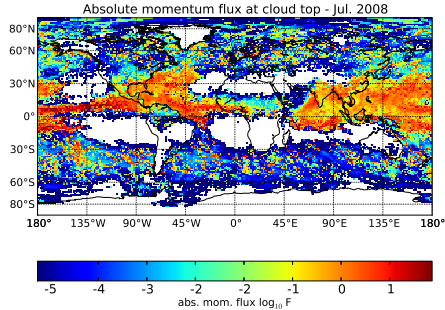
The convective gravity wave source model calculates momentum flux at the source level - the top of the convective cell where the simulated gravity waves are launched by GROGRAT. The result of the global momentum flux calculation is shown in Figure 5.6 for January 2008 conditions. For each longitude-latitude box the cloud top altitude is shown as the height of the surface. Color (logarithmic scale) denotes the momentum flux. Higher momentum flux values are typically found in regions of large convective towers (e.g. tropics). In higher-latitude regions, convective excitation of gravity waves remains low. Remarkable are regions west of South America, Africa and Australia where almost no momentum flux is provided for launch. The altitude of the source level indicates that either clouds with a very low altitude cloud top or on average no clouds can be found there. Shallow clouds (clouds with vertical extend lower than 4km) do not contribute much to the momentum flux budget at source level [*Song and Chun, 2005*] and are therefore neglected to improve calculation efficiency. Figures 5.5a and 5.5b show the typical seasonal distribution of momentum flux at cloud top height. The main forcing regions in the tropics follow well the ITCZ thus, they are found in the southern hemisphere during January 2008 and in the northern hemisphere during July 2008. Further, the excitation is also remarkable above the continents due to the known deep convection above the rain forests. In particular, the Asian Monsoon region show strong momentum flux values at source level. But deep convection can be also found at higher latitudes.

## 5.1. THE YONSEI CONVECTIVE GRAVITY WAVE SOURCE MODEL

---



(a) January 2008



(b) July 2008

Figure 5.5.: Calculated momentum flux (logarithmic scale) at cloud top height for January and July 2008. Highest values are found within the tropics close to the inter-tropical convergence zone (ITCZ) for January. Further, a strong forcing is found in south America, south Africa and Australia. Shallow clouds in the south Pacific, south Atlantic and south Indian Ocean regions as well as above north American and Asian continents (white) excite only low amplitude gravity waves and are therefore neglected due to performance optimization of the coupled model. The ITCZ region is shifted to the northern hemisphere during July, thus, main convective forcing region are obtained in middle America and Indonesia.

Tropical cyclones and mid-latitude storms are another major source of gravity wave momentum flux due to deep convection which has been already a subject of study [*Lehmann et al.*, 2012]. High momentum flux values are already found close to the sources (see section 5.2). This is either an indication that many evanescent gravity waves are excited or that gravity waves are physically filtered due to critical wind shear filtering close to the top of the convective forcing. Secondly, after a major amount of gravity waves have been filtered out, the remaining gravity waves form a spectrum which undergoes further wind filtering with altitude. Thus, the GROGRAT ray-tracing model was used to transfer momentum flux from the convective source to the middle atmosphere while allowing three-dimensional propagation of the forced gravity waves and accounting for wind filtering and dissipation. Both, the distribution of the sources and the wind filtering render the observed horizontal tropical distributions of gravity waves.

## 5.2. Ray-tracing of convective gravity waves

As mentioned before, there are free parameters in the convective source model which cannot be constrained by theory. The aim is to constrain these parameters by comparing modelled distribution of momentum flux to global observations. In this section three sets of parameters are presented in order to best fit the simulated global momentum flux distributions to satellite observations. Previous studies [*Choi et al.*, 2009, 2012] indicate a need for such a further tuning

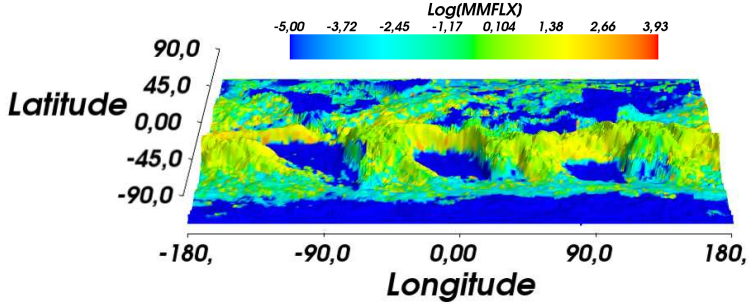


Figure 5.6.: Three-dimensional representation of calculated momentum flux (color) at cloud top height for January 2008.

of the source model to resemble satellite observations in particular. Observational studies on the other hand show a different location of the spectral peak especially in the low horizontal wavelength region [Ern and Preusse, 2012]. In order to investigate the influence of the free parameters  $\delta_x$  and  $\delta_t$ , three parameters sets (referred to MF1, MF2, and MF3) listed in Table 5.1 are used. The first two sets were introduced in Choi *et al.* [2012].

Figure 5.7 shows the momentum flux spectrum as a function of horizontal and vertical wavelength at 25km altitude for January 2008. The spectrum was calculated by binning momentum flux values from single waves with respect to their horizontal wavenumber  $k_h = 2\pi/\lambda_h$  and vertical wavenumber  $m = 2\pi/\lambda_z$  in logarithmic coordinates ( $\tilde{k}_h = \log_{10}(k_h^{-1})$  and  $\tilde{m} = \log_{10}(m^{-1})$  with grid spacings of  $\delta\tilde{k}_h = 0.1$  and  $\delta\tilde{m} = 0.1$  and an overlap of  $\Delta\tilde{k}_h, \tilde{m} = 0.2$ . Momen-

## CHAPTER 5. RAY-TRACING SIMULATIONS OF CONVECTIVE GRAVITY WAVES

---

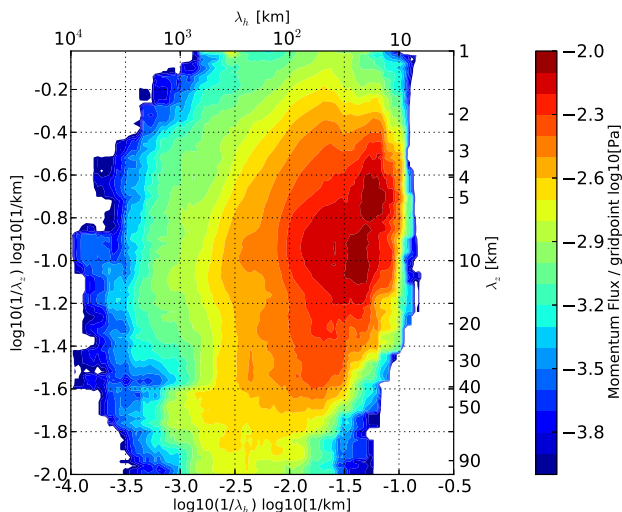


Figure 5.7.: Momentum flux per gridpoint as a function of horizontal and vertical wavelength for MF1 parameter set at 25km altitude for January 2008 conditions.

tum flux values are added for each bin and normalized with respect to the average momentum flux found at that particular altitude. The central peak of this MF1 parameter set ( $\delta_x = 5\text{km}$ ,  $\delta_t = 20\text{min}$ ) is obtained at approximately 15km horizontal wavelength and 10km vertical wavelength. This is close to findings from *Choi et al.* [2012] where a peak horizontal wavelength of 10km was reported. Deviations to results presented here may arise from different ray-tracing models used. In *Choi et al.* [2012] and *Choi et al.* [2009] the gravity wave ray-tracer from *Song and Chun* [2008] was used to calculate

## 5.2. RAY-TRACING OF CONVECTIVE GRAVITY WAVES

---

Set	$\delta_x$ (km)	$\delta_t$ (min)
MF1	5	20
MF2	25	60
MF3	120	60

Table 5.1.: Spatial and temporal values for the free parameters of the Yonsei convective gravity wave source scheme. MF1 and MF2 have been introduced in *Choi et al.* [2012]. MF3 is introduced in this work to account large convective clusters (e.g. an ensemble of single convective cells distributed over a large region).

the propagation and amplitude of gravity waves. However, the trajectory calculation is also based on *Lighthill* [1967], but the change of the wavevector during propagation was neglected (which might slightly affect the propagation of gravity waves) and also the amplitude calculation is simplified compared to GROGRAT. Therefore, it is plausible that results calculated with GROGRAT might differ from those from the ray-tracer by *Song and Chun* [2008]. The result of this second parameter set (MF2,  $\delta_x = 25\text{km}$ ,  $\delta_t = 60\text{min}$ ) are presented in Figure 5.8. The maximum momentum flux per grid-point is now obtained at approximately 90km horizontal wavelength and 7km vertical wavelength. The maximum momentum flux is decreased by half an order of magnitude compared to Figure 5.8. Albeit the spectral distribution is shifted to longer horizontal wavelengths, the majority of the momentum flux caused by MF2 would still not be visible to an instrument like SABER which has a low likelihood for observing gravity waves with horizontal wavelengths shorter than 100km.

## CHAPTER 5. RAY-TRACING SIMULATIONS OF CONVECTIVE GRAVITY WAVES

---

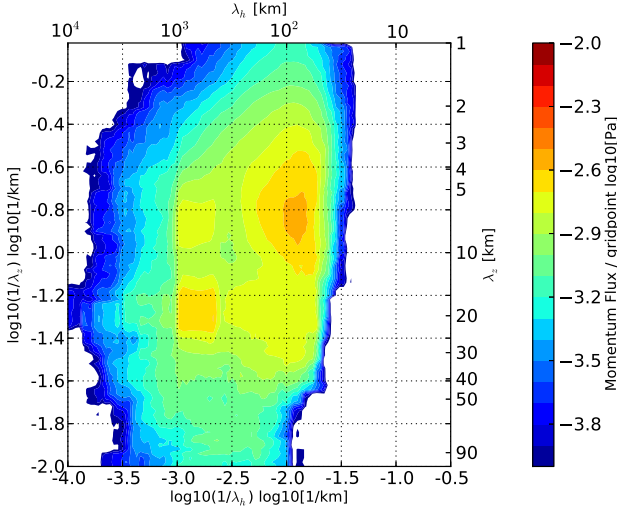


Figure 5.8.: Momentum flux per gridpoint as a function of horizontal and vertical wavelength for MF2 parameter set at 25km altitude for January 2008 conditions.

Therefore, another parameter set (MF3,  $\delta_x = 120\text{km}$ ,  $\delta_t = 60\text{min}$ ) is introduced here to account for large-scale convective clusters. The temporal scale is kept constant according to MF2 and only the spatial parameter is shifted towards longer scales to account for even larger convective events than MF2. The result is shown in Figure 5.9. The maximum average momentum flux is approximately 1.6mPa (i.e. -2.8 in log units) and found at 700km horizontal wavelength and 5.5km vertical wavelength. The whole horizontal spectrum consists of waves with horizontal wavelengths longer than 100km and

## 5.2. RAY-TRACING OF CONVECTIVE GRAVITY WAVES

---

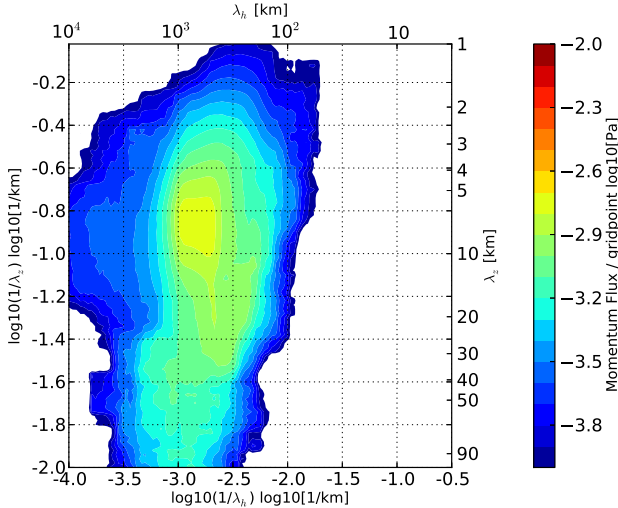


Figure 5.9.: Momentum flux per gridpoint as a function of horizontal and vertical wavelength for MF3 parameter set at 25km altitude for January 2008 conditions.

is therefore observable by a limb-sounding instrument. The location of this maximum is determined by the wave-resonance and interference factor  $X^2$  [Song and Chun, 2005]. This factor directly shapes the phase speed spectrum in terms of single peaks which are easy to ray-trace. As a result, the horizontal and vertical wavelength is determined due to the connection to the gravity wave dispersion relation (Eq. 2.5). The phase speed of each particular wave is, for instance, responsible for the filtering of gravity waves excited in the ITCZ regions already close to their source. In that case, the slow

## CHAPTER 5. RAY-TRACING SIMULATIONS OF CONVECTIVE GRAVITY WAVES

---

phase speeds lead to filtering in the troposphere with comparable slow wind speeds. So far, only spectral distributions of momentum flux of all three setups have been considered. The contribution of all three parameter sets to the global momentum flux distribution, the acceleration of the background flow (gravity wave drag), and the temperature amplitude of the excited waves are shown as zonal means in Figures 5.10-5.12. The calculated gravity wave momentum flux has been summed within bins of  $5^\circ$  in latitude and 1km in altitude and normalized with respect to the number of rays launched inside the same latitude bin. Therefore, a decay in e.g. momentum flux with altitude may be induced by either a decay in momentum flux per gravity wave or in a decreasing number of rays with altitude.

For the MF1 contribution, Figure 5.10 gives an overview of average momentum flux (upper row), gravity wave drag (middle row) and temperature amplitude (lower row) for January 2008 (left column) and July 2008 (right column). The discussed values are presented in color. Additionally, the background winds are plotted as contours. The momentum flux (logarithmic scale) shows a strong decay in amplitude from lower altitudes to higher altitudes. This decay is in good agreement to the filtering of gravity waves. As an example, waves in the winter hemisphere can propagate to higher altitudes due to the gain in amplitude of those waves propagating against the winter hemispheric jet. Especially gravity waves in the southern hemisphere mid-latitudes of July 2008 propagate up to 50km altitude until they are filtered out.

## 5.2. RAY-TRACING OF CONVECTIVE GRAVITY WAVES

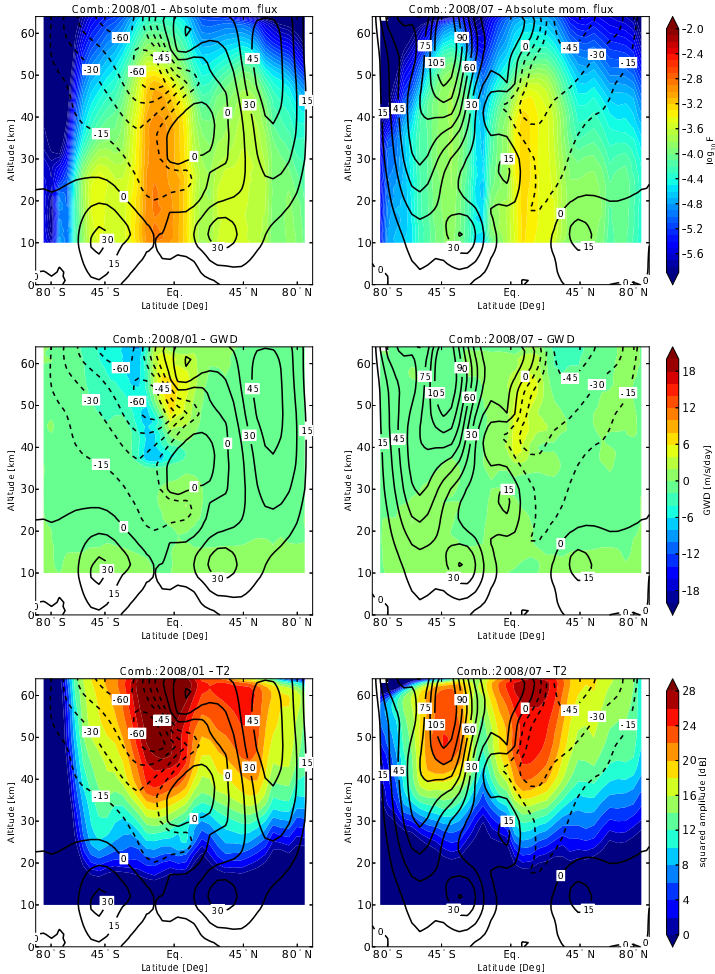


Figure 5.10.: Zonal averages for the MF1 setup of momentum flux (upper panels), gravity wave drag (middle panels), and temperature amplitudes (lower panels) for January 2008 conditions (left panels) and July 2008 conditions (right panels). For more details see text.

# CHAPTER 5. RAY-TRACING SIMULATIONS OF CONVECTIVE GRAVITY WAVES

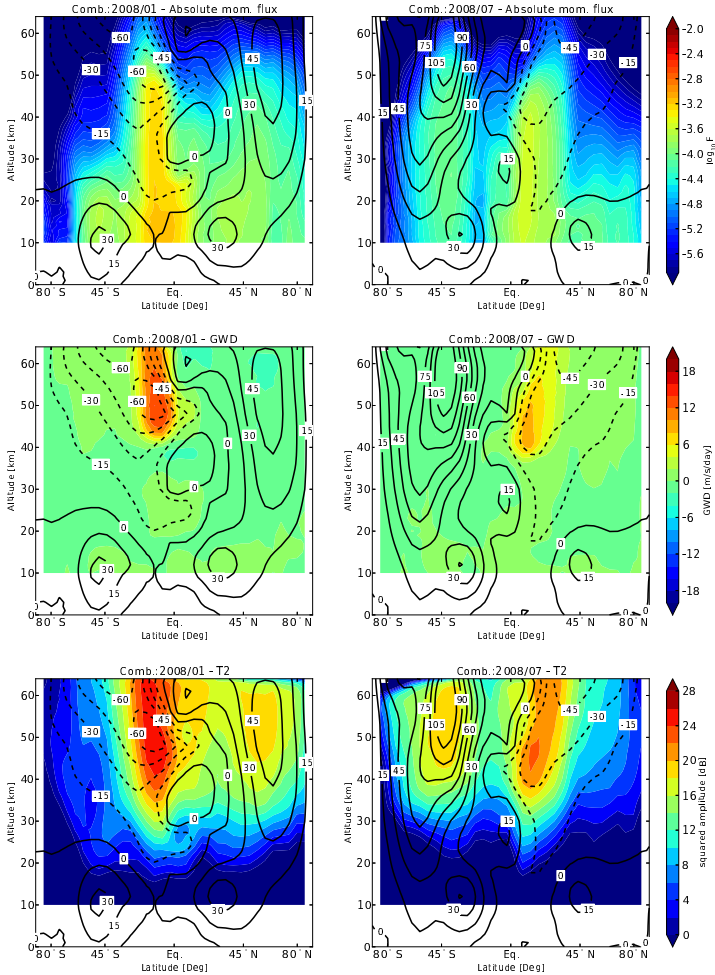


Figure 5.11.: Zonal averages for the MF2 setup of momentum flux (upper panels), gravity wave drag (middle panels), and temperature amplitudes (lower panels) for January 2008 conditions (left panels) and July 2008 conditions (right panels). For more details see text.

## 5.2. RAY-TRACING OF CONVECTIVE GRAVITY WAVES

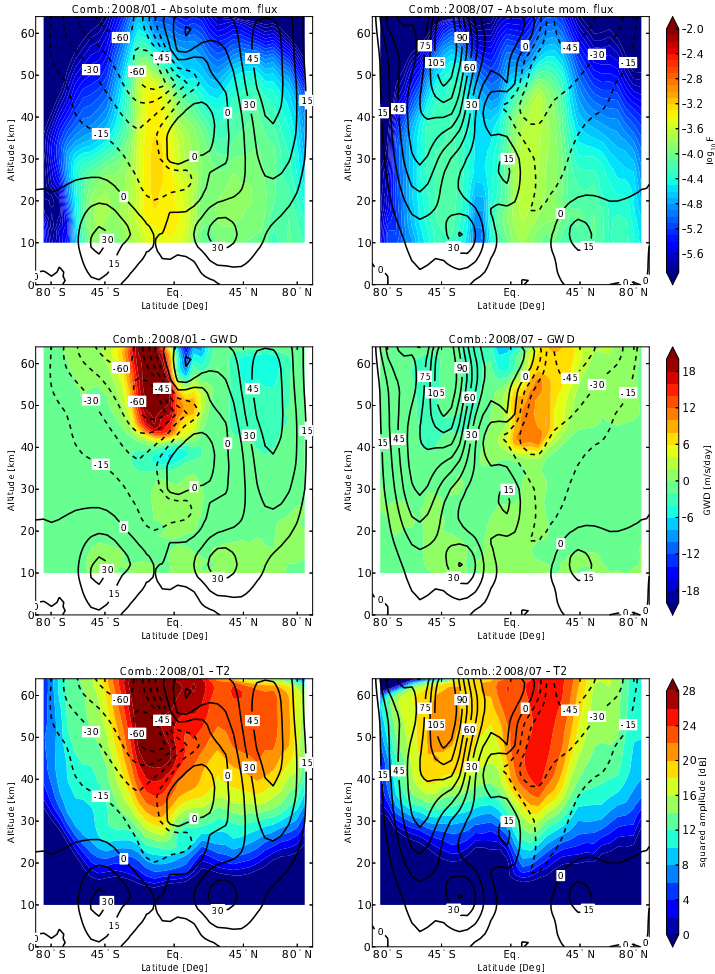


Figure 5.12.: Zonal averages for the MF3 setup of momentum flux (upper panels), gravity wave drag (middle panels), and temperature amplitudes (lower panels) for January 2008 conditions (left panels) and July 2008 conditions (right panels). For more details see text.

## CHAPTER 5. RAY-TRACING SIMULATIONS OF CONVECTIVE GRAVITY WAVES

---

The primary momentum flux peak arises in the tropics close to the equator ( $15^{\circ}\text{S}$  in January,  $15^{\circ}\text{N}$  in July). Comparing to the momentum flux at source height (cloud top) of Figures 5.5a and 5.5b, this is the region where the dominant contribution to the momentum flux distribution is found. Therefore, the distribution changes with the season according to the source. The northern hemisphere peak reaches altitudes of up to 45km and, as a result, is also important for the interaction with the quasi-biennial-oscillation (QBO). The middle row of Figure 5.10 shows the major gravity wave drag values within the tropics. The highest drag values are obtained during July at an altitude of 40-55km. Lower acceleration of the background flow can be found in the January 2008 simulation with an interesting interaction with the inner tropical QBO background winds at 28km and 50km altitude. These maximum acceleration of the background atmosphere is found to be within a  $10^{\circ}\text{N/S}$  latitude band and thus appear as an important pattern in terms of the interaction with the QBO. Further, the extra-tropical storm regions, which also contribute as sources of convective gravity waves (Figures 5.5a,5.5b) have little effect on the background atmosphere. The gravity wave drag from mid-latitudes to higher latitudes remains lower than  $1\text{ms}^{-1}\text{day}^{-1}$  in both seasons. This is in good agreement with previous studies [*Pulido and Thuburn, 2008*]. Finally, the squared temperature amplitude is plotted in the lower row of Figure 5.10. It is noteworthy, that these amplitudes represent the convective gravity waves alone, thus, these results should not be misinterpreted as observable amplitudes due to their lack of

## 5.2. RAY-TRACING OF CONVECTIVE GRAVITY WAVES

---

other sources. The observable amplitude within a given analysis region is the super-imposed amplitude of all gravity waves found in this region. Therefore, if only one source (like the convective source in this case) is simulated, the result does not need to correlate with observed squared amplitudes (e.g. in *Preusse et al.* [2009]). However, the squared amplitudes presented in Figure 5.10 shows some interesting structures which fit well to the background winds and their seasonal change. First of all, the exponential increase of squared temperature amplitude with altitude follows the general amplitude ( $u'$ ) behavior of gravity waves propagating upwards within an atmosphere. Therefore, the lowest amplitudes are found close to the source and as a result of the exponential decay of the atmosphere's density, the gravity wave amplitude increases with altitude. Assuming that polarization equations can be applied, this also includes an exponential increase in squared temperature amplitudes. Besides this general trend, lower amplitudes are found close to the summer hemisphere polar region indicating a small amount of waves travelling from convective sources towards the summer pole. Further, reduced amplitudes are found above the inner tropical wind reversal which indicates that many waves have been filtered out by this wind reversal and the remaining waves from higher latitude regions cannot fill the resulting gap in the gravity waves spectrum.

Figure 5.11 shows the momentum flux, gravity wave drag and temperature amplitudes for the MF2 parameter set of the source. Compared to the MF1 results, the momentum flux (upper row) remains lower with maximum momentum flux in the tropics. Gravity

## CHAPTER 5. RAY-TRACING SIMULATIONS OF CONVECTIVE GRAVITY WAVES

---

waves generated at mid- or higher latitudes are almost filtered out in the January data. Again, the southern hemisphere mesospheric winter jet (July data) carries a remarkable amount of waves to higher altitudes of up to 50km. Waves from the MF2 parameter set (longer horizontal waves compared to MF1 waves) appear to be more confined to the tropics due to a lower latitude coverage of the primary momentum flux peak in Figure 5.11 compared to 5.10. The acceleration (middle row) from this waves prominently occurs around 50km altitudes at  $10^{\circ}\text{N/S}$ . This acceleration maxima are found at regions where gravity waves do not encounter a wind reversal and strong wind filtering during upward propagation. For January this is at  $10^{\circ}\text{S}$  above the zero-crossing of the zonal wind below at 10km altitude. For July this pattern is obtained at  $10^{\circ}\text{N}$  and again exactly above the zero-crossing of the background zonal wind. The squared amplitude plots (lower row) show a higher amplitude (24dB) for exact these regions. Like in MF1, the gravity wave drag from a convective gravity wave source is confined to low latitudes. Additionally, a seasonal structure due to wind filtering is responsible for the hemispheric asymmetry in the maximum gravity wave drag. Finally, the MF3 simulation run follows the same structure, but with lower momentum flux values which are, same as MF2, particularly enhanced in low latitude regions (Figure 5.12, upper row). The drag is found to be higher for MF3 compared to MF2 and MF1 with values up to  $18\text{ms}^{-1}\text{day}^{-1}$ . The reason is a higher dissipation of MF3 waves with altitude and therefore a higher vertical momentum flux gradient which results in a higher drag. The gravity wave drag

## 5.2. RAY-TRACING OF CONVECTIVE GRAVITY WAVES

---

shows the same seasonal structure like in 5.11 as a result of the lower altitude wind reversal and the seasonality of the source. However, the temperature amplitudes are comparable to MF1 and MF2 and show highest values ( $>22$  dB) in the winter hemisphere mesosphere and again in the low latitudes with the hemispheric structure already obtained for MF1 and MF2. To further complete the picture of convective gravity waves, all three simulation runs have been super-imposed to one composite result. In general it is possible to introduce some weighting factors for all three parameter sets:

$$MF_{comb.} = C_1 * MF1 + C_2 * MF2 + C_3 * MF3 \quad (5.8)$$

where MF may denote either momentum flux, drag, or temperature amplitudes at the launch level. Following *Choi et al.* [2012], all constants  $C_i$  are set to one. Adjusting the values of  $C_j$  in the future, more detailed comparative studies between observations and modeling might be a possible way to estimate the true horizontal momentum wavelength distribution of tropical convective gravity waves. The momentum flux distribution in the upper row is similar to the momentum flux distribution of the MF1 (Figure 5.10). This is obvious due to the higher overall momentum flux of the MF1 simulation. Figure 5.13 shows the result of these super-imposed simulation runs.

## CHAPTER 5. RAY-TRACING SIMULATIONS OF CONVECTIVE GRAVITY WAVES

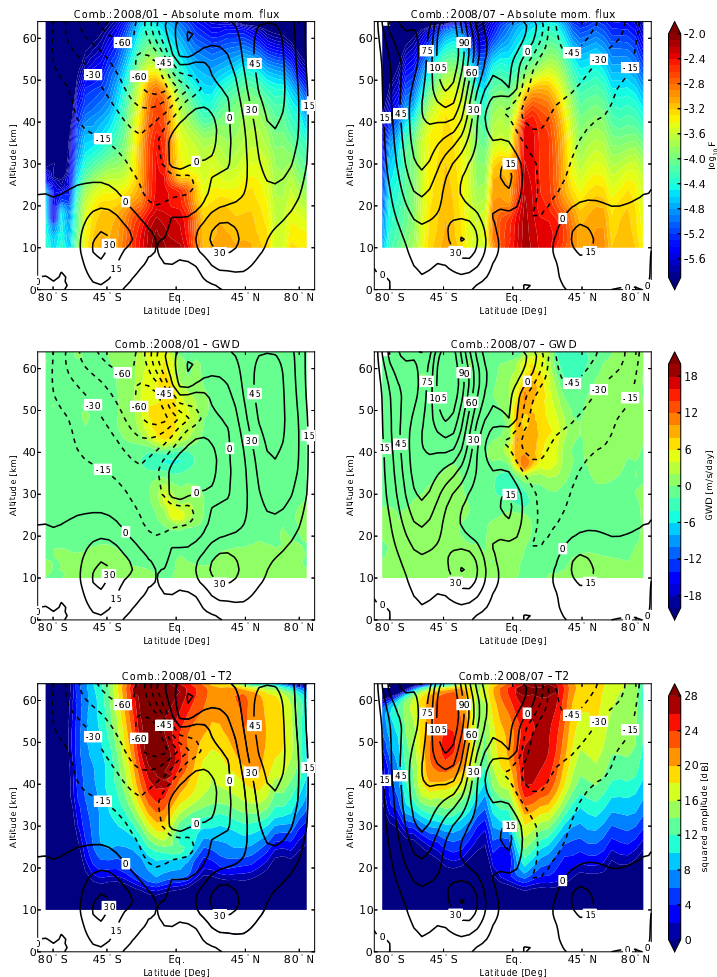


Figure 5.13.: Zonal averages for the combined setup of momentum flux (upper panels), gravity wave drag (middle panels), and temperature amplitudes (lower panels) for January 2008 conditions (left panels) and July 2008 conditions (right panels). For more details see text.

## 5.2. RAY-TRACING OF CONVECTIVE GRAVITY WAVES

---

Also the gravity wave drag (middle row) matches well the obtained structure of maximum values above the zero-crossing in background wind with the seasonal behavior like in the MF1,2,3 simulations. Accelerations of 18m/s/day in the upper stratosphere to lower mesosphere region as found in this combined simulation appear high. Previous studies report a derived stratospheric (<40km) gravity wave drag of less than 1m/s/day with an error margin of factor 2-3 [Ern *et al.*, 2014]. Ern *et al.* [2013] show gravity wave drag values of up to 5m/s/day at 60km altitude - again with an error margin of factor 2-3. One possible reason for the high simulated drag values is that simulations shown here do not consider other sources of gravity waves than convection. Important effects like the relative efficiency of different gravity wave sources and wave-wave interaction was neglected in this simulation. The temperature amplitudes of high-latitude waves in Figure 5.13 remain high, even though the number of convective waves propagating to those latitudes is very low compared to tropical regions. Momentum flux and squared temperature amplitude values of the extra-tropics should be carefully interpreted. Only a smaller number of gravity waves propagate to higher latitudes, thus, the sampling is not reliable for this regions. Figure 5.14 shows the number distribution for January and July of 2008 at 30km and 50km altitude for the combined MF1+MF2+MF3 run. The highest number of waves is found at 15°S for January and 10°N for July. Less than 10 percent of the amount of tropical waves is found at higher latitudes. Thus, ray-tracing results of convectively forced gravity waves can be trusted only up to a certain extend in

## CHAPTER 5. RAY-TRACING SIMULATIONS OF CONVECTIVE GRAVITY WAVES

---

this regions. An additional gravity wave source is needed for higher latitudes.

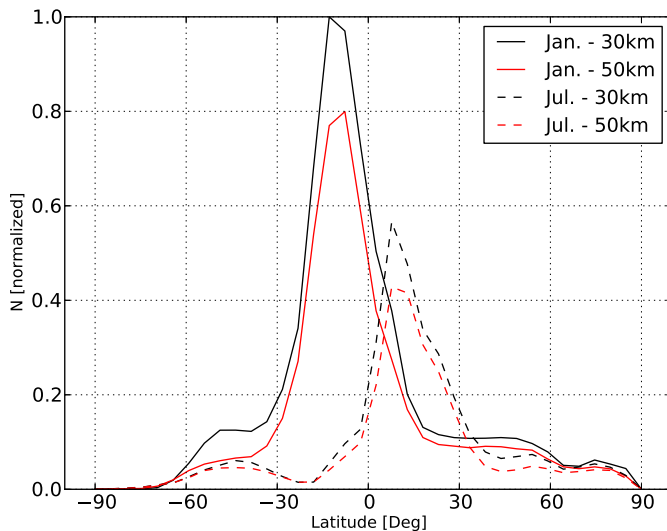


Figure 5.14.: Number distribution (normalized w.r.t. maximum number of rays per latitude-altitude bin) of combined MF1-MF3 rays for January 2008 (solid line) and July 2008 (dashed line) for 30km (black) and 50km (red) altitude. The majority of gravity waves is found in the tropics with a seasonal cycle following the inter-tropical convergence zone.

For the tropical region, Figure 5.15 shows maps of gravity wave absolute momentum flux (left panels) and temperature squared amplitudes (right panels) at 25km, 35km, and 50km altitude for Jan-

## 5.2. RAY-TRACING OF CONVECTIVE GRAVITY WAVES

---

uary (panels a-f) and July (panels g-l) 2008. The momentum flux at different altitudes shows some similar features to the momentum flux at cloud top height (Figures 5.5a and 5.5b). The deep convection source appears to have a higher activity above continents. Differences occur above oceans where high momentum flux values are found at source level (Figure 5.5a and 5.5a). The ray-tracing results show much lower forcing in that regions even close to the source at 25km (see Figure 5.15 - left panels). The east pacific region, the south Atlantic Ocean and the south Indian Ocean west of Australia show lower momentum flux values. In these regions the clouds are too shallow to generate gravity waves which would not be filtered out directly above the source. For January conditions these major convective gravity waves are found over central south America, south Africa and Indonesia between  $5^{\circ}\text{S}$  to  $10^{\circ}\text{S}$ . Because of the seasonal cycle (July conditions, see panels g-l of Figure 5.15) the maximum forcing region shifts northward towards  $5^{\circ}\text{N}$  to  $10^{\circ}\text{N}$ . Squared temperature amplitudes show the known growth with altitude from 12dB at 25km to more than 28dB at 50km altitude. Still, these amplitudes represent convective gravity waves only. Neither waves from other sources, nor more general background launch distribution (non-orographic launch distribution) are taken into account. Thus, these isolated convective wave amplitudes are higher than expected, but would probably decrease in a gravity wave simulation accounting for additional sources.

## CHAPTER 5. RAY-TRACING SIMULATIONS OF CONVECTIVE GRAVITY WAVES

---

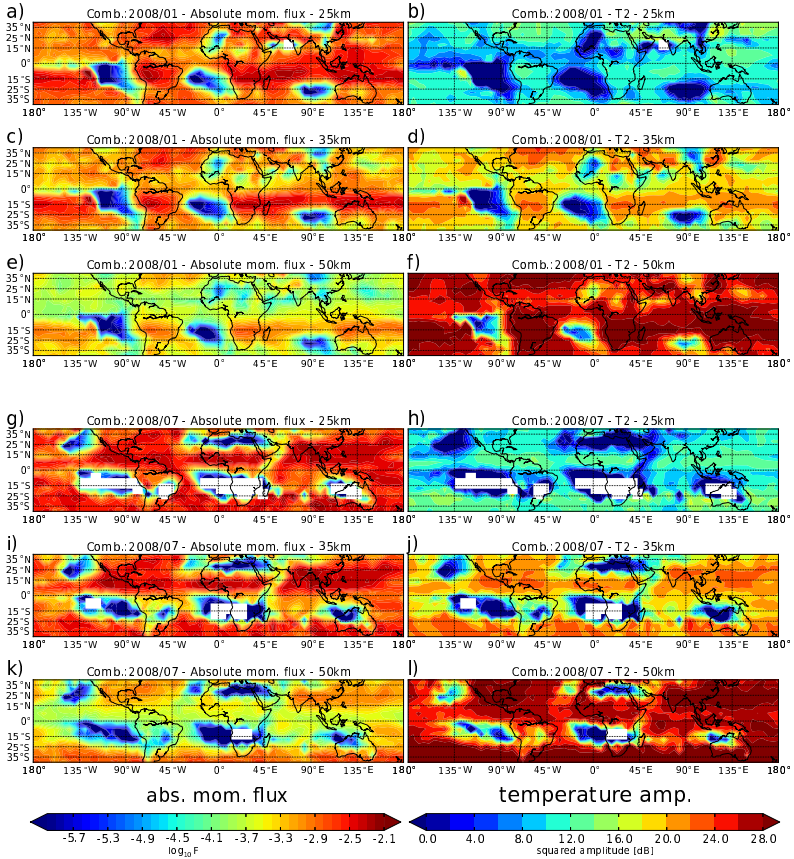


Figure 5.15.: Distribution of combined MF1+MF2+MF3 absolute momentum flux (left column) and temperature squared amplitude (right column) for January 2008 (panels a-f) and June 2008 (panels g-l). Momentum flux shows a decreasing trend with altitude. Prominent peaks are found above the continents. The latitudinal position of the peaks shifts with season towards the summer hemisphere. For further details see text.

## 5.3. Simulated convective gravity waves in comparison to satellite measurements

### 5.3.1. Limitations due to the observational filter

The SABER (Sounding of the Atmosphere using Broadband Emission Radiometry) [Mlynczak, 1997, Russell *et al.*, 1999, Yee *et al.*, 2003, Remsberg *et al.*, 2008] instrument on board of the TIMED (Thermosphere, Ionosphere, Mesosphere Energetics and Dynamics) satellite measures infrared radiation in the  $1.27\mu\text{m}$  to  $16.9\mu\text{m}$  band subdivided into 10 channels. From these infrared emission atmospheric temperatures can be derived from the tropopause region to well above 100km altitude with a vertical field-of-view of 2km. Measurements are done in limb-sounding geometry with the deep space background, thus atmospheric emissions are directly estimated. This measurement geometry implies some limitations to the observation of wave-like features with a sensitivity depending on horizontal and vertical wavelength of the wave. This sensitivity or visibility function accounts for the efficiency in wave detection [Preusse *et al.*, 2002]. Figure 5.16 shows the visibility function (contour) of a typical limb-sounding instrument. The number of gravity waves (logarithmic scale of combined setups MF1+MF2+MF3) with respect to horizontal and vertical wavelength is shown by color. Higher values of the visibility function show a high likelihood in detecting a wave. The vast amount of waves is found with horizontal wavelengths shorter than 500km. The visibility of such short waves is generally low and

## CHAPTER 5. RAY-TRACING SIMULATIONS OF CONVECTIVE GRAVITY WAVES

---

hard to observe. Also, gravity waves with horizontal wavelengths between 100km and 200km can only be observed, if their vertical wavelength is less than 8km<sup>6</sup>. It is noteworthy that even waves with longer horizontal wavelengths are affected and their amplitude will be underestimated in observations. For this study, a simplified observational filter was used. Further investigations on the impact of limb-sounding geometry on the observation of gravity waves are in progress. Yet, for an estimation of observational limitations it is reasonable to consider only waves with horizontal wavelengths longer than 100km. A more sophisticated attempt to account for observational limitations of limb-sounding instruments, sampling issues, and the visibility of modelled convective gravity waves with regards to their spatial and temporal scale is beyond the scope of this thesis and will be addressed in *Trinh et al.* [2014].

The coupled model of convective gravity wave source parametrization and GROGRAT ray-tracer is used to obtain the influence of the instrumental limitation due to the limb-sounding measurement geometry. For this purpose, the analysis of the ray-tracing results have been extended by a simple approach sorting out gravity waves which cannot be observed by SABER. A simple restriction of 100km for the lowest observable horizontal wavelength is applied according to *Ern et al.* [2004]. Only waves which can pass the observational filter are considered in the later calculations and binning process. This will affect the majority of gravity waves excited in the original MF1 setup of the convective source model. The MF2 setup adds some

---

<sup>6</sup>Depending on the orientation of the horizontal wavevector

### 5.3. SIMULATED CONVECTIVE GRAVITY WAVES IN COMPARISON TO SATELLITE MEASUREMENTS

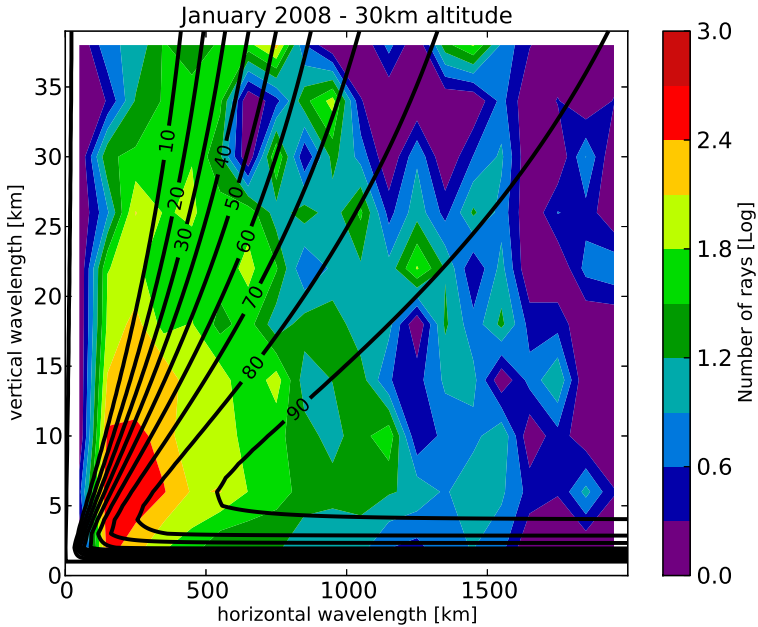


Figure 5.16.: Convective gravity waves (color) visible to a limb-sounding instrument. Visibility function [Preusse *et al.*, 2002] is depicted as contour lines. Numbers show what percentage of temperature amplitudes is retained in the measured radiance signal. Most convective gravity waves (from source setups MF1-MF3) have a short horizontal wavelength and are therefore almost invisible to limb-sounding instruments.

more longer waves within the horizontal wavelength range of approximately 80km, thus, many waves will be filtered out again. The

third setup, MF3, adds waves which can pass this simple observational filter, but still carry less momentum flux. Therefore, the combined setup is used for the gravity wave source in order to simulate the observations from the SABER satellite in tropical regions. For global comparisons, a non-orographic parametrization was added for the representation of high latitude gravity wave sources. The results of this composite gravity wave momentum flux distribution is discussed in section 5.3.3.

### 5.3.2. Results

For this study, the convective gravity wave source scheme has been set up with the combined parameter setup from section 5. The coupling of the source model and the GROGRAT ray-tracer are according to this previous work and only extended in terms of the additional observational filter to investigate uncertainties in the observation of convective gravity waves by a limb-sounding instrument like SABER. For this reason, global maps of absolute momentum flux<sup>7</sup> are compared from simulation (see Figure 5.17) and observation by SABER (see Figure 5.18). Both Figures show January 2008 conditions in the left panels and July conditions in the right panels for altitudes from 25km to 45km with a 5km stepping. The simulated structures with observational filter of Figure 5.17) are in good

---

<sup>7</sup>The gravity wave estimation from SABER temperature variances does not allow the retrieval of the horizontal wavevector. Therefore, only absolute horizontal wavelengths can be estimated and used to calculate the absolute momentum flux according to *Ern et al.* [2004]. For better comparison, the ray-tracing data are also analyzed with respect to absolute values.

### 5.3. SIMULATED CONVECTIVE GRAVITY WAVES IN COMPARISON TO SATELLITE MEASUREMENTS

agreement with the results of Figure 5.15. The convective source is strongest above the continents and lowest west of south America, Africa and Australia due to shallow clouds in this region. Despite the lower general momentum flux in Figure 5.17, the altitude dependence is much weaker compared to Figure 5.15.

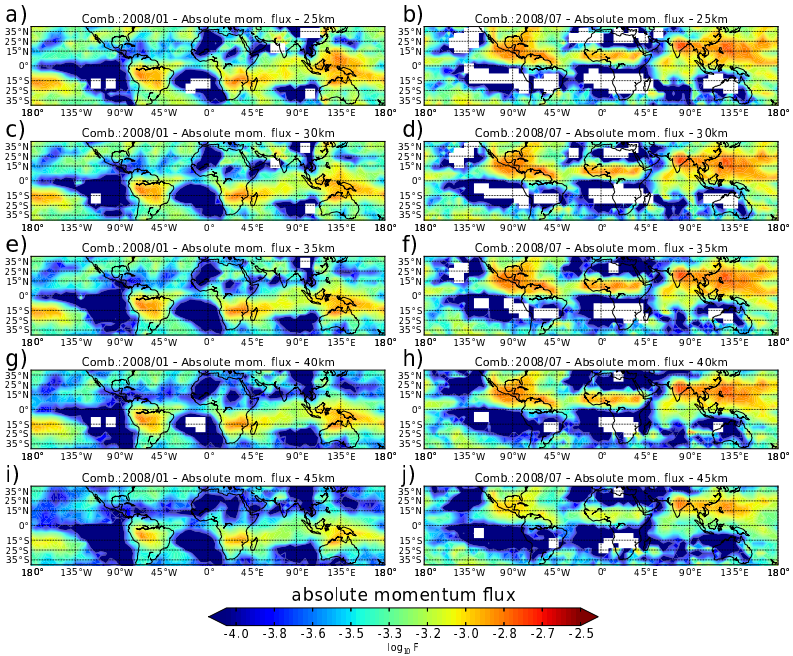


Figure 5.17.: Calculated momentum flux after ray-tracing and application of the visibility filter for January 2008 (left panels) and July 2008 (right panels). The decline of momentum flux with altitude is only very weak - an indication that waves are not saturated at altitudes up to 40km.

## CHAPTER 5. RAY-TRACING SIMULATIONS OF CONVECTIVE GRAVITY WAVES

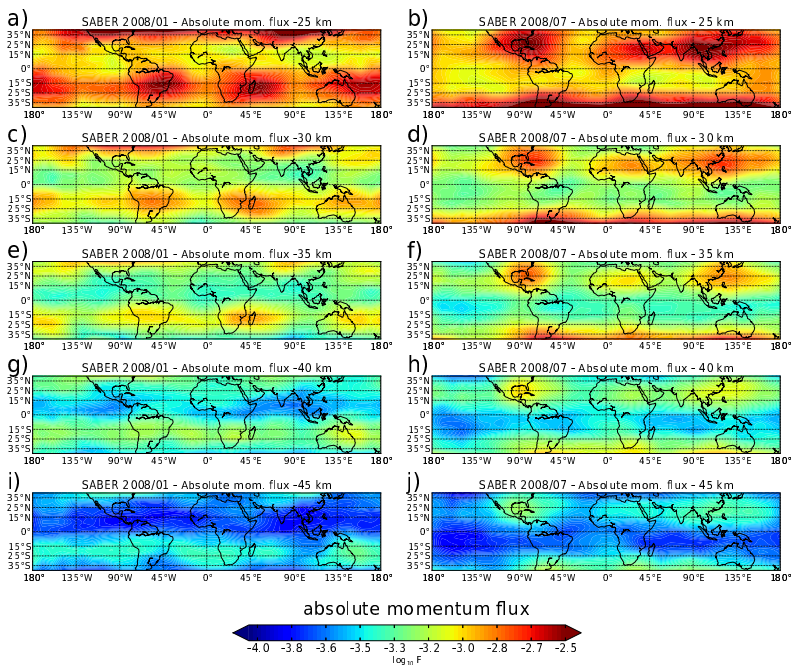


Figure 5.18.: Gravity wave momentum flux derived from the SABER satellite instrument for January 2008 (left panels) and July 2008 (right panels) (courtesy Manfred Ern).

Waves potentially visible to SABER propagate almost conservatively up to the middle stratosphere. Also, the decline of momentum flux with altitude is reduced in the ray-tracing results compared to SABER observations. An indication that the amplitude saturation limit was still not reached for most of the simulated waves at altitudes lower than 45km. The SABER observations on the other hand

### 5.3. SIMULATED CONVECTIVE GRAVITY WAVES IN COMPARISON TO SATELLITE MEASUREMENTS

---

show strong dissipation with altitude (Figure 5.18). It is noteworthy that these observational results include waves from other sources besides convective gravity waves. Especially the 25km altitude may show contributions from other sources, which are already filtered out at 30km altitude. Also, SABER radiances may include some noise as a result from cloud contamination at those low altitudes [Ern *et al.*, 2011]. Another effect is the vertical wavelength filtering in observations induced by a change in the horizontal wavevector. Figure 5.16 shows that for short horizontal wavelengths only very short vertical wavelengths are visible to the instrument. This also depends on the alignment of the horizontal wavevector to the viewing direction of the instrument. A change in the orientation of the horizontal wavevector therefore changes the visibility of waves with very short vertical wavelength. However, values of the simulated convective gravity waves and the SABER observations match well in the order of magnitude.

## CHAPTER 5. RAY-TRACING SIMULATIONS OF CONVECTIVE GRAVITY WAVES

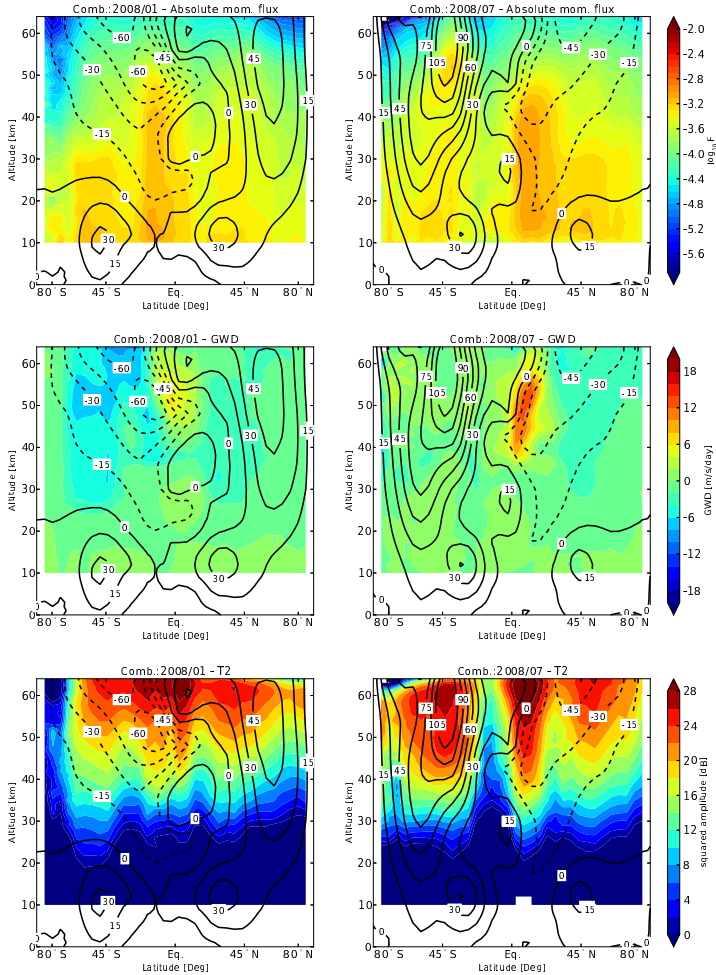


Figure 5.19.: Combined zonal averages of momentum flux (upper row), acceleration (middle row), and temperature amplitude (lower row) with visibility filter. Please note that intermittency with other gravity waves sources was not taken into account. Thus, simulated amplitudes are upper limits.

### 5.3. SIMULATED CONVECTIVE GRAVITY WAVES IN COMPARISON TO SATELLITE MEASUREMENTS

---

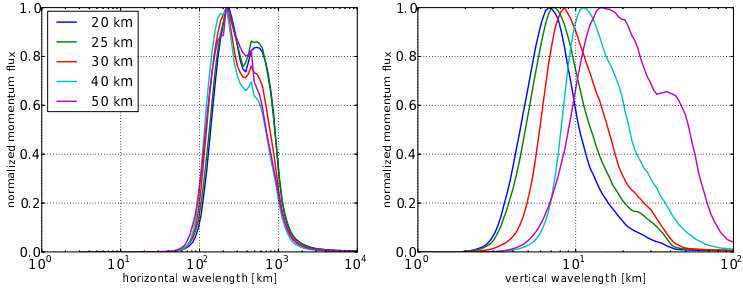


Figure 5.20.: Distributions of gravity wave momentum flux (normalized) by altitude for all three source setups combined and visibility filtered. Left panel shows momentum flux as distribution of the horizontal wavelength. The right panel shows momentum flux as function of the vertical wavelength.

Another feature found is the seasonal cycle of the SABER results with the south to north shift of the continental momentum flux maximums between January and July conditions. The Asian Monsoon region is one of the strongest peaks at 25km altitude and can be also found in the simulation. However, gravity waves from the Asian Monsoon region are somewhat over pronounced in the simulation and distributed over large areas of the Pacific Ocean. This feature is maintained throughout the vertical propagation of the waves and is therefore also found at 45km altitude. SABER results show much lower momentum flux values for this altitude. The zonal averages (upper column of Figure 5.19) show indeed an increased momentum flux at 10°N/S at altitudes as high as 50km in January and 45km in July. At this altitudes gravity wave wind filtering becomes more

## CHAPTER 5. RAY-TRACING SIMULATIONS OF CONVECTIVE GRAVITY WAVES

---

prominent and might be responsible for the decrease in momentum flux at these altitudes. This implies that the remaining gravity waves (after application of an observational filter) are faster waves, thus, can propagate to the upper stratosphere / lower mesosphere region. Consequently, the gravity wave drag is lower with maxima still concentrated within tropical regions. The largest differences to the non-filtered run can be obtained in the temperature amplitudes (lower row). The maximum amplitudes (up to 28 dB) are obtained above the zero-crossing of the background wind (altitudes of 55km and above) with comparable low amplitudes above the background wind reversal ( $<12$  dB). The extra-tropical temperature amplitudes are increased compared to Figure 5.13.

Figure 5.20 shows the combined gravity wave momentum flux distribution with respect to horizontal wavelength (panel a) and vertical wavelength (panel b) of all three source parametrizations and the observational filter applied. The majority of waves is now found between 100km and 1000km horizontal wavelength. The vertical wavelength shifts to longer wavelengths with altitude due to dissipation of waves of shorter vertical wavelength during the upward propagation.

### 5.3.3. Comparison of global ray-tracing and satellite data

In the last sections, convective gravity wave momentum flux, temperature amplitudes, and drag are directly compared to SABER measurements. Even though, encouraging results were found for low latitude regions, modelling of higher latitudes is also needed for a comparison on a global scale. For that purpose, waves from the *Preusse et al.* [2009] non-orographic gravity waves launch distribution was added to the convective gravity waves. This combination of both launch distributions was done by a weighted average:

$$F = \frac{1}{N_{NOLD} + N_{CGW}} \left( \sum_{i=1}^{N_{NOLD}} F_{NOLD} + \sum_{i=1}^{N_{CGW}} F_{CGW} \right) \quad (5.9)$$

$F$  is the overall momentum flux of the combined model.  $F_{NOLD}$  and  $F_{CGW}$  are momentum flux values for the non-orographic launch distribution (NOLD) and the convective gravity waves (CGW).  $N_{NOLD}$  and  $N_{CGW}$  denote the number of each kind of waves within one spatial bin. The NOLD waves spectrum also represents waves from convective sources<sup>8</sup>. Those waves have to be neglected in the combination of NOLD and CGW waves. In order to model convective waves only once, a weighting factor of ten between the two kinds

---

<sup>8</sup>The non-orographic launch distribution includes a broad spectrum of waves which may be excited from sources like convection, fronts or jet-imbalance. The location of each launch is homogeneous distributed, thus, the real source location is not resolved and the final momentum flux distribution depends strongly on wind filtering.

## CHAPTER 5. RAY-TRACING SIMULATIONS OF CONVECTIVE GRAVITY WAVES

---

waves was introduced. Due to this factor, CGW dominates low latitude regions and reduce the momentum flux per bin in high latitude regions.

Figure 5.21 shows the resulting momentum flux distribution for the ray-tracing of both launch distributions (color) and SABER satellite data (contour) for a direct comparison for January 2008 (upper panels) and July 2008 (lower panels). The left panels show results for 30km altitude and the right panels show results for 50km altitude. Figure 5.21 shows a better agreement with SABER observational data in terms of location of local maxima / minima of momentum flux and its absolute value. The momentum flux between 30°S and 30°N is dominated by the ray-tracing calculation of convective gravity waves from all three convective source setups combined including the visibility filter.

In contrast, momentum flux values at higher latitudes originate mainly from the non-orographic gravity wave launch distribution after *Preusse et al.* [2009]. In particular, the tropical peaks above the continents are better resolved. The south American momentum flux maximum is found above the Amazonian rain forest in the simulation and in observational data for January conditions. The peak over Madagascar as seen in the SABER data spans from south Africa to the Indian ocean. Also, the high momentum fluxes above Indochina found in the observations are well represented in the simulation. Further, localized minima with momentum flux values lower than in the observations of Figure 3.2 appear in the tropics of the winter hemisphere. Comparing SABER measurements and gravity

### 5.3. SIMULATED CONVECTIVE GRAVITY WAVES IN COMPARISON TO SATELLITE MEASUREMENTS

---

wave simulations for 50km altitude, the general latitudinal structures are in good agreement. But unlike to the observations, the momentum flux peaks in the simulations are not poleward shifted at 50km altitude. The tropical peaks are shifted to the northern hemisphere during July. Maxima in momentum flux are again in good agreement to the observation in position and value. Since both source parametrizations do not include any orographic gravity waves, the typical momentum flux maximum at the Drake Passage is not represented in the simulation. Despite these typical mountain wave regions (mountain wave are not covered by this combined gravity wave ray-tracing model), the overall agreement in structure and absolute values between observation and simulation is encouraging. The only remaining difference is that the poleward shift of momentum flux with altitude is not represented in the model data as it is observed from SABER.

CHAPTER 5. RAY-TRACING SIMULATIONS OF CONVECTIVE GRAVITY WAVES

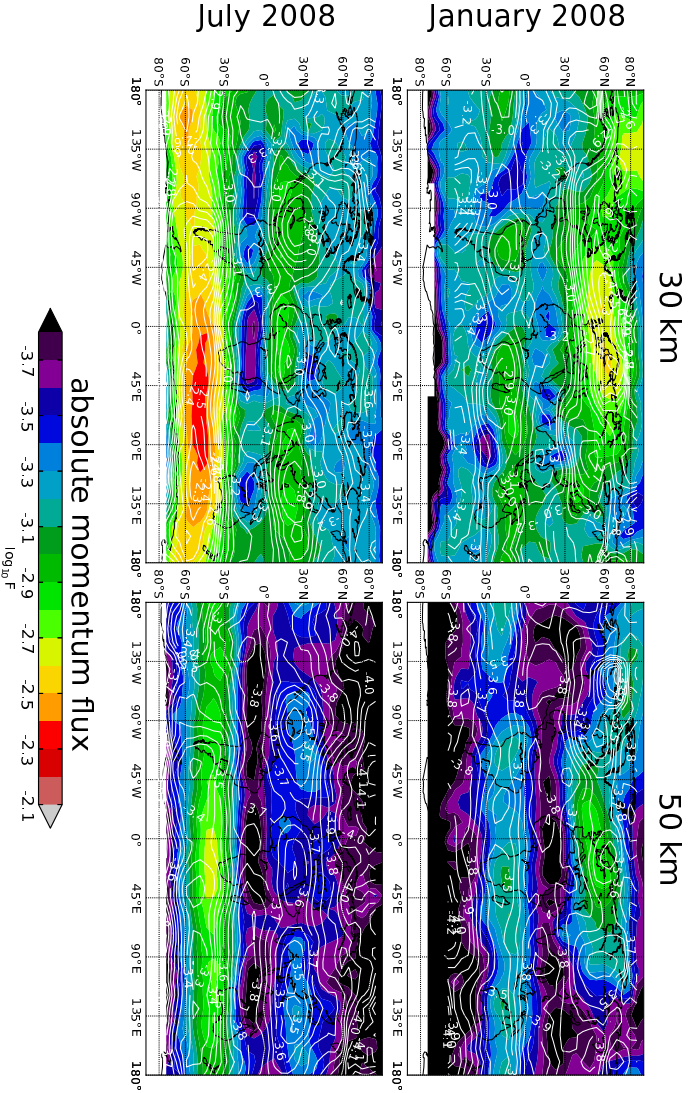


Figure 5.21.: Combination of MF1-MF3 parameter setups with visibility filter (gravity waves shorter than 100km have been filtered out). A non-orographic background parametrization after *Preusse et al.* [2009] was added for better comparison with SABER satellite measurements (white contour lines).

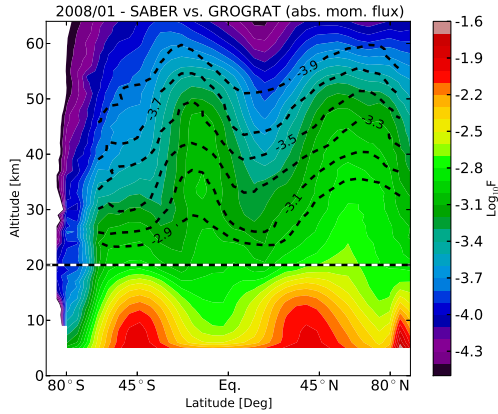
### 5.3. SIMULATED CONVECTIVE GRAVITY WAVES IN COMPARISON TO SATELLITE MEASUREMENTS

---

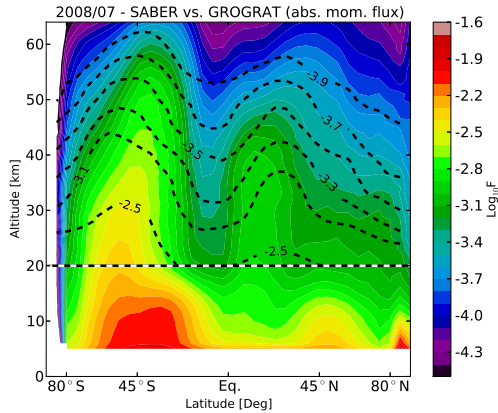
Figures 5.22a and 5.22b show the zonal mean momentum flux of the combined convective and non-orographic parametrization in color. SABER measurements of momentum flux are indicated as contour lines starting at 20km altitude. In the troposphere maxima are found at approximately  $45^{\circ}$ N/S with a rather steep decay rate. Momentum flux already decreased about one order of magnitude at 20km altitude. In the stratosphere the northern hemisphere (winter) maximum in momentum flux is found between  $45^{\circ}$ N and  $80^{\circ}$ N with logarithmic momentum flux values of about  $-2.8$  (1.6mPa) at 20km to  $-3.3$  (0.5mPa) at 50km altitude. This is in terms of both structure and value in very good agreement with the SABER data (error margin of SABER is about 0.3 orders of magnitude). The southern hemisphere (summer) peak is found around  $15^{\circ}$ S in the stratosphere for the ray-tracing calculations and appears to be northward shifted by more than  $5^{\circ}$  compared to SABER measurements. Still, the vertical decay in momentum flux is found somewhat consistent with the decay of the observed gravity wave momentum flux. The southward tilt of momentum flux found between 50km and 60km is less prominent compared to the tilt observed by SABER. Gravity waves from the convective source which propagate predominantly within low latitudes (see Figure 5.14) might not explain the tilting obtained in Figures 5.22a and 5.22b. Instead, the non-orographic waves dominate the momentum flux distribution and induce the obtained tilting.

## CHAPTER 5. RAY-TRACING SIMULATIONS OF CONVECTIVE GRAVITY WAVES

---



(a) January 2008



(b) July 2008

Figure 5.22.: Momentum flux zonal averages of the combined simulation MF1-3 with visibility filter (color) and the *Preusse et al.* [2009] gravity wave parametrization as background. SABER measurements are indicated as contour lines. Error margin of SABER is about 0.3 orders of magnitude of momentum flux.

### 5.3. SIMULATED CONVECTIVE GRAVITY WAVES IN COMPARISON TO SATELLITE MEASUREMENTS

---

Further investigation on different gravity wave sources (e.g. jet imbalance) is needed to explain the physical source of this mid-latitude waves which produce the strong tilting found in the measurements. Convective gravity waves are a minor contributor in this case. The situation is slightly different for July. In the southern hemisphere where tropospheric wind jet direction and the stratospheric winds are both eastward directed. As a result, waves with a westward component of the wave vector encounter favourable propagation conditions and can propagate to higher altitudes, while eastward propagating waves are strongly damped or even filtered. In the absolute momentum fluxes, the effect of favourable propagation conditions for westward propagating waves dominates and a strong maximum forms up. Momentum flux values from ray-tracing and SABER data show enhanced values at  $45^{\circ}\text{S}$  from the troposphere up to the mesosphere. The secondary peak is found at  $25^{\circ}\text{N}$  in the ray-tracing calculations and at  $30^{\circ}\text{N}$  for the measurements. The same shift in the tropical peak was already found in Figure 5.21 for July. However, the momentum flux distribution over Africa indicates that neither convection nor the general background parametrization are suitable to explain this differences (SABER shows higher momentum fluxes above the Sahara desert, ray-tracing of convective waves originate from the Sahel zone). A similar, but less pronounced equatorward bias of the modeled subtropical maximum was also observed for January data in Figure 5.22a. Considering the global maps in Figure 5.21, the regions where this shifts occur can be identified as the continental maxima. The most pronounced maximum is found in

North America with a remarkable shift of more than  $5^\circ$  southward for January data.

## 5.4. Summary and Outlook

The aim of this chapter is to improve the understanding of convective gravity waves by performing calculations with the GROGRAT gravity wave ray-tracer and the Yonsei convective gravity wave source model. For this purpose, both models have been coupled. The convective gravity wave source showed a typical seasonal behavior in terms of a hemispheric shift in momentum flux at cloud top height following the ITCZ. After performing the ray-tracing simulations from source level, this seasonal shift was, as expected, also found at higher altitudes. The dependence of momentum flux distributions, gravity wave drag, and temperature amplitudes on two free tunable parameters, the horizontal scale  $\delta_x$  and the temporal scale  $\delta_t$ , have been investigated. Three different setups of these parameters have been chosen. MF1 and MF2 from *Choi et al.* [2012] account for small and middle scale convective cells. The new setup MF3 also accounts for large-scale convective clusters (e.g. in the Asian Monsoon). A ray-tracing simulation combined of all three source setups showed already remarkable good agreement with SABER satellite measurements. Local features, like peaks in gravity wave momentum flux above the continents, are in good agreement with the measurements at low latitudes. This agreement could be further improved by introducing the observational filter to account for the limitations of limb-

#### 5.4. SUMMARY AND OUTLOOK

---

sounding satellites in observing waves of short horizontal wavelength. The resulting global distributions of gravity wave momentum flux, constrained by observations, reproduce, apart from the influence of orographic sources, all major features in the relative distribution as well as in magnitude.



## 6. Summary and Outlook

In this thesis the forcing and propagation of gravity waves was investigated using the well-proven method of ray-tracing and different types of launch distributions. Four urgent questions are addressed concerning the generation of gravity waves at tropospheric sources, their propagation through the middle atmosphere, and their dissipation. Global distributions from these numerical simulations have been compared to satellite observations to judge the quality of the modelling. Measurement uncertainties are as high as a factor of 2-3 and simulations have, of course, also a limited precision. However, the combination of measurements and modelling can answer the questions from the introduction of this thesis.

**Can gravity wave ray-tracing with a homogeneous and isotropic source resemble major features in the gravity wave momentum flux distribution as observed by satellite instruments?**

To answer this question, the GROGRAT gravity wave ray-tracing model was used with a homogeneous and isotropic launch distribu-

tion. Phase-speeds and amplitudes at launch level were taken from comparisons with satellite measurements by *Preusse et al.* [2009]. In analogy to a non-orographic gravity wave parametrization for global models this is also called non-orographic launch distribution. The results of these simulation were compared to infrared limb-sounder measurements by SABER and showed a good overall agreement in the latitudinal and vertical structure of the momentum flux distribution. Still, the longitudinal structure of momentum flux due to physical sources is not well represented. Also, simulated momentum flux values show in general a high bias. However, the seasonal differences found by gravity wave ray-tracing agree very well with observations. These encouraging results motivate further investigations using the GROGRAT ray-tracing model with a non-orographic launch distribution to answer the remaining questions of this thesis. The GROGRAT ray-tracing model is also able to restrict the trajectory calculation to vertical-only propagation. Therefore, it is a useful tool to answer the second question:

**How does the vertical-only assumption of gravity wave propagation affect the patterns of gravity wave accelerations in the middle atmosphere?**

This question was first asked by *Lindzen* [1981] and was not answered yet. However, the vertical-only propagation assumption is used in gravity wave parametrizations of atmospheric circulation models today. In order to answer that question, two ray-tracing sim-

---

ulations have been performed. One with vertical-only propagation of gravity waves and the second one with a free three-dimensional propagation of gravity waves<sup>1</sup>. The restriction to vertical propagation alters the global distributions of both the zonal drag and the meridional drag. For zonal drag the following major patterns were found: The gravity wave drag of the oblique propagation case is enhanced in the summer stratopause and mesosphere region. But, it is reduced in the tropics above the middle stratosphere (30-40km). Also the drag maximum at the top of the winter polar jet is poleward shifted. In addition, some minor local structures caused by local wind filtering in the UTLS are smoothed out. The influence on meridional drag is much stronger and alters the overall distribution. Higher meridional drag is exerted at locations similar to those where higher zonal drag was found and was found to be generally poleward directed. In the vertical-only propagation case a relatively weak drag is found opposed to the summer pole to winter pole circulation in the upper mesosphere. As a first order effect, the meridional drag and zonal drag occur at the same position. Therefore, it is self-evident to suggest an easy-to-implement test to GCM modellers: the meridional drag can be kept proportional to the absolute zonal drag, scaled, and adjusted for hemisphere:

$$Y_N = Y + \alpha \cdot \Gamma \cdot |X| \quad (6.1)$$

with X representing the zonal drag component calculated by a

---

<sup>1</sup>The results of this study can also be found in *Kalisch et al.* [2014]

common gravity wave parametrization,  $Y$  the meridional drag component,  $\alpha$  as a positive scaling factor varying with altitude and  $\Gamma$  as a hemispheric function ( $\Gamma = -1$  for SH;  $\Gamma = 1$  for NH). The latter ensures the poleward direction of the new adjusted meridional drag  $Y_N$ . The meridional acceleration may directly affect the residual circulation, but also changes the interaction of gravity waves and planetary waves. Thus, a first assessment of some of the effects of oblique wave propagation could be considered without actually including a ray-tracing parametrization into a GCM.

The latitudinal structure of momentum flux distributions are already well represented by a homogeneous launch distribution. However, localized and time-varying features, in which gravity wave momentum flux may be enhanced by factors, remain unreflected. For instance, the enhancement by convective gravity wave sources in the Monsoon regions is about one order of magnitude. By homogeneous sources, gravity wave momentum flux in the subtropics is overestimated in regions without specific sources and underestimated in regions of strong convection, resulting in a contrast of only half an order of magnitude. In addition, the tuning of unphysical sources cannot take into account climate feedbacks. Physical sources of gravity waves like convection are highly dynamic, localized, and also force gravity waves with very short horizontal wavelengths which are hard to observe on a global scale. Yet, a first step towards further understanding of the impact of convective gravity waves on a global scale leads to the following question:

---

**How does a convective gravity wave source model alter the global distributions of gravity wave momentum flux compared to a uniform gravity wave source?**

Chapter 5 answers this question. A convective gravity wave source model was coupled to the GROGRAT ray-tracer. The calculations involve tuning of free parameters and were compared to satellite observations of convective regions.

Gravity waves have been modelled including their tropospheric forcing mechanism and propagation into the mesosphere. Three different setups of the convective gravity wave source model were used to account for small-scale single convective cells as well as for convective clusters (e.g. in the Asian Monsoon) or large-scale convection. It has been shown that the launch distribution of convective gravity waves correlates with precipitation patterns and that wind filtering during the upward propagation of waves alters the global momentum flux distribution. Accordingly, the momentum flux distributions are in good agreement to global observations of gravity wave momentum flux. Further, the momentum flux distribution in the tropics and subtropics could be significantly improved. Momentum flux is enhanced in the summer hemisphere and in particular above the continents. During northern summer this is the Indian summer monsoon and the region around Florida for the southern summer. For a quantitative comparison also limitations of infrared limb-sounding of gravity wave signatures need to be taken into account. One of these limitations concerns the shortest horizontal wavelengths ob-

servable by a limb-sounding satellite instrument. This particular limitation was also taken into account when comparing simulations and observations and the following question could be answered:

**How does the observational filter of infrared limb-sounding satellite instruments affect global momentum flux distributions and which part of the convective gravity wave spectrum is visible to satellite instruments?**

The results presented in chapter 5 show that convective gravity waves can have very short horizontal wavelengths of the order of  $\approx 10$ km. Infrared limb-sounding of optically thin emissions is generally limited to the observation of gravity waves with horizontal wavelengths of the order of 100km or longer.

The gravity wave source model used for this study accounts for excitation processes on different spatial and temporal scales. Small and larger convective cells as well as convective clusters are represented by three different setups of the source parametrization (MF1, MF2, and MF3). MF1 accounts for small-scale convection and its associated gravity waves are not visible to the SABER limb-sounding instrument. MF2 gravity waves are partially visible and MF3 waves are almost entirely visible to the instrument. Chapter 5 showed that a combination of all three setups MF1, MF2, and MF3 including the observational filter and a non-orographic background parametrization for the representation of high latitude momentum flux agrees well with observations. However, the spatial and temporal charac-

---

teristics of the convective gravity wave source does not address the relative contribution of these scales to the momentum flux distributions. Further research is needed to quantify the relative forcing strength associated with each source setup. Also, the observational filter itself is the focus of another on-going study [*Trinh et al., 2014*] which addresses the limitations of infrared limb-sounding satellite instruments with respect to the detection of gravity waves in more detail.

The relative contribution of short horizontal scale gravity waves still remains uncertain. Additional measurements using different observational methods (e.g. balloon measurements) are needed for a more sophisticated characterization of the horizontal wavelength spectrum of convective gravity waves particularly in the short horizontal wavelength part of the spectrum. First attempts for this task have already been made [*Jewtoukoff et al., 2013*], but still available datasets on convective gravity waves remain sparse. There are three possible options to address this problem.

Firstly, satellites with a higher visibility in the short horizontal wavelength (as short as 50km) regime would be able to detect complementary parts of the convective gravity wave spectrum with a global coverage. Observations performed with e.g. the GLORIA<sup>2</sup> limb-sounding infrared imager would offer more insights for urgent questions about, for instance, the contribution of gravity waves to the semiannual-oscillation (SAO). However, the very short horizon-

---

<sup>2</sup>Gimballed Limb Observer for Radiance Imaging of the Atmosphere (GLORIA) [*Friedl-Vallon et al., 2014, Riese et al., 2014*]

tal wavelength part with waves as short as a few kilometers would still remain uncertain.

Secondly, a larger scale campaign (Stratéole campaign already planned for 2018/2019) using super-pressure balloons for altitudes up to 18km would support measurements in the horizontal wavelength range of a few kilometers. As a result, the relative contribution of small convective cells represented by the MF1 setup of the convective source model in this thesis can be estimated. Also, the importance of oblique gravity wave propagation on balloon measurements was already discussed in *Jewtoukoff et al.* [2013]. Results from chapter 4 of this thesis and *Kalisch et al.* [2014] may help to quantify the effect of horizontal propagation of gravity waves in those measurements. However, the disadvantage of super-pressure balloons is, of course, the low spatial coverage. In addition, these measurements are limited to altitudes less than 18km. Many ducted gravity waves may exist between the thermal tropopause and the wind shear above of it. Therefore, these observations cannot replace truly-stratospheric measurements.

Thirdly, the extrapolation of the visible gravity wave horizontal wavelength spectrum towards shorter wavelengths using estimates of the missing gravity wave drag (e.g. in tropics) for comparison with simulations and other observations. This technique could be applied without the costly development of new instruments using model input to constantly re-evaluate its results. First attempts in this direction have already been made in *Ern et al.* [2014]. However, a model based extrapolation of measurements is not able to

---

substitute for real measurements.

None of these three approaches on its own is likely to reliably solve this question, but the combination of all three attempts together will cancel out some of the disadvantages of each method and will help to solve the puzzle of the horizontal wavelengths of convective gravity waves.



# A. Appendices

## A.1. Wind filtering of gravity waves

In the main part of this thesis the wind-filtering mechanism (also known as *critical level filtering*) is used to explain the change in the sign of momentum flux during the upward propagation within a wind reversal. Also the higher amounts of gravity wave drag found at regions with gradients in wind can be explained by this mechanism. The explanation here will follow the results from *Booker and Bretherton* [1967]. In this publication, the vertical wavenumber  $m$  at a critical level was derived as:

$$m = \pm \frac{N}{(c_{ph} - u)} \quad (\text{A.1})$$

with  $N$  as the buoyancy frequency,  $c_{ph}$  as the (horizontal) phase-speed of the wave and  $u$  as the background wind speed. As soon as the background wind speed approaches  $c_{ph}$ , the vertical wavenumber  $m$  becomes infinity. The vertical wavelength ( $\lambda_z = 2\pi/m$ ) then approaches zero. In other words, the wave cannot exist at the exact location of the critical level and therefore releases its momentum to

the background flow. This implies a higher gravity wave drag at that location.

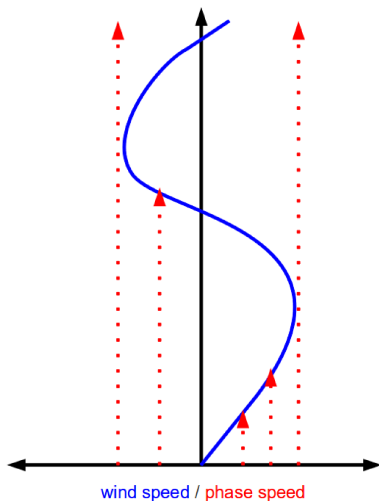


Figure A.1.: Schematic depiction of the wind-filtering mechanism of gravity waves (red dotted lines). Waves with different phase-speed (x-axis) propagate upward until their phase-speed matches the background wind speed (blue line).

Figure A.1 shows the case of a wind reversal (blue line) with gravity waves (red dotted lines) of certain phase-speeds launched at a lower altitude. Gravity waves are filtered during their upward propagation with respect to their phase-speed. Waves with phase-speeds faster than the background wind speed are not filtered, hence, propagate to even higher altitudes.

## A.2. Timeseries of convective gravity waves

In the main part of this thesis, the convective gravity wave source model was used to explain global momentum flux and gravity wave drag distributions for two representative months (January and July). The whole annual cycle of convective gravity waves, though, is another important topic. Because convection is the dominant source in the tropics, the interaction with typical tropical winds (e.g. QBO winds) are particularly interesting. For this reason, the MF1 parameter setup of the convective gravity wave source scheme has been used for a timeseries run from 2002-2009 using Merra data for the atmospheric background and the latent heat data.

Figure A.2 shows the average zonal momentum flux within a  $10^{\circ}\text{S}$ - $10^{\circ}\text{N}$  latitude bin denoted in color. The contour lines indicate the wind direction. The black lines show the zero-crossing of the wind field. Red lines indicate for positive zonal winds (eastward directed winds) of  $10\text{m/s}$  and blue lines indicate negative zonal winds (westward directed winds) of  $-10\text{m/s}$ . The background wind shows a bias of winds in westward direction. Eastward directed winds (red lines) exceed  $10\text{m/s}$  only for a short period of time at certain altitudes. The momentum flux, however, is generally anti-correlated to the background wind. Positive (eastward) momentum flux values match well the negative (westward) directed zonal wind. A simple explanation for this observation is the wind-filtering mechanism from chapter A.1. Starting from low altitudes, gravity waves with, for instance, eastward propagation direction are filtered out in an

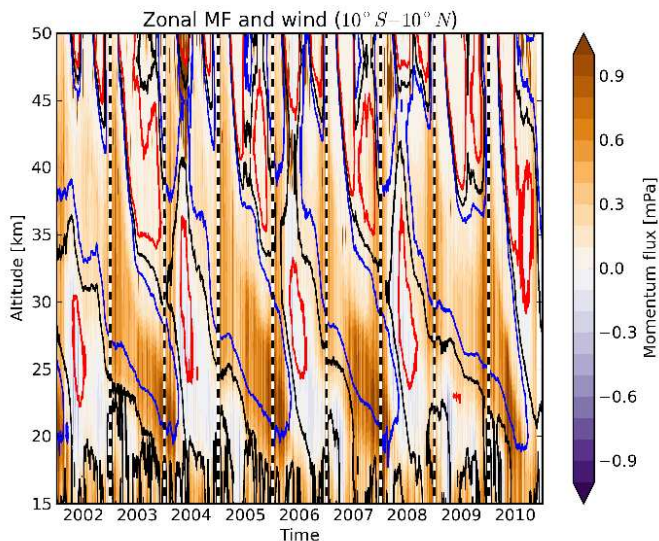


Figure A.2.: Gravity wave zonal momentum flux (color) and zonal background wind (contour) for  $10^{\circ}\text{S}$ - $10^{\circ}\text{N}$  latitudes. Red contour lines indicate 10m/s zonal wind and blue contour lines indicate -10m/s zonal wind. The black line indicates the zero-crossing to distinguish the different QBO phases. Gravity wave momentum flux shows strong anti-correlation with the background wind as discussed in the text.

eastward directed background wind. The remaining waves are almost westward directed and produce the observed anti-correlation with the background wind. Further, the remaining momentum flux is found to be very low at higher altitudes in particular when the

## A.2. TIMESERIES OF CONVECTIVE GRAVITY WAVES

---

background wind encounters a full reversal in horizontal direction. In this case, the filtering of gravity waves by the background wind acts in both directions and decreases the overall momentum flux. This can be found, for instance, for the winter of 2007. During that particular time, the zonal wind at altitudes around 20km is westward directed. The wind reversal occurs at 35km altitude and again at 47km altitude. The momentum flux found at that altitude is already decreased to values lower than 0.1mPa. As a result of the anti-correlation of momentum flux and background wind, a quasi-biennial-cycle of zonal gravity wave momentum flux can be obtained from Figure A.1 at altitudes between 25km and 40km. Well, this quasi-biennial-cycle is obtained for the tropics. Extra-tropic latitudes, however, show a very different annual cycle in momentum flux.

Figure A.3 shows the average absolute momentum flux at 15°N-25°N (upper panel) and 15°S-25°S (lower panel), both at 30km altitude. Maxima in momentum flux are found during the summer time of each hemisphere, thus, in June/July/August for the northern hemisphere and December/January/February for the southern hemisphere. It was already shown in *Ern et al.* [2011] that this annual cycle is indeed found in observation of momentum flux from satellite instruments.

Figure A.4 shows the whole latitude range of absolute momentum flux (upper panel), zonal momentum flux (middle panel), and meridional momentum flux (lower panel). The quasi-biennial-cycle in absolute momentum flux is hard to obtain from this figure. How-

## Timeseries of gravity wave momentum flux

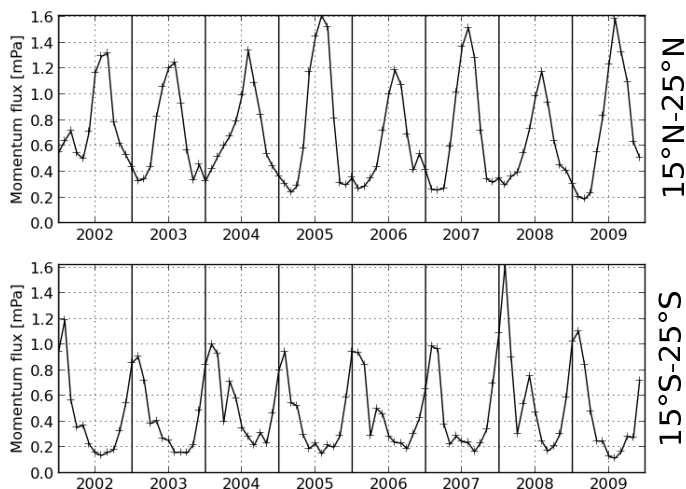


Figure A.3.: Average absolute momentum flux at  $15^{\circ}\text{N}$ - $25^{\circ}\text{N}$  (upper panel) and  $15^{\circ}\text{S}$ - $25^{\circ}\text{S}$  (lower panel) at 30km altitude. Both hemispheres show a annual cycle in the momentum flux.

ever, the extra-tropical annual cycle is more obvious. Additionally, high momentum flux values are found for the southern hemisphere winter time. It is also remarkable that the (extra-)tropical zonal momentum flux (middle panel) is predominantly eastward directed. In contrast, the higher latitude momentum flux, in particular for the southern hemisphere, are westward directed. The latter can be again understood with respect to the wind-filtering mechanism from

## A.2. TIMESERIES OF CONVECTIVE GRAVITY WAVES

---

chapter A.1. The strong west wind (eastward directed) regime of the southern hemisphere filters larger parts of the eastward propagating gravity waves. The remaining gravity waves show a westward bias. The meridional momentum flux component shows another interesting feature. In contrast to the findings for the homogeneous isotropic launch distribution from chapter 4, the meridional momentum flux appears to be almost only northward directed. Further research is needed to explain this finding and its possible impacts on the meridional circulation.

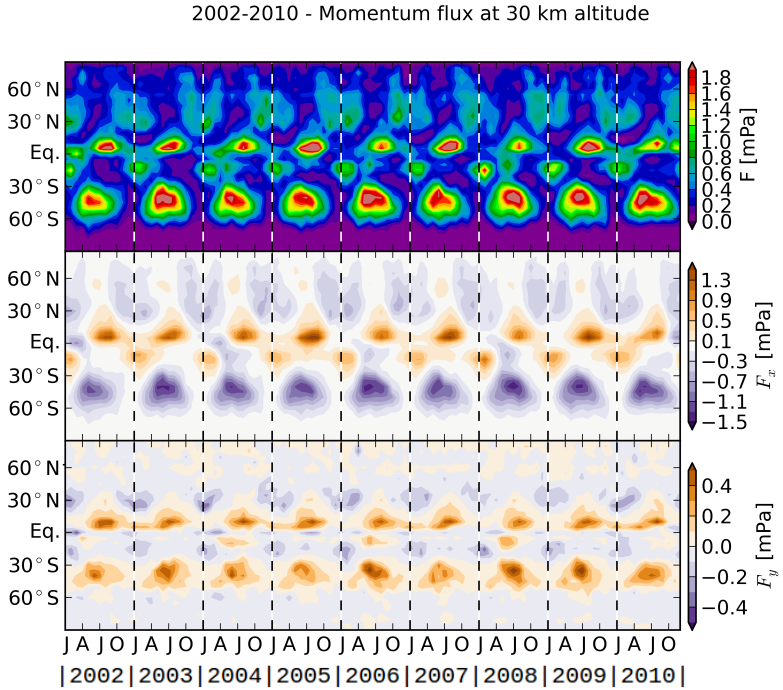


Figure A.4.: The whole latitude range of absolute momentum flux (upper panel), zonal momentum flux (middle panel), and meridional momentum flux (lower panel) at 30km altitude. For discussion refer to text.

## A.3. Gravity wave ray-tracing as a parametrization for atmospheric circulation models

### A.3.1. Overview of the HAMMONIA GCM

The Hamburg Model for the Neutral and Ionized Atmosphere (HAMMONIA) was originally designed to investigate coupling mechanisms between different atmospheric regions and their response to external perturbations (e.g. solar variability, anthropogenic chemical emissions) [Schmidt *et al.*, 2008]. The HAMMONIA model is the vertical extension of the MAECHAM5 model up to the thermosphere [Giorgetta *et al.*, 2006, Manzini *et al.*, 2006]. MAECHAM5 itself is the middle atmosphere extension of the ECHAM5 atmospheric general circulation model [Roeckner *et al.*, 2003]. Many technical details like the spectral representation of the background atmosphere evolved from this long history of model development on the ECHAM models. Typically HAMMONIA uses a triangular truncation at wavenumber 31 (T31) in the horizontal and 67 vertical levels up to 250km represented as hybrid<sup>1</sup> coordinates. Orographic gravity waves are parametrized by the *Lott and Miller* [1997] scheme like in the ECHAM5 model. The non-orographic gravity wave momentum flux deposition is calculated using the Hines parametrization [Hines,

---

<sup>1</sup>Hybrid vertical coordinates are a common optimization to keep the vertical grid almost parallel to the topography at lower altitudes and parallel to pressure-based vertical coordinates at higher altitudes.

1997] with an additional tropospheric frontal source parametrization [Charron and Manzini, 2002]. The vertical cutoff wavenumber was set to  $2\pi/(12km)$  to maintain realistic mesospheric winds and temperatures. The Hines scheme assumes vertical only propagation of gravity waves and is not able to resemble many of the findings made in chapter 4.

### **A.3.2. Technical implementation**

The implementation of a free three-dimensional trajectory calculation into an existing highly parallelized atmospheric model implies some technical challenges which are briefly introduced in this section. First of all, HAMMONIA like the most atmospheric models, uses a spatial domain subdivision to distribute the overall workload over a larger amount of processors. Since single regions within the atmosphere are not isolated from each other, the atmospheric state has to be distributed to neighbouring regions. This involves some communication on the cluster computer network and therefore a reduction in computational efficiency. Most of the parametrizations today are designed to work within one vertical column or only need to communicate with neighbour columns to reduce the communication effort. The ray-tracer on the other hand needs the whole atmospheric state for each processor involved in the ray-tracing calculations. Thus, the complete state of the background atmosphere has to be send to every single processor which implies a larger amount of data to be transmitted at every time step. Another technical problem is the load-balancing of the ray-tracing of each processor. Some gravity

### A.3. GRAVITY WAVE RAY-TRACING AS A PARAMETRIZATION FOR ATMOSPHERIC CIRCULATION MODELS

---

wave calculations are stopped earlier due to full dissipation of waves than others. It follows that the time spent for ray-tracing differs among the processors, if no load-balancing algorithm is applied.

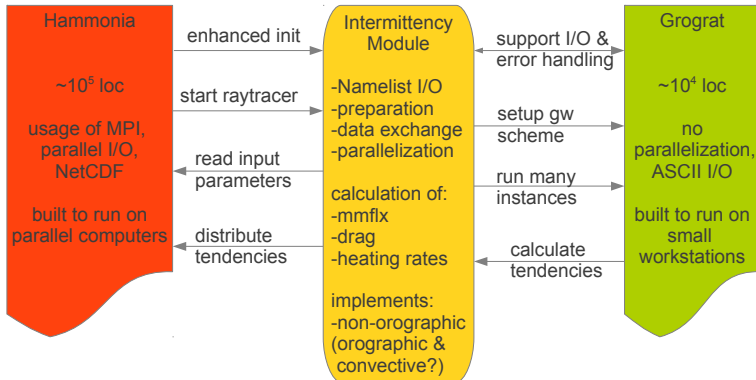


Figure A.5.: Coupling of the HAMMONIA GCM and the GROGRAT gravity wave ray-tracer. The intermittent module (middle box) works as a coupler and hides internal variables of each model. It also re-routes the Input/Output mechanisms of GROGRAT towards HAMMONIA atmospheric state quantities (e.g. wind and temperature). Further, gravity wave launch distributions are generated. Different parallelizations are also implemented for the ray-tracing and its load-balancing throughout the simulation run.

For this reason, a load-balancing mechanism was developed to keep every processor busy with the ray-tracing calculation. This ensures a high scalability of the whole model. Another reason for the implementation of an intermittent module is to only introduce as few changes as needed within the HAMMONIA model. Only a

## APPENDIX A. APPENDICES

---

few interfaces between HAMMONIA and the intermittent module are needed (e.g. initialization, data transmission, and execution of the ray-tracer). Figure A.5 gives a schematic overview of the technical coupling of both models. The red box on the left side represents the HAMMONIA model with its own input/output subsystem, parallelization, the dynamical core, and its parametrizations. Only small changes in the HAMMONIA code had to be done to couple it to the GROGRAT ray-tracer (green box on the right side) via the intermittent module (yellow box in the middle). The latter connects GROGRAT's own input/output system to the data transmitted from HAMMONIA and hides technical details of both models from each other. It further introduces a different global parallelization (domain subdivision) during the ray-tracing simulation only. Although the model is already working, the reliability of this new coupled model has still to be proven. This, of course, is beyond the scope of this thesis and will be a topic of further model studies.

# Acknowledgements

I would like to address my first thanks to Prof. Dr. Martin Riese for trusting me with this interesting research topic and for offering me the opportunity to work at IEK-7. I am very thankful for his helpful comments and discussions on my work and papers to be published.

I am very grateful to Dr. Peter Preuße for his support and scientific as well as non-scientific discussions. His continuous critical questioning combined with many fresh and creative ideas contributed a lot to this work.

I am also much obliged to Dr. Manfred Ern and his great work on gravity wave measurements from satellite instruments. Without his results and expertise, this work would have been infeasible.

I would also like to express my sincere gratitude to all remaining colleagues from the IEK-7 at Forschungszentrum Jülich who are responsible for a very pleasurable working environment. Special thanks go to Tobias Guggenmoser for the refreshing and creative discussions besides our scientific research. I would also like to acknowledge the funding of this work by Deutsche Forschungsgemeinschaft (DFG).



# Bibliography

- Alexander, M. J. (1998), Interpretations of observed climatological patterns in stratospheric gravity wave variance, *J. Geophys. Res.*, *103*, 8627–8640.
- Alexander, M. J., and T. J. Dunkerton (1999), A spectral parameterization of mean-flow forcing due to breaking gravity waves, *J. Atmos. Sci.*, *56*, 4167–4182.
- Alexander, M. J., and K. H. Rosenlof (2003), Gravity-wave forcing in the stratosphere: Observational constraints from the upper atmosphere research satellite and implications for parameterization in global models, *J. Geophys. Res.*, *108*, 4597, doi: 10.1029/2003JD003373.
- Alexander, M. J., T. Tsuda, and R. A. Vincent (2002), On the latitudinal variations observed in gravity waves with short vertical wavelengths, *J. Atmos. Sci.*, *59*, 1394–1404.
- Alexander, M. J., M. Geller, C. McLandress, S. Polavarapu, P. Preusse, F. Sassi, K. Sato, S. D. Eckermann, M. Ern, A. Hertzog, Y. Kawatani, M. Pulido, T. Shaw, M. Sigmund, R. Vincent,

## Bibliography

---

- and S. Watanabe (2010a), Recent developments in gravity wave effects in climate models, and the global distribution of gravity wave momentum flux from observations and models, *Q. J. Roy. Meteorol. Soc.*, *136*, 1103–1124, doi:10.1002/qj.637.
- Alexander, M. J., M. Geller, C. McLandress, S. Polavarapu, P. Preusse, F. Sassi, K. Sato, S. Eckermann, M. Ern, A. Hertzog, Y. Kawatani, M. Pulido, T. A. Shaw, M. Sigmund, R. Vincent, and S. Watanabe (2010b), Recent developments in gravity-wave effects in climate models and the global distribution of gravity-wave momentum flux from observations and models, *Q. J. R. Meteorol. Soc.*, *136*, 1103–1124, doi:{10.1002/qj.637}.
- Andrews, D. G., and M. E. McIntyre (1978), Generalized Eliassen-Palm and Charney-Drazin theorems for waves on axisymmetric mean flows in compressible atmospheres, *J. Atmos. Sci.*, *35*, 175–185.
- Andrews, D. G., J. R. Holton, and C. B. Leovy (1987), *Middle Atmosphere Dynamics, International Geophysics Series*, vol. 40, Academic Press.
- Baker, N. D. (2000), Effects of the sun on the earth’s environment, *J. Atmos. Solar-Terr. Phys.*, *62*, 1669–1681.
- Beres, J. H., M. J. Alexander, and J. R. Holton (2002), Effects of tropospheric wind shear on the spectrum of convectively generated gravity waves, *J. Atmos. Sci.*, *59*, 1905–1824.

- Beres, J. H., M. J. Alexander, and J. R. Holton (2004), A method of specifying the gravity wave spectrum above convection based on latent heating properties and background wind, *J. Atmos. Sci.*, *61*(3), 324–337.
- Beres, J. H., R. R. Garcia, B. A. Boville, and F. Sassi (2005), Implementation of a gravity wave source spectrum parameterization dependent on the properties of convection in the Whole Atmosphere Community Climate Model (WACCM), *J. Geophys. Res.*, *110*(D10108), doi:10.1029/2004JD005504.
- Booker, J. R., and F. P. Bretherton (1967), The critical layer for internal gravity waves in a shear flow, *J. Fluid Mech.*, *27*, 513–519.
- Bosilovich, M. G., F. R. Robertson, and J. Chen (2011), Global energy and water budgets in merra., *Journal of Climate*, *24*(22), 5721 – 5739.
- Bretherton, F. P. (1969), Momentum transport by gravity waves, *Q. J.R. Meteorol. Soc.*, *95*, 213–243.
- Buehler, O., and M. E. McIntyre (2003), Remote recoil: a new wave-mean interaction effect, *J. Fluid Mech.*, *492*, 207–230.
- Butchart, N., I. Cionni, V. Eyering, T. G. Shepherd, D. W. Waugh, H. Akiyoshi, J. Austin, C. Bruehl, M. P. Chipperfield, E. Cordero, M. Dameris, R. Deckert, S. Dhomse, S. M. Frith, R. R. Garcia, A. Gettelman, M. A. Giorgetta, D. E. Kinnison, F. Li, E. Mancini,

## Bibliography

---

- C. McLandress, S. Pawson, G. Pitari, D. A. Plummer, E. Rozanov, F. Sassi, J. F. Scinocca, K. Shibata, B. Steil, and W. Tian (2010), Chemistry-climate model simulations of twenty-first century stratospheric climate and circulation changes, *J. Climate*, *23*, 5349–5374.
- Carlsaw, K. S., T. Peter, J. T. Bacmeister, and S. D. Eckermann (1999), Widespread solid particle formation by mountain waves in the arctic stratosphere, *J. Geophys. Res.*, *104*(D1), 1827–1836.
- Charron, M., and E. Manzini (2002), Gravity waves from fronts: Parameterization and middle atmosphere response in a general circulation model, *J. Atmos. Sci.*, *59*, 923–941.
- Charron, M., E. Manzini, and C. D. Warner (2002), Intercomparison of gravity wave parameterizations: Hines doppler-spread and warner and mcintyre ultra-simple schemes, *J. Met. Soc. Japan*, *80*, 335–345.
- Chimonas, G., and H. M. Hauser (1997), The transfer of angular momentum from vortices to gravity swirl waves, *J. Atmos. Sci.*, *54*, 1701–1711.
- Choi, H. J., H. Y. Chun, and I. S. Song (2009), Gravity wave temperature variance calculated using the ray-based spectral parameterization of convective gravity waves and its comparison with microwave limb sounder observations, *J. Geophys. Res.*, doi: 10.1029/2008JD011330.

- Choi, H.-J., H.-Y. Chun, J. Gong, and D. L. Wu (2012), Comparison of gravity wave temperature variances from ray-based spectral parameterization of convective gravity wave drag with AIRS observations, *J. Geophys. Res.*, *117*, doi:{10.1029/2011JD016900}.
- Chun, H. Y., and J. J. Baik (1998), momentum flux by thermally induced internal gravity waves and its approximation for large-scale models, *J. Atmos. Sci.*, *55*, 3299–3310.
- Chun, H.-Y., M.-D. Song, J.-W. Kim, and J.-J. Baik (2001), Effects of gravity wave drag induced by cumulus convection on the atmospheric general circulation., *Journal of the Atmospheric Sciences*, *58*(3), 302.
- Chun, H. Y., I. S. Song, J. J. Baik, and Y. J. Kim (2004), Impact of a convectively forced gravity wave drag parameterization in NCAR CCM3, *J. Climate*, *17*, 3530–3547.
- Chun, H.-Y., Y.-H. Kim, H.-J. Choi, and J.-Y. Kim (2011), Influence of gravity waves in the tropical upwelling: WACCM simulations., *Journal of the Atmospheric Sciences*, *68*(11).
- Collins, M., S. R. Lewis, and P. L. Read (1997), Gravity wave drag in a global circulation model of the martian atmosphere, *Adv. Space Res.*, *19*, 1245–1254.
- Dewan, E. M., R. H. Picard, R. R. O’Neil, H. A. Gardiner, J. Gibson, J. D. Mill, E. Richards, M. Kendra, and W. O. Gallery (1998), MSX satellite observations of thunderstorm-generated

## Bibliography

---

- gravity waves in mid-wave infrared images of the upper stratosphere, *Geophys. Res. Lett.*, *25*, 939–942.
- Dunkerton, T. J. (1984), Inertia gravity waves in the stratosphere, *J. Atmos. Sci.*, *41*, 3396–3404.
- Dunkerton, T. J. (1997), The role of gravity waves in the quasi-biennial oscillation, *J. Geophys. Res.*, *102*, 26,053–26,076.
- Eckermann, S. D. (2000), Long-term global morphology of gravity wave activity using UARS data, *NASA technical report*, NRA-97-MTPE-04.
- Eckermann, S. D., P. Preusse, B. Schaeler, J. Oberheide, D. Offermann, J. T. Bacmeister, and D. Broutman (2001), Global gravity wave "weather" in the middle atmosphere: preliminary insights from the crista-spas missions, *Proceedings of the Solar Terrestrial and Space Physics Community, 13th. National Congress of the Australian Institute of Physics*, *146*, 11–24.
- Eckermann, S. D., K. W. Hoppel, and L. Coy (2009), High-altitude data assimilation system experiments for the northern summer mesosphere season of 2007, *Journal of Atmospheric and Solar-Terrestrial Physics*, *71*, 531–551.
- Egger, J. (2000), On the energy source for atmospherically induced angular momentum changes of the earth, *Meteorol. Zeit.*, *9*, 377–379.

- Ern, M., and P. Preusse (2012), Gravity wave momentum flux spectra observed from satellite in the summertime subtropics: Implications for global modeling, *Geophysical Research Letters*, *39*(15), n/a–n/a, doi:10.1029/2012GL052659.
- Ern, M., P. Preusse, M. J. Alexander, and C. D. Warner (2004), Absolute values of gravity wave momentum flux derived from satellite data, *J. Geophys. Res.*, *109*(D20103), doi:10.1029/2004JD004752.
- Ern, M., P. Preusse, and C. D. Warner (2006), Some experimental constraints for spectral parameters used in the Warner and McIntyre gravity wave parameterization scheme, *Atmos. Chem. Phys.*, *6*, 4361–4381.
- Ern, M., P. Preusse, J. C. Gille, C. L. Hepplewhite, M. G. Mlynczak, J. M. Russell III, and M. Riese (2011), Implications for atmospheric dynamics derived from global observations of gravity wave momentum flux in strato- and mesosphere, *J. Geophys. Res.*, *116*(D19107), doi:doi:10.1029/2011JD015821.
- Ern, M., P. Preusse, S. Kalisch, M. Kaufmann, and M. Riese (2013), Role of gravity waves in the forcing of quasi two-day waves in the mesosphere: An observational study, *J. Geophys. Res.*, *118*(9), 3467–3485, doi:10.1029/2012JD018208.
- Ern, M., F. Ploeger, P. Preusse, J. Gille, L. Gray, S. Kalisch, M. Mlynczak, J. Russell, and M. Riese (2014), Interaction of gravity waves with the QBO: A satellite perspective, *J. Geophys. Res.*, *119*(5), 2329–2355.

## Bibliography

---

- Farman, J. C., B. G. Gardiner, and J. D. Shanklin (1985), Large losses of total ozone in antarctica reveal seasonal ClOx/NOx interaction, *Nature*, *315*, 207–210, doi:10.1038/315207a0.
- Fels, B. S. (1984), The radiative damping of short vertical scale waves in the mesosphere, *J. Atmos. Sci.*, *41*, 1755–1764.
- Fovell, R., D. Durran, and J. R. Holton (1992), Numerical simulations of convectively generated stratospheric gravity waves, *J. Atmos. Sci.*, *49*, 1427–1442.
- Friedl-Vallon, F., T. Gulde, F. Hase, A. Kleinert, T. Kulesa, G. Maucher, T. Neubert, F. Olschewski, C. Piesch, P. Preusse, H. Rongen, C. Sartorius, H. Schneider, A. Schönfeld, V. Tan, N. Bayer, J. Blank, R. Dapp, A. Ebersoldt, H. Fischer, F. Graf, T. Guggenmoser, M. Höpfner, M. Kaufmann, E. Kretschmer, T. Latzko, H. Nordmeyer, H. Oelhaf, J. Orphal, M. Riese, G. Schardt, J. Schillings, M. K. Sha, O. Suminska-Ebersoldt, and J. Ungermann (2014), Instrument concept of the imaging Fourier transform spectrometer GLORIA, *Atmospheric Measurement Techniques Discussions*, *7*(3), 2301–2337, doi:10.5194/amtd-7-2301-2014.
- Fritts, D. C., and M. J. Alexander (2003), Gravity wave dynamics and effects in the middle atmosphere, *Rev. Geophys.*, *41*(1), doi:10.1029/2001RG000106.
- Fritts, D. C., and P. K. Rastogi (1985), Convective and dynamical

- instabilities due to gravity wave motions in the lower and middle atmosphere: theory and observations, *Radio Sci.*, *20*, 1247–1277.
- Geller, M. A., M. ALEXANDER, P. T. Love, J. Bacmeister, M. Ern, A. Hertzog, E. Manzini, P. Preusse, K. Sato, A. A. Scaife, et al. (2013), A comparison between gravity wave momentum fluxes in observations and climate models., *Journal of Climate*, *26*(17).
- Giorgetta, M. A., E. Manzini, E. Roeckner, M. Esch, and L. Bengtsson (2006), Climatology and forcing of the quasi-biennial oscillation in the MAECHAM5 model, *J. Clim.*, *19*, 3863–3881.
- Goldstein, S. (1931), On the stability of superposed streams of fluids of different densities, *Proceedings of the Royal Society of London. Series A, Containing Papers of a Mathematical and Physical Character*, pp. 524–548.
- Hasha, A., O. Bühler, and J. Scinocca (2008), Gravity wave refraction by three-dimensionally varying winds and the global transport of angular momentum, *J. Atmos. Sci.*, *65*, 2892–2906.
- Hines, C. O. (1997), Doppler-spread parameterization of gravity-wave momentum deposition in the middle atmosphere. Part 1: Basic formulation, *J. Atmos. Solar-Terr. Phys.*, *59*, 371–386.
- Holton, J. R. (1982), The role of gravity wave induced drag and diffusion on the momentum budget of the mesosphere, *J. Atmos. Sci.*, *39*(4), 791–799.

## Bibliography

---

- Holton, J. R., and M. J. Alexander (1999), Gravity waves in the mesosphere generated by tropospheric convection, *Tellus*, *51*, 45–58.
- Holton, J. R., P. H. Haynes, M. E. McIntyre, A. R. Douglass, R. B. Rood, and L. Pfister (1995), Stratosphere-troposphere exchange, *Rev. Geophys.*, *33*, 403–439.
- Huygens, C. (1678), *Traité de la lumière*.
- Jewtoukoff, V., R. Plougonven, and A. Hertzog (2013), Gravity waves generated by deep tropical convection: Estimates from balloon observations and mesoscale simulations, *Journal of Geophysical Research: Atmospheres*, *118*(17), 9690–9707, doi:10.1002/jgrd.50781.
- Jiang, J. H., B. Wang, K. Goya, K. Hocke, S. D. Eckermann, J. Ma, D. L. Wu, and W. J. Read (2004), Geographical distribution and interseasonal variability of tropical deep convection: Uars mls observations and analyses, *J. Geophys. Res.*, *109*(D03111), doi:10.1029/2003JD003756.
- Joshi, M., R. Haberle, J. Hollingsworth, and D. Hinson (2000), A comparison of mgs phase 1 aerobraking radio occultation data and the nasa ames mars gcm, *J. Geophys. Res.*, *105*, 17,601–17,615.
- Kalisch, S., P. Preusse, M. Ern, S. D. Eckermann, and M. Riese (2014), Differences in gravity wave drag between realistic oblique and assumed vertical propagation, *J. Geophys. Res.*, submitted.

- Kim, Y.-H., A. Bushell, D. Jackson, and H.-Y. Chun (2013), Impacts of introducing a convective gravity-wave parameterization upon the QBO in the Met Office Unified Model, *Geophysical Research Letters*, *40*(9), 1873–1877.
- Kim, Y. J., S. D. Eckermann, and H. Y. Chun (2003), An overview of the past, present and future of gravity-wave drag parameterization for numerical climate and weather prediction models - survey article, *Atmosphere-Ocean*, *41*, 65–98.
- Lamb (1910), On the theory of waves propagated vertically in the atmosphere, *Proc. Lond. Math. Soc.*, *7*, 122–141.
- Lehmann, C., Y.-H. Kim, P. Preusse, H.-Y. Chun, M. Ern, and S.-Y. Kim (2012), Consistency between fourier transform and small-volume few-wave decomposition for spectral and spatial variability of gravity waves above a typhoon, *Atmos. Meas. Tech. Discuss.*, *5*, 1763–1793, doi:10.5194/amtd-5-1763-2012, [www.atmos-meas-tech-discuss.net/5/1763/2012/](http://www.atmos-meas-tech-discuss.net/5/1763/2012/).
- Lighthill, M. J. (1967), Waves in fluids, *Communications on Pure and Applied Mathematics*, *20*(2), 267–293.
- Lindzen, R. (1973), Wave-mean flow interactions in the upper atmosphere, *Boundary Layer Meteor.*, *4*, 327–343.
- Lindzen, R. S. (1981), Turbulence and stress due to gravity wave and tidal breakdown, *J. Geophys. Res.*, *86*, 9707–9714.

## Bibliography

---

- Lindzen, R. S., and J. R. Holton (1968), A theory of the Quasi-Biennial Oscillation, *J. Atmos. Sci.*, *25*, 1095–1107.
- Lott, F., and M. J. Miller (1997), A new subgrid scale orographic drag parameterization: Its formulation and testing, *Quart. J. Roy. Meteor. Soc.*, *123*, 101–127.
- Manzini, E., and N. A. McFarlane (1998), The effect of varying the source spectrum of a gravity wave parameterization in a middle atmosphere general circulation model, *J. Geophys. Res.*, *103*, 31,523–31,539.
- Manzini, E., M. A. Giorgetta, M. Esch, L. Kornblueh, and E. Roeckner (2006), The influence of sea surface temperatures on the northern winter stratosphere: Ensemble simulations with the MAECHAM5 model, *J. Climate*, *19*, 3863–3881.
- Marks, C. J., and S. D. Eckermann (1995), A three-dimensional nonhydrostatic ray-tracing model for gravity waves: Formulation and preliminary results for the middle atmosphere, *J. Atmos. Sci.*, *52*, 1959–1984.
- McDonald, A. J., S. E. George, and R. M. Woollands (2009), Can gravity waves significantly impact PSC occurrence in the Antarctic?, *Atmos. Chem. Phys.*, *9*, 8825–8840.
- McIntyre, M. E. (1998), Breaking waves and global scale chemical transport in the Earth’s atmosphere, with spinoffs for the Sun’s interior, *Prog. of Theor. Phys.*, *130*, 137–166.

- McIntyre, M. E. (1999), Breaking waves and global-scale chemical transport in the Earth's atmosphere, with spinoffs for the Sun's interior Errata, *Prog. of Theor. Phys.*, *130*, 137–166.
- McLandress, C. (1998), On the importance of gravity waves in the middle atmosphere and their parameterization in general circulation models, *J. Atmos. Terr. Phys.*, *60*, 1357–1383.
- McLandress, C., and J. F. Scinocca (2005), The GCM response to current parameterizations of nonorographic gravity wave drag, *J. Atmos. Sci.*, *62*, 2394–2413.
- McLandress, C., and T. G. Shepherd (2009), Simulated anthropogenic changes in the brewer-dobson circulation, including its extension to high latitudes, *J. Clim.*, *22*, 1516–1540, doi:10.1175/2008JCLI2679.1.
- Medvedev, A. S., and G. P. Klaassen (2000), Parameterization of gravity wave momentum deposition based on nonlinear wave interactions: basic formulation and sensitivity tests, *J. Atm. Sol.-Terr. Phys.*, *62*, 1015–1033.
- Medvedev, A. S., and G. P. Klaassen (2001), Realistic semiannual oscillation simulated in a middle atmosphere general circulation model, *Geophys. Res. Lett.*, *28*, 733–736.
- Mlynczak, M. G. (1997), Energetics of the mesosphere and lower thermosphere and the saber experiment, *Adv. Space Res.*, *20*, 1177–1183.

## Bibliography

---

- Molina, M. J., and F. S. Rowland (1974), Stratospheric sink for chlorofluoromethanes: chlorine atom-catalyzed destruction of ozone, *Nature*, *249*, 810–812.
- Newton, I. (1687), *Philosophiae naturalis principia mathematica*, *Journal of the Royal Society*.
- Offermann, D., K.-U. Grossmann, P. Barthol, P. Knieling, M. Riese, and R. Trant (1999), Cryogenic Infrared Spectrometers and Telescopes for the Atmosphere (CRISTA) experiment and middle atmosphere variability, *J. Geophys. Res.*, *104*, 16,311–16,325.
- Orr, A., P. Bechtold, J. Scinocca, M. Ern, and M. Janiskova (2010), Improved middle atmosphere climate and forecasts in the ECMWF model through a nonorographic gravity wave drag parameterization, *J. Climate*, *23*, 5905–5926.
- Pfister, L., S. Scott, M. Loewenstein, S. Brown, and M. Legg (1993), Mesoscale disturbances in the tropical stratosphere excited by convection: Observations and effects on the stratospheric momentum budget., *J. Atmos. Sci.*, *50*, 1058–1075.
- Pitteway, M. L. V., and C. O. Hines (1963), The viscous damping of atmospheric gravity waves, *Canadian Journal of Physics*, *41*, 1935–1948, doi:10.1139/p63-194.
- Plumb, R. A., and A. D. McEwan (1978), The instability of a forced standing wave in a viscous stratified fluid: A laboratory analogue of the Quasi-Biennial Oscillation, *J. Atmos. Sci.*, *35*, 1827–1839.

- Preusse, P. (2001), Satellitenmessungen von Schwerewellen in der mittleren Atmosphäre mit CRISTA, *Wuppertal University*, 9, PhD thesis.
- Preusse, P., G. Eidmann, S. D. Eckermann, B. Schaeler, R. Spang, and D. Offermann (2001), Indications of convectively generated gravity waves in CRISTA temperatures, *Adv. Space Res.*, 27, 1653–1658.
- Preusse, P., A. Dörnbrack, S. D. Eckermann, M. Riese, B. Schaeler, J. T. Bacmeister, D. Broutman, and K. U. Grossmann (2002), Space-based measurements of stratospheric mountain waves by CRISTA, 1. sensitivity, analysis method, and a case study, *J. Geophys. Res.*, 107, doi:10.1029/2001JD000699.
- Preusse, P., M. Ern, M. J. Alexander, and M. Bartelt (2003), Estimates of the horizontal wavelenghts of gravity waves and the implications for the tropical maximum observed in satellite climatologies, *J. Geophys. Res.*, submitted.
- Preusse, P., M. Ern, S. D. Eckermann, C. D. Warner, R. H. Picard, P. Knieling, M. Krebsbach, J. M. R. III, M. G. Mlynczak, C. J. Mertens, and M. Riese (2006), Tropopause to mesopause gravity waves in August: measurement and modeling, *J. Atmos. Solar-Terr. Phys.*, 68, 1730–1751.
- Preusse, P., S. D. Eckermann, and M. Ern (2008), Transparency of the atmosphere to short horizontal wavelength gravity waves, *J. Geophys. Res.*, 113(D24), doi:10.1029/2007JD009682.

## Bibliography

---

- Preusse, P., S. D. Eckermann, M. Ern, J. Oberheide, R. H. Picard, R. G. Roble, M. Riese, J. M. Russell III, and M. G. Mlynczak (2009), Global ray tracing simulations of the saber gravity wave climatology, *J. Geophys. Res.*, *114*(D08126), doi:10.1029/2008JD011214.
- Pulido, M., and J. Thuburn (2008), The seasonal cycle of gravity wave drag in the middle atmosphere, *Journal of Climate*, *21*(18), 4664–4679, doi:{10.1175/2008JCLI2006.1}.
- Queney, P. (1948), The problem of airflow over mountains: A summary of theoretical studies, *Bull. Am. Meteor. Soc.*, *29*, 16–27.
- Reed, R. J., W. J. Campbell, L. A. Rasmussen, and D. G. Rodgers (1961), Evidence of downward-propagating annual wind reversal in the equatorial stratosphere, *J. Geophys. Res.*, *66*, 813–818.
- Remsberg, E. E., B. T. Marshall, M. garcia-Comas garcia-Comas garcia Comas, D. Krueger, G. S. Lingenfelter, J. Martin-Torres, M. G. Mlynczak, J. M. R. III, A. K. Smith, Y. Zhao, C. Brown, L. L. Gordley, M. J. Lopez-Gonzalez, M. Lopez-Puertas, C. Y. She, M. J. Taylor, and R. E. Thompson (2008), Assessment of the quality of the version 1.07 temperature-versus-pressure profiles of the middle atmosphere from timed/saber, *J. Geophys. Res.*, *113*(D17101), doi:10.1029/2008JD010013.
- Richter, J. H., Fabricio Sassi, and R. R. Garcia (2010), Toward a physically based gravity wave source parameterization in a general circulation model, *J. Atmos. Sci.*, *67*, 136–156.

- Rienecker, M. M., M. J. Suarez, R. Gelaro, R. Todling, J. Bacmeister, E. Liu, M. G. Bosilovich, S. D. Schubert, L. Takacs, G.-K. Kim, S. Bloom, J. Chen, D. Collins, A. Conaty, A. da Silva, W. Gu, J. Joiner, R. D. Koster, R. Lucchesi, and A. Molod (2011), Merra: Nasa's modern-era retrospective analysis for research and applications., *Journal of Climate*, *24*(14), 3624 – 3648.
- Riese, M. (1994), Das CRISTA-Meßsystem: Struktur und Anwendungen, Dissertation, Universität Wuppertal.
- Riese, M., P. Preusse, R. Spang, M. Ern, M. Jarisch, K.-U. Grossmann, and D. Offermann (1997), Measurements of trace gases by the Cryogenic Infrared Spectrometers and Telescopes for the Atmosphere (CRISTA) experiment, *Adv. Space Res.*, *19*, 563–566.
- Riese, M., R. Spang, P. Preusse, M. Ern, M. Jarisch, D. Offermann, and K. U. Grossmann (1999), Cryogenic Infrared Spectrometers and Telescopes for the Atmosphere (CRISTA) data processing and atmospheric temperature and trace gas retrieval, *J. Geophys. Res.*, *104*, 16,349–16,367.
- Riese, M., H. Oelhaf, P. Preusse, J. Blank, M. Ern, F. Friedl-Vallon, H. Fischer, T. Guggenmoser, M. Höpfner, P. Hoor, M. Kaufmann, J. Orphal, F. Plöger, R. Spang, O. Suminska-Ebersoldt, J. Ungermann, B. Vogel, and W. Woiwode (2014), Gimballed limb observer for radiance imaging of the atmosphere (GLORIA) scientific objectives, *Atmospheric Measurement Techniques Discussions*, *7*(2), 1535–1572, doi:10.5194/amtd-7-1535-2014.

## Bibliography

---

- Roble, R. G., and E. C. Ridley (1994), A thermosphere-ionosphere-mesosphere-electrodynamics general circulation model (TIME-GCM): Equinox solar cycle minimum simulations (30-500 km), *Geophys. Res. Lett.*, *21*, 417–420.
- Roeckner, E., G. Bauml, L. Bonaventura, R. Brokopf, M. Esch, M. Giorgetta, S. Hagemann, I. Kirchner, L. Kornblueh, E. Manzini, et al. (2003), The atmospheric general circulation model ECHAM5. part i: model description, *Scientific Report of the Max Planck Society - Report No. 349*.
- Russell, J. M., M. G. Mlynczak, L. L. Gordley, J. Tansock, and R. Esplin (1999), An overview of the saber experiment and preliminary calibration results, *Proceeding SPIE*, (3756), 277–288.
- Sato, K., M. Yamamori, S. Y. Ogino, N. Takahashi, Y. Tomikawa, and T. Yamanouchi (2003), A meridional scan of the stratospheric gravity wave field over the ocean in 2001 (mess02001), *J. Geophys. Res.*, *108*(4491), doi:10.1029/2002JD003219.
- Schmidt, T., G. Beyerle, S. Heise, J. Wickert, and M. Rothacher (2008), A climatology of multiple tropopauses derived from GPS radio occultations with CHAMP and SAC-C, *Geophys. Res. Lett.*, *33*(L11806), doi:10.1029/2005GL024600.
- Schwartz, M. J. (2008), Validation of the Aura Microwave Limb Sounder temperature and geopotential height measurements, *J. Geophys. Res.*, *113*(D15S11), doi:10.1029/2007JD008783.

- Sigmond, M., and J. F. Scinocca (2010), The Influence of the Basic State on the Northern Hemisphere Circulation Response to Climate Change, *J. Clim.*, *23*(6), 1434–1446, doi:{10.1175/2009JCLI3167.1}.
- Song, I. S., and H. Y. Chun (2005), Momentum flux spectrum of convectively forced internal gravity waves and its application to gravity wave drag parameterization. Part I: theory, *J. Atmos. Sci.*, *62*, 107–124.
- Song, I. S., and H. Y. Chun (2008), A lagrangian spectral parameterization of gravity wave drag induced by cumulus convection, *J. Atmos. Sci.*, *65*, 1204–1224.
- Song, I. S., H. Y. Chun, R. R. Garcia, and B. A. Boville (2007), Momentum flux spectrum of convectively forced internal gravity waves and its application to gravity wave drag parameterization. Part II: Impacts in a gcm (WACCM), *J. Atmos. Sci.*, *64*, 2286–2308.
- Suarez, M. J., M. M. Rienecker, R. Todling, J. Bacmeister, L. Takacs, H. C. Liu, W. Gu, M. Sienkiewicz, R. D. Koster, R. Gelaro, I. Stajner, and J. E. Nielsen (2008), The GEOS-5 data assimilation system, *NASA technical reports*.
- Taylor, M. J., and M. A. Hapgood (1988), Identification of a thunderstorm as a source of short period gravity waves in the upper atmospheric nightglow emissions, *Planet. Space Sci.*, *36*(10), 975–985.

## Bibliography

---

- Trey, F. (1919), Ein Beitrag zum Studium der Luftwogen, *Meteorol. Z.*, 36, 25–28.
- Trinh, Q. T., S. Kalisch, P. Preusse, H.-Y. Chun, S. D. Eckermann, and M. Riese (2014), Observational filter for limb sounders applied to convective gravity waves, *Atmospheric Measurement Techniques (AMT)*, to be submitted.
- Tsuda, T., M. Nishida, C. Rocken, and R. H. Ware (2000), A global morphology of gravity wave activity in the stratosphere revealed by the GPS occultation data (GPS/MET), *J. Geophys. Res.*, 105(D6), 7257–7274.
- Ungermann, J., L. Hoffmann, P. Preusse, M. Kaufmann, and M. Riese (2010), Tomographic retrieval approach for mesoscale gravity wave observations by the PREMIER Infrared Limb-Sounder, *Atmos. Meas. Tech.*, 3, 339–354.
- Warner, C. D., and M. E. McIntyre (1999), Toward an ultra-simple spectral gravity wave parameterization for general circulation models, *Earth Planets Space*, 51, 475–484.
- Watanabe, S. (2008), Constraints on a non-orographic gravity wave drag parameterization using a gravity wave resolving general circulation model, *Sci. Online Lett. Atmos.*, 4, 61–64.
- Wegener, A. (1906), Studien über Luftwogen, *Beitr. Physik Freien Atmos.*, 4, 23–25.

- Wentzel, G. (1926), Eine Verallgemeinerung der Quantenbedingungen für die Zwecke der Wellenmechanik, *Zeitschrift für Physik*, *38*, 518–529, doi:10.1007/BF01397171.
- Wu, D. L., and S. D. Eckermann (2008), Global gravity variances from aura mls: characteristics and interpretation, *J. Atmos. Sci.*, *65*, 3695–3718.
- Yee, J. H., E. R. Talaat, A. B. Christensen, T. L. Killeen, J. M. Russell, and T. N. Woods (2003), Timed instruments, *Johns Hopkins APL Technical Digest*, *24*, 156–164.
- Zhu, X. (1994), A new theory of the saturated gravity wave spectrum for the middle atmosphere, *J. Atmos. Sci.*, *51*, 3615–3626.